Hydrous fluids in the mantle

Dissertation

Zur Erlangung der Würde eines
Doktors der Naturwissenschaften
- Dr. rer. nat. -

der Bayreuther Graduiertenschule für Mathematik und Naturwissenschaften

vorgelegt von

Kirill Vlasov

aus Moskau

Bayreuth 2022

Die vorliegende Arbeit wurde in der Zeit von Juli 2018 bis Mai 2022 in Bayreuth am Bayerischen Geoinstitut unter Betreuung von Herrn Professor Dr. Hans Keppler angefertigt.

Vollständiger Abdruck der von der Bayreuther Graduiertenschule für Mathematik und Naturwissenschaften (BayNAT) der Universität Bayreuth genehmigten Dissertation zur Erlangung des akademischen Grades eines Doktors der Naturwissenschaften (Dr. rer. nat.).

Dissertation eingereicht am: 16.05.2022

Zulassung durch das Leitungsgremium: 18.05.2022

Wissenschaftliches Kolloquium: 26.01.2023

Amtierender Direktor: Prof. Dr. Hans Keppler

Prüfungsausschuss:

Prof. Dr. Hans Keppler	(Gutachter)
PD. Dr. Catherine McCammon	(Gutachterin)
Prof. Dr. Daniel Frost	(Vorsitz)
Prof. Dr. Leonid Dubrovinsky	

Table of contents

Summary

Aqueous fluids affect mass transfer as well as the formation of melts and mineral phases in the upper mantle. In present thesis, I investigated three particular aspects of the geochemistry of mantle fluids – the electrical conductivity of KCl-bearing aqueous fluids, the critical curve in the H_2-H_2O system, and the stability of the acetate in the subduction zones. All three topics address fundamental properties of H_2O in the uppermost 200 km of the Earth, being directly interconnected as many of described effects may occur in similar geological settings.

Evidence from diamond inclusions suggests that KCl-bearing fluids may be abundant in the subcratonic mantle and these fluids may also cause local anomalies of high electrical conductivity. I therefore measured the electrical conductivity of aqueous fluids containing 6.96, 0.74 and 0.075 wt% KCl using a hydrothermal diamond anvil cell to 2.5 GPa and 675 °C, and with a piston-cylinder apparatus to 5 GPa and 900 °C. I found that below 550 °C, increasing pressure generally decreases solution conductivity, while at higher temperatures the effect is opposite. However, at high pressures, the conductivity of KCl in H_2O is smaller than for NaCl, possibly due to a hydration shell collapse. The experimental data are described by two numerical models. The first model (R^2 = 0.999), is preferable for crustal conditions: $\log \sigma = -2.03 + 25.0*T^{-1} + 0.923*\log c + 0.990*\log \rho + \log \Lambda_0$, where σ is the conductivity in S/m, T is temperature in K, c is KCl concentration in wt%, ρ is the density of pure water (in g/cm^3) at given pressure and temperature. Λ_0 is the limiting molar conductivity of KCl (in S·cm^2·mol^{-1}): $\Lambda_0 = 1377 - 1082*\rho + 6883*10^2*T^{-1} - 2471*10^5*T^{-2}$. The second model ($R^2$ = 0.986), is applicable to the lithospheric mantle: $\log \sigma = -1.52 - 357*T^{-1} + 0.865*\log c + 1.72 * \log \rho + \log \Lambda_0$, with the same equation for Λ_0. The latter model shows that already traces of KCl-bearing aqueous fluid may account for high conductivity anomalies in the subcratonic mantle.

Immiscibility between water and hydrogen in planetary interiors may have multiple implications for current and past geological processes, such as early mantle oxidation and the formation of shallow super-reduced domains. The critical curve in the H_2-H_2O system was previously established for pressures of 1.75 – 2.7 GPa. In this thesis, I describe piston-cylinder experiments that triple this range, providing data for 1-4 GPa. The experiments were caried out with an external Fe-FeO buffer and fluid miscibility was determined by trapping fluid inclusions in single crystals

of quartz or olivine. The inclusions were then studied by Raman spectroscopy. From 1 to 3.5 GPa, the slope of the critical curve gradually increases, and ultimately exceeds the temperatures defined by Archean and present geotherms. This suggests that at depths exceeding 100 km, water and hydrogen were immiscible through most of Earth's geologic history. This fact has significant implications for the young Earth's outgassing and for the formation of the first reducing atmosphere. Moreover, the rapid oxidation of the upper mantle may have been caused by the emergence of H_2-H_2O immiscibility and rapid H_2 escape. To better understand the geochemical consequences of this process, I also studied element partitioning between the coexisting H_2 and H_2O phases by laser ablation ICP-MS analyses of fluid inclusions from runs doped with a suite of trace elements. Most trace elements prefer the aqueous fluid phase, but both xenon and CH_4 partition preferentially into the H_2-rich phase. The rapid loss of radiogenic ^{129}Xe and of xenon isotopes produced by fission of plutonium in the first ~100 Myr after Earth´s formation may therefore be related to H_2-H_2O immiscibility and rapid loss of the H_2-rich phase from the mantle.
Recent theoretical studies have suggested that under certain intermediate redox conditions, organic anions, in particular carboxylic acids anions like acetate, may be the dominant carbon species in deep subduction zone fluids. This could have major consequences for the properties of these fluids, for the formation of diamonds, and for the deep carbon cycle in general. In a project carried out together with master student Victoria Szlachta we have tested these predictions by carrying out both ex-situ piston cylinder experiments and in-situ Raman spectroscopic experiments in the externally-heated diamond cell to 600 ˚C and 5 GPa, the predicted stability field of acetate. We observed that upon heating and pressurization to these conditions, an aqueous solution of sodium acetate undergoes several interesting reactions, including the formation of carbonate and higher hydrocarbons. However, at 5 GPa and 600 ˚C, almost all organic species appear to have decomposed to some graphite or amorphous carbon-like material. Our experiments therefore do not support the stability of acetate and other organics as main carbon species in deep subduction fluids. However, the stability of minor concentrations of such species is still possible and requires further study. During deep subduction, most of the reduced carbon in sediments may be retained and recycled into the mantle to great depth.

Zusammenfassung

Wasserhaltige Fluide beeinflussen den Stofftransport im Mantel, die Bildung von Schmelzen und die Stabilität von Mineralen. In der vorliegenden Dissertation habe ich drei verschiedene Aspekte der Geochemie von Mantel-Fluiden untersucht: Die elektrische Leitfähigkeit von KCl-haltigen wässrigen Fluiden, die kritische Kurve im H_2-H_2O-System, sowie die Stabilität von Azetat in Subduktionszonen. Alle drei Themen beschäftigen sich mit den fundamentalen Eigenschaften von Wasser in den oberen 200 km der Erde. Sie stehen in engem Zusammenhang zueinander, weil sie Effekte beschreiben, die in ähnlichen geologischen Systemen auftreten können.

Untersuchungen von Einschlüssen in Diamanten lassen vermuten, dass KCl-reiche Fluide im subkratonischen Mantel recht verbreitet sind und möglicherweise lokale Anomalien mit hoher elektrischer Leitfähigkeit verursachen. Ich habe daher die elektrische Leitfähigkeit von Fluiden mit 6,96, 0,74 und 0,075 Gew. % KCl gemessen, in einer hydrothermalen Diamantstempel-Zelle bis 2,5 GPa und 675 ˚C und in einer Piston-Cylinder-Apparatur bis 5 GPa und 900 ˚C. Unterhalb 550 ˚C erhöht sich die Leitfähigkeit mit dem Druck, während bei höherer Temperatur der gegenteilige Effekt auftritt. Bei hohem Druck ist die Leitfähigkeit von KCl in Wasser kleiner als für NaCl, möglicherweise wegen einem Zusammenbruch der Hydrat-Hülle um das Ion. Die experimentellen Daten wurden durch zwei numerische Modelle beschrieben. Das erste Modell (R^2 = 0.999), ist besonders geeignet für Bedingungen in der Erdkruste: $\log \sigma = -2{,}03 + 25{,}0*T^{-1} + 0{,}923*\log c + 0{,}990*\log \rho + \log \Lambda_0$, wobei σ die Leitfähigkeit in S/m ist, T die Temperatur in K, c die KCl Konzentration in Gew. % und ρ die Dichte von reinem Wasser (in g/cm^3) beim jeweiligem Druck und der jeweiligen Temperatur. Λ_0 ist die molare Leitfähigkeit von KCl bei unendlicher Verdünnung (in $S \cdot cm^2 \cdot mol^{-1}$): $\Lambda_0 = 1377 - 1082*\rho + 6883*10^2*T^{-1} - 2471*10^5*T^{-2}$. Das zweite Modell ($R^2$ = 0.986), ist geeignet für den lithosphärischen Mantel: $\log \sigma = -1.52 - 357*T^{-1} + 0{,}865*\log c + 1{,}72 * \log \rho + \log \Lambda_0$, mit der gleichen Formel für Λ_0. Das zweite Modell zeigt, dass bereits Spuren von KCl-haltigen wässrigen Fluiden die Anomalien hoher Leitfähigkeit im Mantel unterhalb von Kratonen erklären können.

Die Entmischung zwischen Wasser und Wasserstoff im Innern von Planeten kann unterschiedliche Effekte verursachen, wie etwa die frühe Oxidation des Erdmantels oder die Bildung extrem reduzierter Domänen im Mantel. Die kritische Kurve im H_2-H_2O-System war bisher bekannt für

den Druckbereich von 1,75 bis 2,7 GPa. In der vorliegenden Dissertation beschreibe ich Piston-Cylinder-Experimente, die diesen Druckbereich etwa verdreifachen, mit Daten für 1 bis 4 GPa. Die Experimente wurden mit einem Fe-FeO-Puffer ausgeführt. Die Mischbarkeit von Fluiden wurde untersucht, indem synthetischen Fluideinschlüssen in Quarz oder Olivin erzeugt und dann mit Raman-Spektroskopie untersucht wurden. Von 1 bis 3,5 GPa wird die Steigung der kritischen Kurve zunehmend steiler, bis sie oberhalb der Temperaturprofile sowohl des modernen als auch des archaischen Erdmantels liegt. Bei Tiefen jenseits von 100 km lagen daher Wasser und Wasserstoff während des größten Teils der Erdgeschichte als entmischte Phasen vor. Dies hat wichtige Konsequenzen für die Entgasung der jungen Erde und für die Bildung der ersten reduzierenden Atmosphäre. Die Entmischung und das schnelle Entweichen einer H_2-reichen Fluidphase hat möglicherweise die frühe Oxidation des Erdmantels verursacht. Um die geochemischen Konsequenzen dieses Prozesses besser zu verstehen, habe ich die Verteilung von Spurenelementen zwischen koexistierenden H_2- und H_2O-Phasen mit Hilfe von Laser-Ablations-ICP-MS-Analysen von synthetischen Flüssigkeitseinschlüssen in dotierten Proben untersucht. Die meisten Spurenelemente bevorzugen die wässrige Phase, aber sowohl Xenon als auch Methan reichern sich in der H_2-Phase an. Die schnelle Entgasung von radiogenem ^{129}Xe und von Xenon-Isotopen aus dem radioaktiven Zerfall von Plutonium in den ersten 100 Millionen Jahren nach der Entstehung der Erde könnten daher auf die Entgasung einer H_2-reichen entmischten Fluidphase zurückzuführen sein.

Neuere theoretische Studien haben vorhergesagt, dass unter gewissen intermediären Redox-Bedingungen Anionen organischer Säuren, wie insbesondere Azetat, die wichtigsten Träger von Kohlenstoff in den wässrigen Fluiden tief in Subduktionszonen sind. Dies könnte wichtige Auswirkungen auf die Eigenschaften dieser Fluide, auf die Bildung von Diamanten und für den tiefen Kohlenstoff-Zyklus überhaupt haben. In einem Projekt, das ich zusammen mit der Master-Studentin Victoria Szlachta ausgeführt habe, wurde diese Vorhersage sowohl durch ex-situ Piston-Cylinder-Experimente als auch durch in-situ Messungen in Diamantstempel-Zellen bei bis zu 600 ˚C und 5 GPa getestet. Beim Aufheizen und bei Druckerhöhung zu diesen Bedingungen laufen in einer Azetat-Lösung mehrere interessante Reaktionen ab, die unter anderem zur Bildung von Carbonat und von höheren Alkanen führen. Bei 5 GPa und 600 ˚C, dem vorhergesagten Stabilitätsbereich von Azetat zersetzen sich jedoch praktisch alle organischen Spezies zu einem Graphit-ähnlichen Kohlenstoff-reichen Material. Unsere Experimente bestätigen daher nicht die

Stabilität von Azetat oder anderen organischen Anionen in tiefen Subduktions-Fluiden. Die Stabilität geringer Konzentrationen dieser Spezies bleibt jedoch denkbar und erfordert weitere Untersuchungen. Bei tiefer Subduktion bleibt wahrscheinlich der größte Teil des reduzierten Kohlenstoffs in den Sedimenten erhalten und wird tief in den Mantel zurückgeführt.

1. Introduction

1.1. Water in the Earth's lithosphere and upper mantle

Water is a key component of our planet's interior. The behavior of aqueous fluids in the lithosphere is partially described by existing equations of state for pure H_2O (Pitzer & Sterner, 1994; Wagner & Pruß, 2002), developed from experimental data of the previous century. However, being semi-empirical, those equations do not fully describe all possible properties of water, omitting, for example, such a crucial component of aqueous geochemistry as the dielectric constant of H_2O (Sverjensky, Harrison et al., 2014). Thus, many contemporary research projects do not use experimentally established values for the physical and chemical properties of aqueous solutions, but estimates, obtained from extrapolations and numerical studies.

The presence of fluids in the deep parts of the continental crust has been a matter of active debate since decades (R. B. Frost & Bucher, 1994; Wannamaker, 2000; Yardley & Valley, 1997), driven by the contradictions between petrological and geophysical observations. The former, based on mineral reactions and rock properties, advocated for the case of a dry lower crust, while the latter, supported by the magnetotelluric and seismic data, proposed the presence of a fluid phase. Reality turned out to be somewhere in between these extremes (Yardley, 2009; Yardley & Bodnar, 2014). Fluids definitely are present in fault systems and tectonically active regions (Manning, 2018) as well as during granulite facies metamorphic events (Newton et al., 2014; Touret, 2009; Touret & Huizenga, 2012). When present, such fluids can induce crustal melting (e.g. Weinberg & Hasalová, 2015), which is especially relevant for tectonically active zones. Nevertheless, the general statement by Yardley and Valley (1997) that most of the ambient lower continental crust regions are dry still holds true.

Fluids certainly play a major role in subduction zones. Subduction fluids drive magma generation and metamorphic reactions (Peacock, 1990; Prouteau et al., 1999; Rustioni et al., 2019), trigger earthquakes (Kato et al., 2010; Peacock & Hyndman, 1999) and are the main force behind element transfer in the subduction zones (Keppler, 1996, 2017; Manning, 2004). For subduction fluids, one of the core research questions is how deep the water is transferred by the slabs and where the total dehydration of the slab happens. Experimental studies of hydrogen containing phases (NAM, DHMS) (D. J. Frost, 2006; Ohtani, 2015; Ohtani et al., 2018; Pamato et al., 2015; Smyth, 2018)

and geochemical evidences from deep diamonds (Palot et al., 2016; Smith et al., 2018) suggest that the total dehydration frontier lies somewhere in the lower mantle. Previously, it was assumed, that water cannot exist in mantle because of the low oxygen fugacities prevailing, but this may not be so (D. J. Frost & McCammon, 2008; Tschauner et al., 2018). By now, the idea that aqueous supercritical fluids occur in some regions of the Earth's mantle appears to be accepted by the majority of geologists.

1.2. Physical and chemical properties of water

Understanding aqueous fluid-related processes requires the precise knowledge of the chemical and physical properties of water. For fluids, the pressure and temperature range covered by measurements of physical properties is dramatically smaller than for solid phases, rarely exceeding 5 GPa and 1000°C, with more extreme conditions typically being explored via numerical methods (e.g. Galvez et al., 2016; Hou et al., 2020).

Partially, this is caused by the notorious ability of fluids to escape completely not only from rocks (e.g Bodinier et al. 1990) but even from sealed experimental environments. Thus, accessible experimental techniques are constrained by a number of factors, of which probably the most important one is a need to maintain isochoric conditions at elevated pressures and temperatures. A classic apparatus, perfected for this task is an externally heated cold pressure vessel (Holloway, 1971; Luth & Tuttle, 1963). After minor recent improvements (e.g. Berndt et al. 2002) these devices have reached their technological limit, allowing to investigate aqueous fluids to deep crustal conditions (~1 GPa). Fortunately, the recent development of new techniques for this field of research, in particular hydrothermal diamond anvil cells (e.g. Bassett et al., 1993; J. Li et al., 2016), make it possible to overcome that technological barrier.

In most chemical interactions in Earth's interior, water acts as a solvent, due to its polarity and ability to dissociate. One key solvent property is density, which greatly influences self-dissociation and viscosity. In general, with increasing pressure the density increases, while increasing temperature has the opposite effect (Fig. 1.1). At ambient conditions, water is a liquid with a density of 0.997 g/cm^3, in equilibrium with water vapor with a density of $2 \cdot 10^{-5}$ g/cm^3. On heating, the liquid and the vapor phase boundary will disappear at the critical point (Fig. 1.1, CP), which is defined by three critical parameters: T_c= 647.1 K, P_c= 22.1 MPa, ρ_c= 0.322 g/cm^3 (Weingärtner

& Franck, 2005). Beyond this point, water is a supercritical fluid, which is its most common state in the Earth's interior.

Most measurements of water density were performed below 1 GPa (e.g. Kell et al., 1978), however several studies expanded the range of explored pressures to 5.5 GPa (Abramson & Brown, 2004; Wiryana et al., 1998; Withers et al., 2000). The most recent advancement in water density research at elevated pressures and temperatures was the application of Brillouin spectroscopy, allowing the estimation of ρ to 7 GPa and 400 °C (Sanchez-Valle et al., 2013). The widely accepted equation of state for water "IAPWS-95" (Wagner & Pruß, 2002), correctly describes water properties up to 1273 K and 1 GPa. Unfortunately, this just covers the conditions of lower continental crust. An equation of state derived by Pitzer and Sterner (1994), typically used in the field of geochemistry is only slightly less accurate, but usable up to 2000 K and 10 GPa.

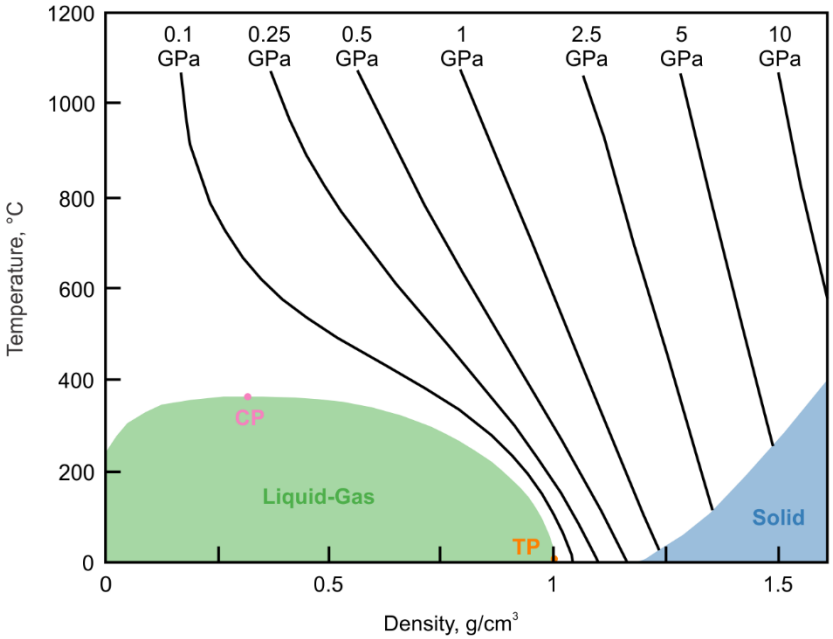

Figure 1.1. *Water phase diagram in ρ-T coordinates with isobars to 10 GPa (CP – critical point, TP – triple point). Modified after (Weingärtner & Franck, 2005).*

The relative dielectric permittivity of water is another parameter that is crucial for understanding deep fluids. Also known as the dielectric constant of water (ε_{H_2O}), this property largely controls dissociation processes and the solubility of various compounds. Furthermore, it is a fundamental component of the Helgeson–Kirkham–Flowers (HKF) equations of state for aqueous species (Helgeson et al., 1981), commonly used in geochemical modelling. Experimentally, ε_{H_2O} at surface

and upper crustal conditions has been measured (e.g. Uematsu and Frank 1980; Fernández et al. 1995), mainly by the means of impedance spectroscopy. However, due to the high complexity of such experiments the value of ε_{H_2O} was experimentally established only up to 0.5 GPa (5 kb) and 550 °C (Heger et al., 1980). Those data were later extrapolated to higher temperatures by Pitzer (1983), based on statistical mechanics considerations. They were incorporated into the thermodynamic software package SUPCRT92 (Johnson et al., 1992) that supports geochemical calculations involving aqueous fluid up to 0.5 GPa and 1000 °C.

A novel semi-theoretical approach to estimate the dielectric constant of H_2O was implemented by Sverjensky, Harrison et al. (2014). They used a combination of statistical mechanics-based equations and mineral solubility data to obtain ε_{H_2O} estimates to 6 GPa and 1200 °C. This achievement allowed them to formulate the Deep Earth Water (DEW) model (F. Huang & Sverjensky, 2019; Sverjensky, 2019; Sverjensky, Harrison et al., 2014). This advanced model replaced SUPCRT92 and allows geochemists to calculate compositions of fluids in the deep parts of subduction zones and in the regions of diamond formation beneath cratons. As of now, the DEW model was successfully applied to quantify, for example, chromium solubility (J. Huang et al., 2019) or carbon speciation in fluids (Stolte et al., 2021; Sverjensky, Stagno et al., 2014). However, those results, being purely theoretical, still require experimental corroboration. Subsequent research on ε_{H_2O} mostly focused on *ab initio* molecular dynamics simulations (e.g. Fowler & Sherman, 2020; Hou et al., 2020; Pan et al., 2013) based primarily on the SPC/E (Berendsen et al., 1987) and TIP4P (Jorgensen et al., 1998) water models.

The value of dielectric constant affects water dissociation. Dissociation of water may be described by the equilibrium

$$H_2O = H^+ + OH^-$$

with the equilibrium constant

$$K = \frac{a(H^+)a(OH^-)}{a(H_2O)}$$

Under conditions where water is only slightly dissociated, this may be approximated by

$$K_w = a(H^+)a(OH^-)$$

The water dissociation constant (K) and ion product (K_w) are defined here as functions of the activities (a) of the corresponding molecular and ionic species. The ion product of water, which is a good representation of an overall water dissociation state, dramatically changes with increasing pressure and temperature, which affects overall fluid pH and an the ability of an aqueous fluid to carry solutes (Weingärtner & Franck, 2005). Up to 1000 °C and 1 GPa K_w was precisely determined by Holzapfel and Franck (1966). Measurements at more extreme conditions proved to be very difficult and no additional experimental data of comparable quality have been reported. Information on the high pressure-high temperature region could in principle be obtained via shockwave experiments, with values reported up to 180 GPa and 10 000 K (Chau et al., 2001). However, the quality of these data is relatively poor due to the large uncertainties in pressure and temperature determination, making them of limited value for geochemical applications.

1.3. Compositions of Earth's upper mantle fluids

Water remains the dominant component of upper mantle fluids to ~250 km depth (~8 GPa, Fig. 1.2). As this fluid normally exists within silicate rocks, silica is an ubiquitous solute. For shallow depths, SiO_2 solubility in H_2O has been explored almost three decades ago (Manning, 1994), with a notable decrease of solubility for increased salinities (Newton & Manning, 2006). For the majority of the upper mantle conditions, H_2O and SiO_2 are fully miscible (Bureau & Keppler, 1999; Shen & Keppler, 1997) and intermediate compositions between pure silicate melt and aqueous fluid may exist.

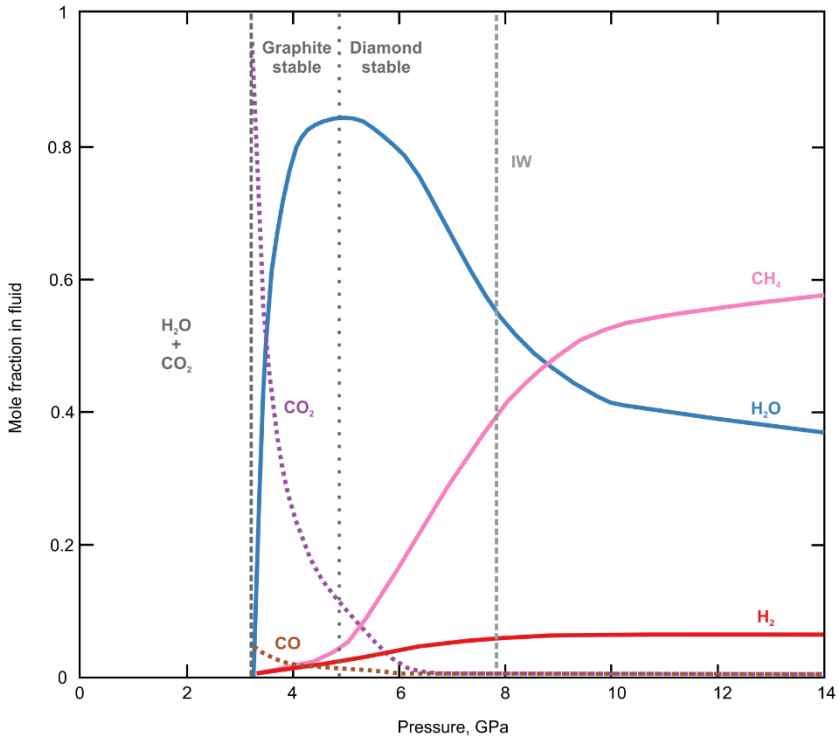

Figure 1.2. *Upper mantle fluid speciation, calculated along an adiabat with a potential temperature of 1200 °C. IW – oxygen fugacity equivalent to iron-wüstite buffer. Modified after (D. J. Frost & McCammon, 2008).*

Common solutes in mantle fluids include chlorides of alkali and alkali earth metals (Izraeli et al., 2001; Keppler, 2017; Manning & Aranovich, 2014). Among them, sodium chloride is the most common solute in the shallow lithosphere, especially in subduction zones (Manning, 2018; Yardley & Bodnar, 2014), with salt concentrations commonly on the level of brines (Frezzotti & Ferrando, 2015, 2018). However, at deeper conditions, fraction of potassium chloride in the fluids increases (Frezzotti et al., 2012), as indicated, for example, by fluid inclusions trapped in diamonds (e.g. Izraeli et al., 2001; Klein-BenDavid et al., 2004, 2007).

Another significant component of deep aqueous fluids is carbon. A plethora of reduced and oxidized carbon species (Sverjensky et al., 2020; Tiraboschi et al., 2022) are theorized to be present in the upper mantle, of which CO_2, CO and CH_4 probably are geochemically most relevant (D. J. Frost & McCammon, 2008). A possible carbon species in the upper mantle is undissociated carbonic acid, $H_2CO_{3(aq)}$ according to several numerical (Stolte & Pan, 2019; Sverjensky, Stagno et al., 2014) and experimental (F. Huang et al., 2017) studies.

Molecular hydrogen H_2 usually constitutes only a small fraction of the upper mantle fluids (Fig. 1.2). Bali et al. (2013) observed that at higher H_2 contents, a miscibility gap with H_2O may open . A reduced immiscible phase may contain CH_4 as well (Y. Li, 2017). Hydrogen may have been a dominant component of the fluid phase early in Earth's history, before the mantle became more oxidized (Bali et al., 2013; Sharp et al., 2013).

1.4. Aims of the thesis

The main goal of the thesis is to elucidate the details of previously underexplored physico-chemical aspects of aqueous fluids. Three inter-related topics were investigated, the electrical conductivity of KCl-bearing aqueous fluids, the stability of the acetate in subduction zone fluids and the effects of H_2-H_2O immiscibility (Fig. 1.3).

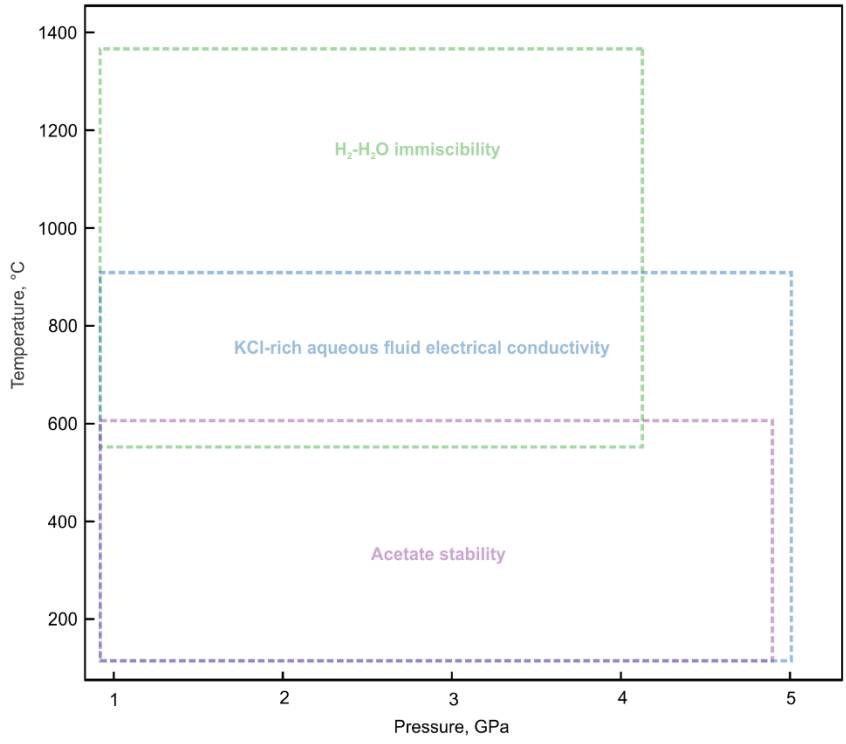

Figure 1.3. *Pressure-temperature ranges of three experimental projects contained within the thesis.*

Salt-bearing fluids conduct electricity and this effect directly depends on the presence and quantity of ions. Thus conductivity itself is mostly a function of salt concentration, the degree of dissociation of the solute, and ion mobility, with the two latter parameters depending on the value of the dielectric constant and the density of water (H. Guo & Keppler, 2019; Sinmyo & Keppler, 2017). As the electrical conductivity of NaCl aqueous solutions at elevated pressures and temperatures has already been explored in previous studies, the new data for KCl-rich fluids will allow to constrain not only the properties of water itself, but in addition various aspects of the behavior of alkali metal chlorides in aqueous solutions. To obtain this information, the electrical conductivity of 1, 0.1 and 0.01 M (mole per liter) KCl solutions were measured in a hydrothermal diamond anvil cell to 700 °C and 2 GPa and in piston-cylinder apparatus to 900 °C and 5 GPa. The data obtained are not only of fundamental interest, but can be applied directly for the interpretation of magnetotelluric survey data.

A number of recent theoretical studies proposed that carboxylic acid anions, such as acetate (Sverjensky, Stagno et al., 2014) or formate (Stolte et al., 2021) are significant constituents of deep aqueous fluids. If such compounds are indeed stable in the Earth's upper mantle, this may lead to a completely new subset of possible chemical reactions and geochemical processes involving carbon. The second aim of this thesis was to experimentally verify the prediction of acetate stability in subduction zone fluids, by performing hydrothermal diamond anvil cell experiments to 600 °C and 5 GPa.

The third aim of the thesis was the determination of the position of the critical curve in the H_2-H_2O system from 1 to 4 GPa and the detection of possible element partitioning effects on unmixing. This critical curve was initially investigated several years ago for the interval of 1.75 - 2.7 GPa (Bali et al., 2013). No data about element partitioning between water and hydrogen at deep Earth conditions have been available so far. Information on the behavior of xenon upon unmixing and the improved data on the position of the critical curve were used for assessing the processes of early degassing of our planet and the oxidation of the upper mantle.

2. Electrical conductivity of fluids in the KCl-H_2O system to 5 GPa and 900 ˚C

2.1. Introduction

Potassium chloride is a common solute in various natural aqueous fluids. While the main salt component in crustal and shallow subduction zone fluids is sodium chloride (Manning, 2018; Yardley & Bodnar, 2014), multiple lines of evidence indicate that mantle fluids are often potassium-dominated (Frezzotti et al., 2012). Most of such evidence comes from the study of mantle rocks affected by metasomatism (Dawson, 2012; O'Reilly & Griffin, 2013), but there are also direct samples of high-density fluids (HDF) trapped in diamonds (e.g. Izraeli et al., 2001; Rege et al., 2010). While fluids released by dehydration of subducted slabs will be rich in NaCl, upon percolation through the mantle, the K/Na ratio will increase as K is much more incompatible than Na in normal mantle minerals (Izraeli et al., 2001). This is likely the origin of KCl-rich fluids in the upper mantle.

With salt concentrations typically at the levels of brines (Frezzotti & Ferrando, 2018; Frezzotti et al., 2012; Frezzotti & Touret, 2014), saline solutions are highly conductive at mantle conditions, as already demonstrated for NaCl-bearing fluids (H. Guo & Keppler, 2019). Zones of elevated conductivity possibly associated with saline fluids are detected via magnetotelluric surveys above subducting plates (Evans et al., 2014; Pommier & Evans, 2017) or in areas of ongoing lithospheric mantle metasomatism (Patkó et al., 2021). However, a very intriguing case of possible fluid presence in the lithospheric mantle comes from the Slave (Canada) and Kaapvaal (South Africa) cratons, were kimberlites, known to produce diamonds with potassic HDF's, coexist with conductive anomalies at estimated diamond formation depths.

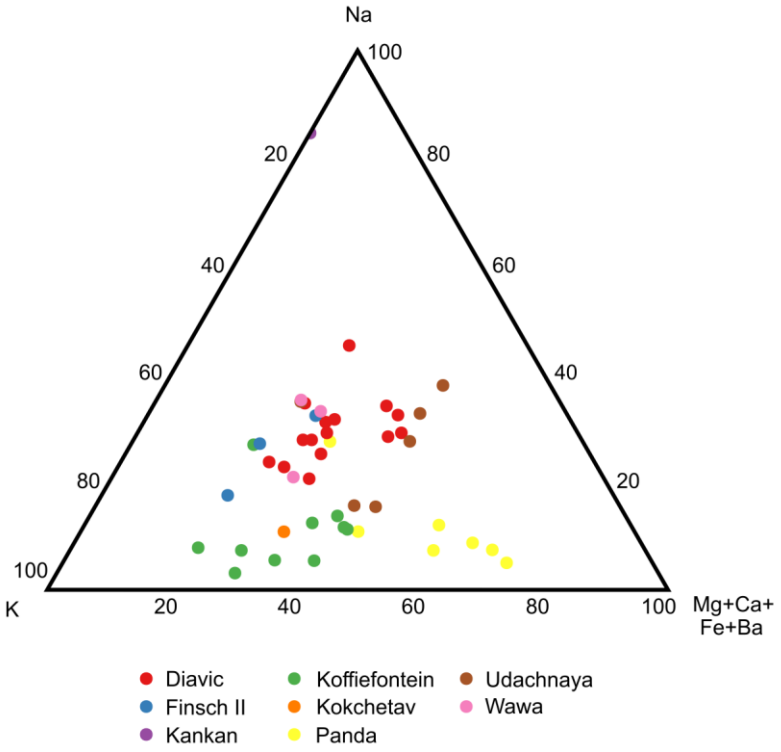

Figure 2.1. *Average and individual compositions of brine inclusions (in mol%) in diamonds from Diavic (Klein-BenDavid et al., 2004, 2007), Finsch II (Weiss & Goldstein, 2018; Weiss et al., 2014), Kankan (Weiss et al., 2014), Koffiefontein (Izraeli et al., 2001), Kokchetav (S. L. Hwang et al., 2005), Panda (Tomlinson et al., 2006), Udachnaya (Zedgenizov et al., 2007) and Wawa (Smith et al., 2012). Si: 0 – 7.9 mol%, Avg. 4.1 mol%; Cl: 21.9 – 52.1 mol%, avg. 37.7 mol%.*

In the interior of the Slave craton, a highly conductive zone, known as the Central Slave Mantle Conductor (Jones et al., 2001, 2003), with resistivity of 10-15 Ω·m originates at 80-120 km and descends to ~200 km. The Eocene kimberlite field is located above this conductor with the Diavic (Klein-BenDavid et al., 2004, 2007) and Panda (Burgess et al., 2009; Tomlinson et al., 2006; Tomlinson & Müller, 2009) kimberlites providing samples of potassium-rich fluids from ~150-200 km. Similarly, in the lithospheric mantle of the Kaapvaal craton, multiple mantle conductors (Evans et al., 2011) may be explained by the presence of fluids. Mineralogical evidence suggests the migration of potassic fluids (Konzett et al., 2013), in agreement with inclusions from diamonds of the Koffiefontein (Izraeli et al., 2001, 2004) and Finsch Group II kimberlites (Weiss &

Goldstein, 2018; Weiss et al., 2014), see Figure 2.1. The conductors at 80-200 km depth below the Dharwar craton (Kusham et al., 2021; Kusham et al., 2018, 2019) are another possible case with diamondiferous kimberlites present at the craton, but no "direct sampling" of fluids reported so far. On the other hand, there are samples of potassic fluids from kimberlite diamonds of Jwaneng in Botswana (Schrauder et al., 1996; Schrauder & Navon, 1994) and Udachnaya in Russia (Zedgenizov et al., 2007), but those areas are not yet covered by large-scale magnetotelluric surveys.

KCl-rich fluid inclusions have been reported not only from kimberlitic diamonds, but from metamorphic ones as well. Such samples were discovered in ultra-high-pressure (UHP) rocks of the Kokchetav UHP complex, where diamonds with potassium-rich HDF's (Dobrzhinetskaya et al., 2005; Hwang et al., 2005) occur together with ample evidence of fluid and melt-related metasomatism (Mikhno et al., 2014; Schertl & Sobolev, 2013). High-pressure potassic hydrous phases, such as K-cymrite (Mikhno et al., 2014; R. Y. Zhang et al., 2009) or maruyamaite (Lussier et al., 2016) found in the Kokchetav rocks may transport both water and potassium deep into the mantle. Though this particular terrain may not be representative for UHP metamorphism in general, it provides a valuable example of a possible scenario that may apply even to current zones of continental crust subduction (e.g. Seno & Rehman, 2011).

Numerical interpretation of magnetotelluric data, e.g. a direct estimate of the amount of possible fluid or melt in the mantle and its concentration, requires electrical conductivity data measured at mantle conditions (Pommier, 2014). Yet for potassium chloride-rich aqueous fluids such measurements have not been reported.

Being a standard solution for electrochemical cell calibration, KCl aqueous solutions are well studied at low pressures and temperatures, with an extensive compilation of more than a hundred years of measurements provided by Corti et al. (2008). Unfortunately, the majority of the data from this summary was collected for very dilute solutions (< 0.01 m or < 0.075 wt%), as part of limiting molar conductance studies, and is not very useful for geological purposes. Electrical conductivity values for solutions with KCl content in the range of naturally occurring fluids were reported by J. U. Hwang at al. (1970) (0.12-3.96 m, 0.89-22.8 wt%) and Sharygin et al. (2002) (0.001-4.5 m, 0.0075-25.12 wt%), but the maximum P-T conditions achieved by both studies are 600 °C and 300 MPa. Mangold and Franck (1969) managed to successfully measure 0.01 m KCl solution to 1000 °C and 1386 MPa. However due to technological limitations, more extreme

conditions remained experimentally inaccessible until recently. Based on newly developed high-pressure high-temperature electrochemical techniques, this study presents electrical conductivity measurements of 0.075 to 6.96 wt% solutions to 900 °C and 5 GPa, covering a wide range of possible lithospheric mantle conditions and fluid concentrations.

2.2. Experimental methods

2.2.1. Overview of the experimental strategy

The general experimental procedure is similar to the one adopted by H. Guo and Keppler (2019) in their study of the conductivity of aqueous NaCl solutions. Firstly, the conductivity of KCl solutions was measured in a restricted range of pressures and temperatures (up to 2.5 GPa and 675 °C) using externally-heated diamond anvil cells (DAC) with two metal gaskets as electrodes, separated by a perforated diamond platelet. Based on these data, a first numerical model of fluid conductivity as a function of density, temperature, concentration and limiting molar conductivity was calibrated. Secondly, data were acquired with a piston-cylinder (PC) electrochemical assembly up to 5 GPa and 900 °C. In these experiments, the conductivity of an aggregate of diamond powder with the KCl solution in the pore space was measured. In order to extract the pure fluid conductivity, the effective fluid fraction in this aggregate has to be calibrated. This could be done at ambient conditions after the run or under pressure in the low-temperature region, where conductivity changes only slightly with pressure. The latter approach was applied here, by modest extrapolation of the electrical conductivity model from the DAC experiments. H. Guo and Keppler (2019, their Fig. 4b) demonstrated that this approach yields results that are in excellent agreement with a calibration after the run at ambient condition.

The procedure used in this study results from the technological limitations of the two experimental setups. The DAC electrochemical cell allows to access a limited pressure-temperature range but yields data with good precision. The PC cell may cover a wider range of pressures and temperatures, but requires external conductivity values for low temperature calibration.

2.2.2. Diamond anvil cell electrochemical assembly

Fluid conductivities up to 2.5 GPa and 675 °C were measured in DAC using an assembly similar to that developed by Ni et al. (2014), see Figure 2.2a. A Bassett type externally-heated diamond anvil cell (Bassett et al., 1993) with 0.7 mm culet type I diamonds and two iridium gaskets, separated by a diamond platelet, was loaded with the fluid of choice and measured. The cell was heated by two molybdenum coils around the tungsten carbide diamond seats. Temperature was measured with a precision of ± 5 °C by two type K thermocouples in contact with the upper and lower diamonds. During the experiment, the cell was flushed with an Ar-H_2 (2%) mixture to prevent heater oxidation.

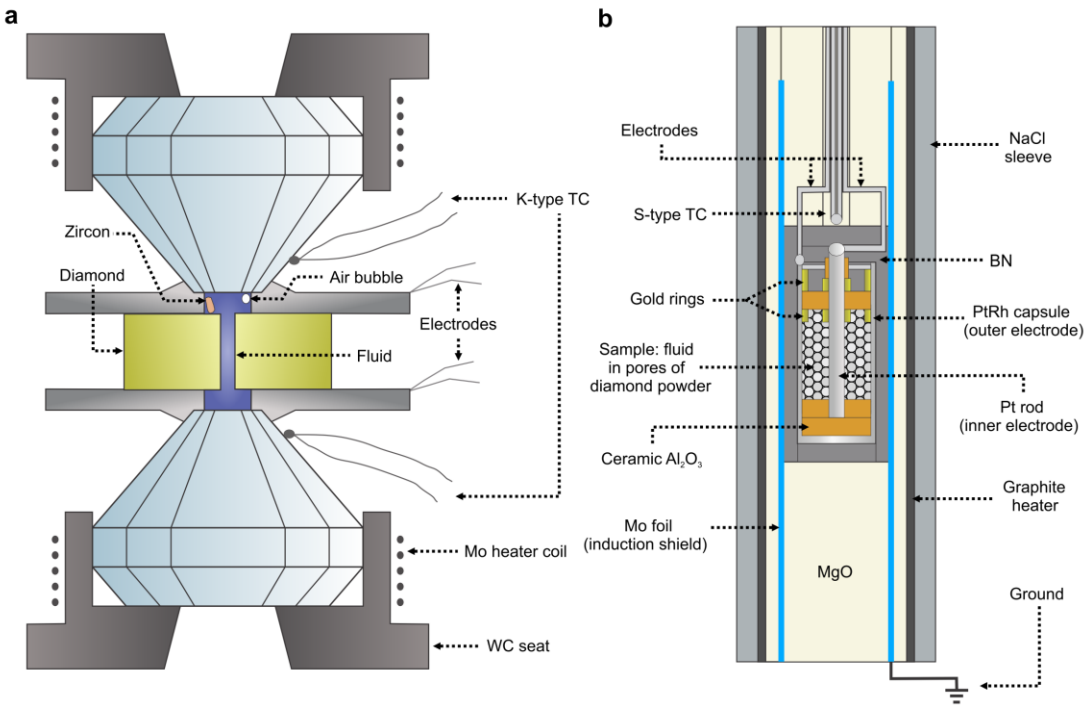

Figure 2.2. *Devices used for electrical conductivity measurements at high pressure. (a) Externally heated diamond cell with two electrodes separated by perforated diamond platelet. (b) Piston-cylinder electrochemical cell, based on a standard ½'' assembly. Note the gold rings introduced to improve sealing.*

Two types of insulating diamond platelets were used: (a) single crystal synthetic CVD diamond (0.3 mm thickness, 0.7 mm diameter, 50-µm pinhole) and (b) polycrystalline "HIME-DIA" diamond (Irifune et al., 2003) (0.5 mm thickness, 1.5 mm diameter, 100-µm pinhole). We achieved

maximal pressures of 2.5 GPa with the single crystal diamonds without failure. Iridium gaskets were 250 μm thick, doubly polished, with a hole ranging from 300 μm to 150 μm, depending on the target pressure of the experiment. Before the run, drilled gaskets were pre-indented using a solid diamond disc to significantly reduce cell deformation.

Natural zircon crystals (Sri Lanka, annealed at 900 °C for 20 h) placed in the upper cell chamber were used as pressure sensors (C. Schmidt et al., 2013), with pressure being calculated based on the shift of the 1008.1 cm^{-1} Raman band. The cell was loaded with 1, 0.1 or 0.01 M KCl conductivity standards (Fluka Analytical, 1 M stands for a concentration of 1 mol/l at standard conditions), equivalent to 6.96, 0.74 and 0.075 wt% KCl concentrations used later throughout the text. The gaskets served as electrodes and were connected by two wires each to the Solartron-1260 impedance analyzer after closuring the cell. Finally, fluid density was adjusted by varying the size of the bubble in the cell.

Raman spectra necessary for pressure calculation were collected with a Horiba Labram 800 HR UV confocal Raman spectrometer using the 514 nm line of an argon laser at 100 mW output power, an 1800 mm^{-1} grating and a confocal pinhole of 100 μm. In some experiments, where the location of the pressure sensor did not allow to measure the band shift due to diamond platelet luminescence, fluid density was determined based on the homogenization temperature (vapor bubble disappearance). Usually the difference between homogenization and nucleation (vapor bubble reappearance on cooling) temperatures was 5 °C or less, which implies isochoric behavior and allows to calculate pressures based on the equation of state of pure water (Wagner & Pruß, 2002).

For converting measured bulk resistances R to fluid conductivity σ, some calibration of the cell constant is required:

$$K_{cell} = \sigma_{fluid} * R_{bulk} \quad \text{(Eq. 2.1)}$$

Closed cells were calibrated at ambient conditions using the known conductivities of KCl solutions at room temperature (Y. C. Wu et al., 1991). Mostly, K_{cell} depends on the geometry of the pinhole in the diamond platelet, with a lesser contribution from the distances between the hole and the electrodes. The latter, as noted previously by Sinmyo and Keppler (2017), is affected by the cell deformation. However, the use of pre-indentation, due to rigidity of iridium, allowed to almost

completely eliminate that effect with the cell constants measured before and after experiment differing by less than 5%. A comparable factor that contributes to the K_{cell} determination error is the limited precision of temperature measurements during the calibration process itself, due to the precision of the K-type thermocouples and their placement. The conductivity of the 0.075 wt% KCl at 20 °C and at 25 °C differs by 10% and a possible error introduced by just moving the experimental assembly from one room to another probably exceeds the K_{cell} value drift due to changes in geometry.

2.2.3. Piston-cylinder electrochemical assembly

Unfortunately, the mechanical properties of the diamond platelets and iridium gaskets limit the pressure-temperature range accessible with the DAC setup. To expand it to 5 GPa and 900 °C, we used a separate piston-cylinder apparatus assembly, based on the standard ½'' NaCl-MgO piston cylinder cell design and the same KCl standard solutions. Originally developed to explore the electrical conductivity of melts by Ni, Keppler, Manthilake et al. (2011) it was modified and adapted for fluids by H. Guo and Keppler (2019).

The $Pt_{95}Rh_5$ capsule and a central Pt rod serve as electrodes and a layer of diamond powder (40-60 μm grain size, Alfa-Aesar), filled with a fluid, is located between them (Fig. 2.2b). The rod is held in place by ceramic alumina discs, with the top one also serving as a sealing cap for a diamond trap. A layer of pyrophyllite below the capsule cap seals the setup and the cap is insulated from the rod by a ceramic alumina sleeve. For this study, gold rings above and below the top ceramic alumina ring were added, to provide better sealing between the ring and the capsule wall.

A friction correction of 5% was applied to the nominal pressure, according to calibration of the quartz-coesite transition at 790 °C (Bose & Ganguly, 1995). The cell is protected from the inductive effect of the heater by a Faraday cage, made out of 0.125 mm thick molybdenum foil. An S-type (Pt-$Pt_{90}Rh_{10}$) thermocouple was used for temperature measurements.

Fluid conductivity can be extracted from the measured bulk cell resistances. This may be demonstrated by an application of the Hashin-Shtrikman upper bound (HS^+) model (Hashin & Shtrikman, 1962) that describes the bulk conductivity of a fluid-solid aggregate as a function of the individual phase conductivities and the fluid fraction, with the assumption that the fluid forms an interconnected network:

$$\sigma_b = \sigma_f + \frac{3(1-\emptyset)\sigma_f(\sigma_d - \sigma_f)}{3\sigma_f + \emptyset(\sigma_d - \sigma_f)} \quad \text{(Eq. 2.2)}$$

where σ_b is the bulk conductivity of the aggregate, Ø the fluid fraction, σ_f is the fluid conductivity and σ_d is the conductivity of diamond. Previous studies (Vandersande & Zoltan, 1991) demonstrate that the electrical conductivity of diamond within our experimental range is very low, ranging from 10^{-14} S/m at 25 °C to 10^{-4} S/m at 900 °C, and thus can be neglected relative to σ_f without introducing significant errors. This yields

$$\sigma_b = \sigma_f \left(1 - \frac{3(1-\emptyset)}{3-\emptyset}\right) \quad \text{(Eq. 2.3)}$$

Equation 2.3 demonstrates that fluid conductivity can be calculated based on measured bulk conductivity of the cell if the fluid fraction and cell physical dimensions are known. While the cell geometrical parameters can be measured directly, the fluid fraction estimation is complicated. A way to estimate it was proposed by H. Guo and Keppler (2019), based on HS^+ model applied to the post-run measurements of the assembly at ambient conditions, or alternatively, by a calibration under pressure at low temperatures, where the pressure effect on fluid conductivities is small.

Therefore, our bulk measurements were evaluated based on the extrapolation of the KCl conductivity model obtained through DAC measurements. As Equation 2.3 remains valid at any temperature and pressure, the cell constant can be evaluated at any experimental conditions if fluid conductivity is known. Though our electrical conductivity model was established on the data up to 2.5 GPa and 675 °C, the model itself suggests that at 400 °C the pressure influence on conductivity is quite minor and the extrapolation would not contribute significantly to the overall error of the measurement. Thus:

$$K_{cell} = \sigma_{400} * R_{400} \text{ (Eq. 2.4)}$$

where σ_{400} is calculated based on Equation 2.5 (see below) and R_{400} is measured directly.

2.2.4. Impedance data acquisition and treatment

For both experimental devices, impedance was measured from 1 MHz to 2 kHz or less using a Solartron-1260 impedance analyzer, with a voltage amplitude of 700 mV. The accuracy in resistance measurements with this instrument is specified by the manufacturer as 0.1% for the range of 10 Ω to 100 kΩ at 10 kHz.

Despite major constructive differences, the impedance response of both the PC and the DAC electrochemical cells is governed by the same physicochemical principles. Each of them features two noble metal electrodes separated by comparable distances (1.7 mm and ~1 mm respectively) and the same type of fluid. Diamond powder, present in the PC assembly, does not contribute to the measured conductivity according to Equation 2.3, providing only a non-reactive framework. This statement is supported by tests at ambient conditions that demonstrated the same type of impedance response in a PC assembly filled with fluid without diamond powder (Ø = 1) and with diamond powder containing variable fluid fractions.

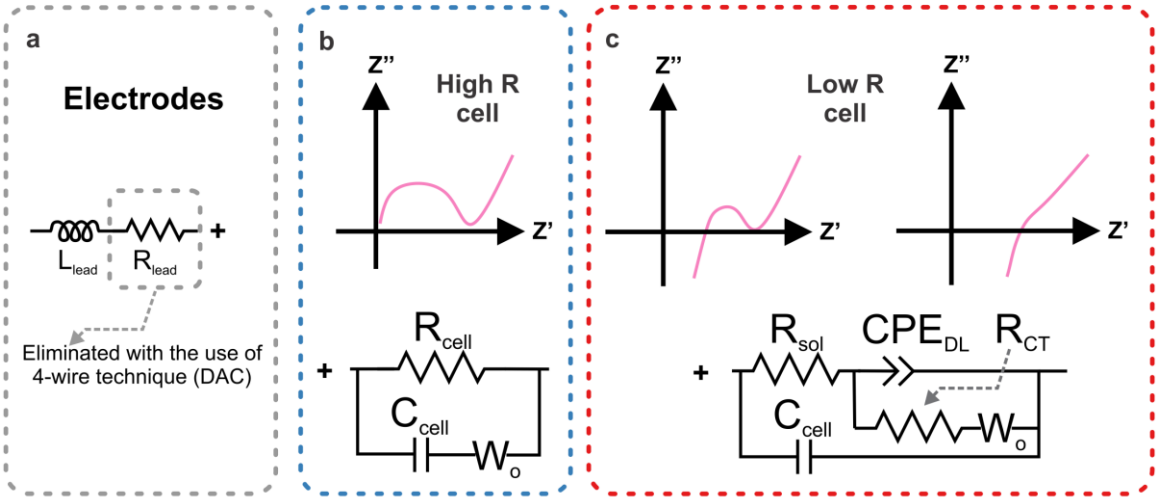

Figure 2.3. *General equivalent circuit, modelling the impedance responses of electrochemical setups used in this study: (a) simplified circuit representing the response of the electrodes; (b) cell of high resistance (R, Ω) e.g. response of the cell containing KCl solutions of low concentration or a mixture of saline ice and diamond powder; (c) cell of low resistance (R, Ω) e.g. response of the cell containing KCl-rich fluid in the pores of diamond powder. Each given cell is a combination of a) and b) or a) and c), depending on the conditions.*

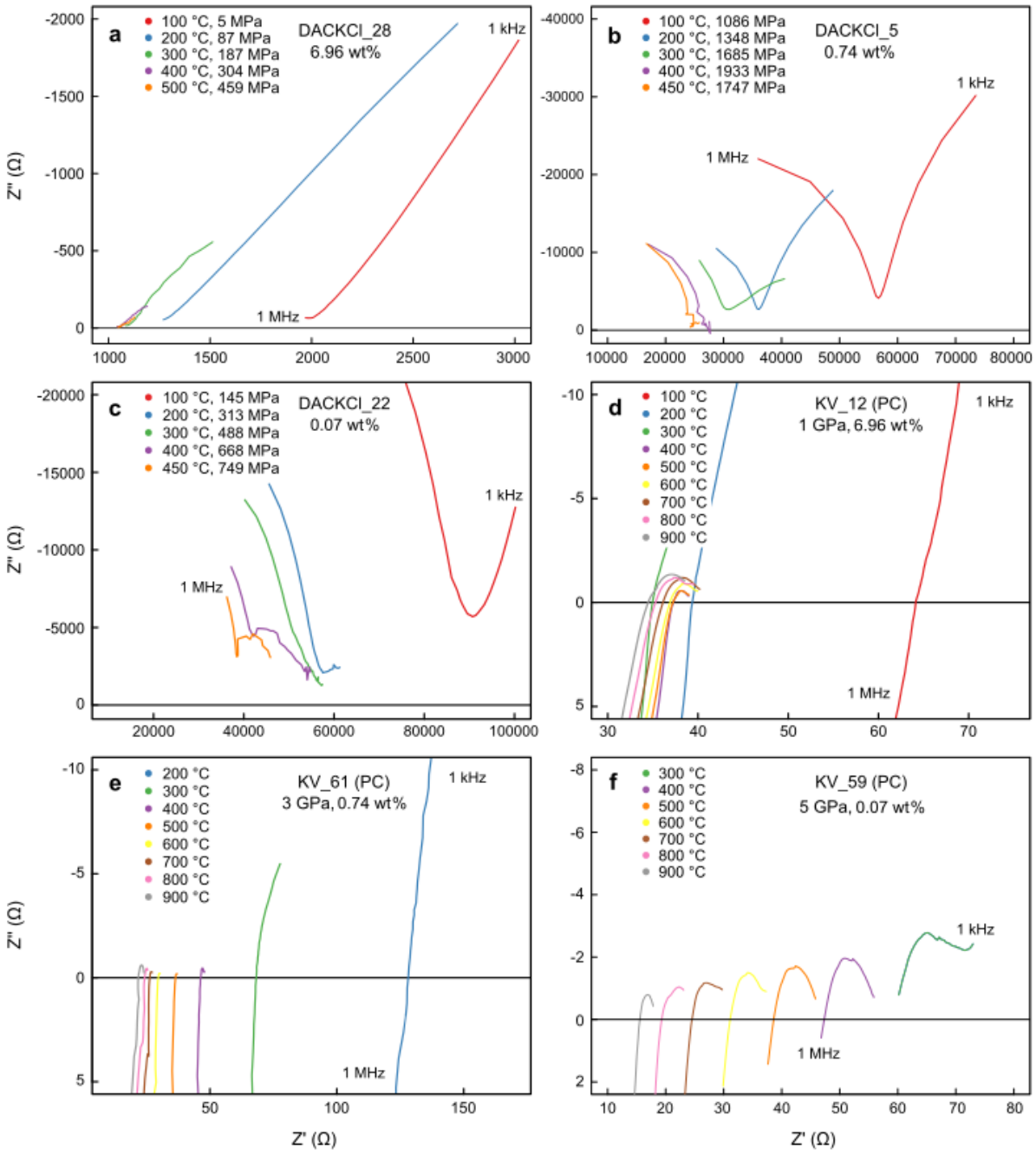

Figure 2.4. *Nyquist plots for impedances measured in: (a-c) DAC assemblies, (d-f) PC assemblies. Analog circuits and fitting results for selected measurements presented here are available in Figures A1-A7 and Table A5 in the Appendices.*

The full impedance response of a system consisting of two noble metal electrodes and a binary aqueous electrolyte is traditionally described by an equivalent model circuit known as a Randles

cell (Barsoukov & Macdonald, 2005; Lvovich, 2015; Randles, 1947). Figure 2.3 shows a slightly modified version of it, which we adopted to interpret the observed impedance responses from our assemblies (Fig. 2.4).

L_{lead} and R_{lead} (Fig. 2.3a) describe the contribution of the lead wires to the measured impedance. Both of those values depend on the physical parameters of the electrodes, connecting the cell and the measuring device. The DAC setup utilizes 4-wire measurements and therefore allows to avoid the R_{lead} contribution, with lead length of only ~7 cm, which significantly lowers L_{lead}. In theory, the 4-wire setup also allows to avoid the lead inductive contribution. However, this is rarely achieved in real high pressure-high temperature experiments due to the length and placement and imperfect connections of the wires (Savova-Stoynov & Stoynov, 1987). Measurements of the PC electrochemical cells were performed with a 2-wire technique (lead length of ~60-25 cm) and required correction for lead resistances, that were collected before the runs using a short-circuit procedure (Ni, Keppler, Behrens, 2011).

A response from the electrochemical cell itself (Fig. 2.3 b,c) consists of the following parts: R_{sol} is solution resistance, C_{cell} is the geometric capacitance of the cell, CPE_{DL} is a capacitance of the electrochemical double layer modelled with a constant phase element, R_{CT} is charge transfer resistance and W_o is an open Warburg element. C_{cell} in case of both assembly types is governed by the placement and area of the opposing electrodes as well as dielectric properties of all materials contained between them. The CPE_{DL} and R_{CT} contributions are not resolved on impedance diagrams if $R_{sol} >> R_{CT}$ and a small semi-arc corresponding to electrode polarization appears on Nyquist plots only at elevated temperatures as fluid resistance decreases. Thus, for cells with high sample resistance those elements can be omitted (Fig. 2.3b). The Warburg impedance, attributed to charge diffusion in the electrolyte or ice, is present in all acquired data, however it is not always perfectly and completely resolved in high temperature data as it occupies the region of low frequencies (< 1 kHz-100 Hz) that is prone to various interference such as noise from the heating circuit. The main purpose of this model is to describe the features observed in impedance measurements performed in the field of liquid water stability. Below freezing temperature, the right part of the circuit, corresponding to the cell impedance response, turns into a true parallel arrangement of the resistor and capacitor (Fig. 2.3b), as expected for a polycrystalline solid. This phase transition is an important part of the measurement procedure at high pressures, however we do not report any saline ice conductivity values as it is beyond the scope of the present thesis.

Not all elements of the aforementioned model can be precisely extracted from our impedance data, as the cell designs and experimental conditions vary significantly. However, the solution resistance (R_{sol}), which is the only variable relevant for this study, can always be reliably obtained with the accuracy of < 0.1 Ohm. To achieve this, we fitted measured impedances using simplified versions of our analog circuit model, which feature main elements observed in each particular case. For example, C_{cell} was commonly omitted from the simplified models due to induction, and the low-frequency Warburg element was modelled as a parallel arrangement of CPE and R with arbitrary large resistance. Typical examples for the different kinds of fits used for both diamond anvil cell and piston cylinder impedance spectra are given in Figures A1 – A2 with fitting parameters available in Table A5 (see Appendices).

2.3. Results

2.3.1. Conductivity measurements in the DAC assembly

Data collected across all three concentrations of potassium chloride in the DAC-based electrochemical assembly was compiled into a data set (Table A1 in the Appendices). Densities were calculated based on the known pressures from the equation of state by Wagner and Pruß (2002).

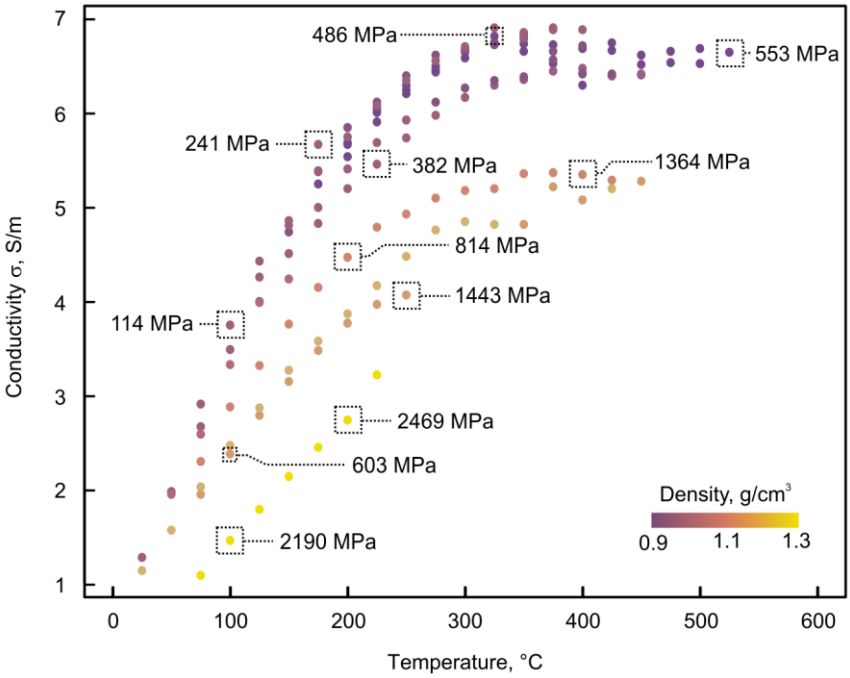

Figure 2.5. *Electrical conductivities of the 0.74 wt% KCl as functions of density and temperature.*

Part of that data set, representing the conductivities of 0.74 wt% KCl fluid, can be seen in Figure 2.5. In general, increasing KCl concentration increases conductivity. Values measured for 0.075 and 0.74 wt% solutions differ approximately tenfold, with the ratio between 0.74 and 6.96 wt% values being slightly smaller. This can be attributed to a decrease in the degree of KCl dissociation with the increase of the concentration itself.

For all concentrations, within the temperature-density range of our experiments, we observe two effects that have an opposing influence on conductivity: σ increases with the increase of temperature and decreases with the increase in density. The temperature effect can be explained with the increase in ion mobility at elevated temperatures (Marshall & Frantz, 1987; Quist & Marshall, 1968).

At fixed temperature, the increase in pressure and therefore in density leads to two opposing physical effects. Firstly, increasing density increases the dielectric constant, which is a factor promoting dissociation of KCl into K^+ and Cl^-. Higher dissociation means that more charge carriers are available in the solution and the conductivity rises. This effect is obvious at low temperatures and low densities. For example, at 300 °C, an increase in fluid density up to 0.9 g/cm^3 leads to a gradual increase in conductivity. However, increasing fluid density impedes ion mobility and above 0.9 g/cm^3 this effect reduces conductivity (Mangold & Franck, 1969). This data set was used to produce a numerical model, describing the electrical conductivity of the KCl aqueous fluid in crustal conditions as a function of density, concentration, temperature, and limiting molar conductivity.

2.3.2. Conductivity model for KCl-bearing aqueous fluids in the crust

We used the diamond anvil cell data to calibrate a model for predicting electrical conductivities of KCl-H_2O fluids in the crust. This model will also be used for the low temperature calibration of piston-cylinder fluid conductivity measurements. As shown by Sinmyo and Keppler (2017) in their study of NaCl-bearing fluid, the following model yields a very good agreement with experimental measurements:

$$\log \sigma = A + B * T^{-1} + C * \log c + D * \log \rho + \log \Lambda_0 \quad \text{(Eq. 2.5)}$$

where σ is the conductivity of the fluid, T is the temperature in Kelvin, c is the concentration in weight percent, ρ is the density of pure water at given P and T in g/cm^3, Λ_0 is a limiting molar conductivity at infinite dilution in S·cm^2·mol^{-1}. Coefficients A, B, C, D are determined by least squares regression of the DAC experimental data set. While temperature, concentration and density are known parameters for any particular composition and conditions, Λ_0 at those conditions needs to be calculated separately. Mangold and Franck (1969) demonstrate in their study of the limiting molar conductivity of KCl aqueous fluid that with increasing density, the value of Λ_0 decreases linearly within the range studied (from 0.7 to 1.2 g/cm^3). Increasing temperature increases Λ_0 up to 400 °C, but has very little effect above 400 °C. Thus, the limiting molar conductivity can be described by the following empirical model:

$$\Lambda_o = \lambda_1 + \lambda_2 * \rho + \lambda_3 * T^{-1} + \lambda_4 * T^{-2} \quad \text{(Eq. 2.6)}$$

with coefficients λ_1- λ_4 being determined by a multiple regression fit of Λ_0 values provided by more contemporary measurements of Ho and Palmer (1997) and Sharygin et al. (2002). Performed in smaller range of densities and temperatures they appear to be more precise than the limiting molar conductivities provided by Mangold and Franck (1969) and Ritzert and Franck (1968). This choice of calibration data results in a better approximation of the high density and low temperature region.

The numerical fit obtained (R^2 = 0.956) yielded λ_1 = 1377 ± 187, λ_2 = -1082 ± 69, λ_3 = 6883*10^2 ± 2383*10^2, λ_4 = -2471*10^5 ± 752*10^5. Being mostly empirical, this equation provides best performance on data within its calibration range. This range fully encompasses the conditions of our DAC measurements and even most of the PC measurements. With Λ_0 given by Equation 2.6, a regression fit was carried out for Equation 2.5. To achieve best fit quality, the full set of our 6.96, 0.74 and 0.075 wt% KCl fluid electrical conductivity values (353 data points, Table A1 in the Appendices) was merged with the data for 0.075 wt% solution by Mangold and Franck (1969) (60 data points), to compensate for the decrease in precision of the method used at low concentrations. Since there is no data for Λ_0 available below 200 °C, we excluded values below 175 °C from the resulting data set (323 data points total) to avoid the influence of the increasing uncertainties of Equation 2.6 on our fit.

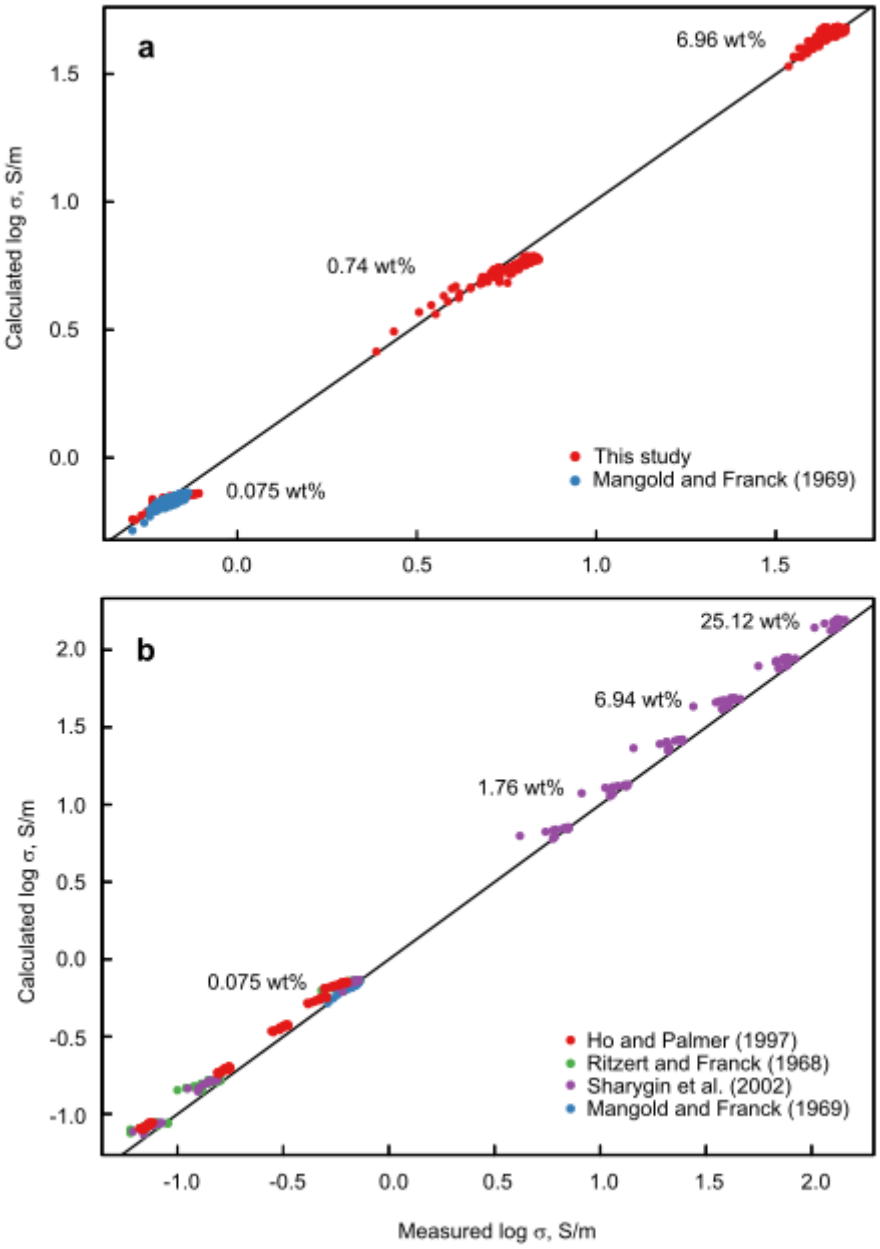

Figure 2.6. *Numerical model for KCl-H_2O fluid conductivity data from DAC measurements. (a) Comparison of measured fluid conductivities and values predicted by Equation 2.5. (b) Test of Equation 2.5 against existing fluid conductivity data ($\rho \geq 0.6$ g/cm^3). Measurements of Mangold and Franck (1969) (blue) used for the creation of the model are given as a reference.*

The fitting procedure (R^2 = 0.999) resulted in A = -2.03 ± 0.01, B = 25.0 ± 5.39, C = 0.923 ± 0.002, D = 0.990 ± 0.037. As seen from Figure 2.6a, these fit parameters provide valid conductivity predictions for all values within the specified range of DAC measurements.

To test the performance of the model we compared its predictions with KCl fluid conductivity measurements from three other studies (Ho & Palmer, 1997; Ritzert & Franck, 1968; Sharygin et al., 2002), see Figure 2.6b. For KCl concentrations up to 25.12 wt%, predictions appear to be quite accurate (347 data points, R^2 = 0.999) for measurements within the ρ-T-c range of our numerical model. Predictions strongly deviate from the measurements for ρ < 0.6 g/cm^3, but this is expected as these densities are far beyond our calibration data. For predicting conductivities in the shallow Earth´s crust at such low densities, Equation 2.5 should therefore be used with caution.

2.3.3. Conductivity measurements in the piston-cylinder assembly

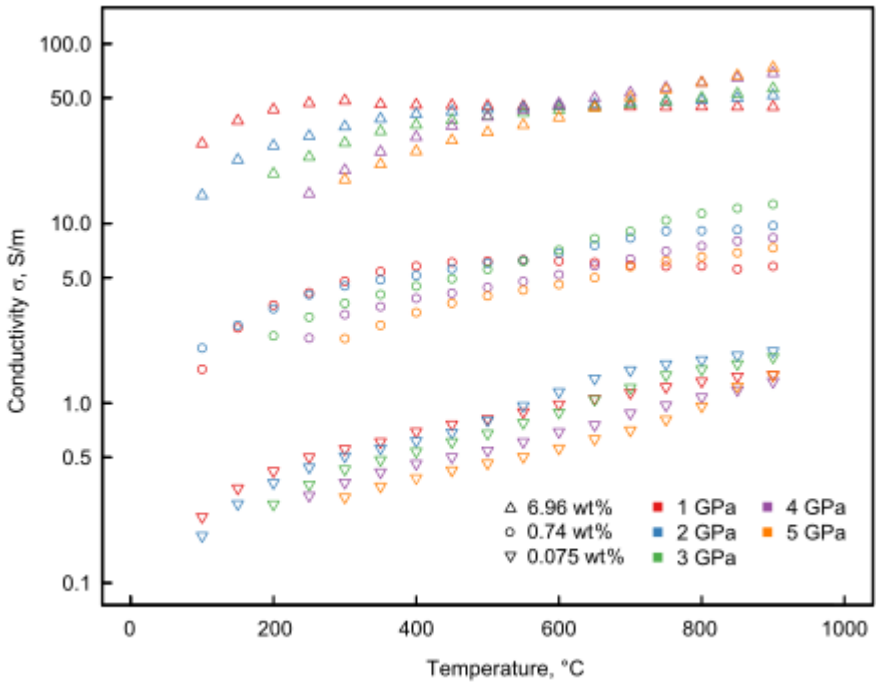

Figure 2.7. *Electrical conductivities of the 6.96, 0.74 and 0.075 wt% aqueous solutions measured in a piston-cylinder electrochemical assembly.*

With Equation 2.5 established, the K_{cell} for the piston-cylinder electrochemical cell was calculated, based on the fluid conductivity estimate at 400 °C. This calibration introduces only limited uncertainties, as the conductivity shows only a minor dependence on fluid density at 400 ˚C. Fluid conductivities in the whole measurement range from 100 to 900 °C and from 1 to 5 GPa were then calculated, assuming that the cell constant remained essentially the same at all temperatures. Measured cell resistances and compilation of resulting conductivity data are available in Tables A2 and A3 in the Appendices respectively. Figure 2.7 shows measured conductivities at some pressures as function of temperature.

As seen from Figure 2.7, the influence of pressure and temperature on the electrical conductivity of the H_2O-KCl fluids is the same as for data collected with the diamond anvil cell electrochemical assembly. With increasing density, fluid conductivity decreases below 550 °C due to the decrease in ion mobility. At 3, 4, and 5 GPa and below 200, 250, and 300 °C respectively, conductivities tend to differ very little for each concentration as the samples were mostly a mixture of ice and diamonds at those conditions (Journaux et al., 2013) and such measurements were omitted from the data set. Above 550 °C, for each pressure an increase in temperature generally increases conductivity. However, the maximum measured conductivity and the pressure at which this value is recorded appears to be dependent on the KCl concentration.

At higher pressures, the effect of the increased density on ion mobility seems to overpower the effect of the changing dielectric constant. While for 6.96 wt% KCl measured conductivities at 900 °C increase with pressure, for 0.74 and 0.075 wt% this is true only to 3 GPa and 2 GPa respectively. At higher pressures and for 0.74 and 0.075 wt% fluids, the value of conductivity tends to decrease. This effect was also previously observed in NaCl-containing fluids by H. Guo and Keppler (2019). For 6.96 and 0.74 wt% concentrations, the measured values at 1 GPa are in agreement with the DAC equation predictions. However, the corresponding values for 0.075 wt% KCl solution at temperatures above 500 °C tend to be ~20% higher than those measured by Mangold and Franck (1969). Due to the extremely low values of conductivities measured, it is difficult to provide a definitive explanation for this effect, as the data may be very sensitive to minor contaminations of the fluid and other effects.

To better constrain the KCl fluid conductivity, multiple experiments were carried out for each pressure of 6.96 and 0.74 wt% concentrations (see Tables A2, A3 in the Appendices). As illustrated by Figure A8 in the Appendices, for both concentrations the method produces very similar data.

For pressures of 3 GPa and above, the leakage of the assembly becomes a significant source of error. In general, each new cooling cycle in this method produces slightly higher resistances at high pressure and low temperatures due to fluid leaks, but that difference is normally within ~1 Ohm and does not affect the measurement outcome significantly – for any greater difference the experiment was discarded. For 1-2 GPa up to 4 heating-cooling cycles can be performed without any change in the quality of the measured resistances, for 3-5 GPa this number reduces to 3 cycles. While interpreting our data, we assume that the primary charge carriers in the fluid are K^+ and Cl^-, produced by KCl dissociation. As previously noted in the NaCl conductivity study by H. Guo and Keppler (2019), at highest pressures and temperatures the auto-dissociation of H_2O into H_3O^+ and OH^- may contribute to measured conductivities in a minor way. As parts of our electrochemical assembly are made of Al_2O_3 and Au, some contamination from the dissolution of those materials is theoretically possible. However, the solubility of gold in such dilute saline solutions during very short run times (< 10 h of heating per experiment) and their cyclic design is almost negligible (Hanley et al., 2005), with the same being true for the Al_2O_3. Though no study on corundum solubility in KCl fluid is readily available, the data presented in the study on NaCl (Newton & Manning, 2006) and KOH (Wohlers & Manning, 2009) fluids strongly support that statement.

2.3.4. Conductivity model for KCl-bearing aqueous fluids in the mantle

Our DAC conductivity measurements of H_2O-KCl fluids allowed us to establish a model covering a majority of possible crustal conditions. For expanding it to the elevated pressures and temperatures probed by the piston-cylinder technique, some adjustment is required. Thus, we performed the same least squares fitting procedure on the cleaned piston-cylinder measurements data set (462 data points), after removing several anomalous single measurements (e.g. KV46 & KV62_3 for temperatures > 750 °C) where the real experimental conditions may be different from those reported. As previously, limiting molar conductivity values were calculated using Equation 2.6 with the previously obtained parameter values. A least squares fit (R^2 = 0.986) yielded A = -1.52 ± 0.02, B = -357 ± 13.4, C = 0.865 ± 0.005, and D = 1.72 ± 0.06 , see Figure 2.8. For the high-pressure data, the model calibrated by the piston cylinder runs clearly reproduces the measurements better. However, the difference between these two models diminishes for elevated KCl concentrations, which are geophysically most relevant. More significant discrepancies between measured and predicted data, most notably for the equation using the fit parameters from

the DAC experiments, occur at the lowest KCl concentrations. This is in some ways expected as for such very dilute fluids and in particular for the highest pressures studied here, the solute may approach complete dissociation. In this case, some of the simplifications used by Sinmyo and Keppler (2017) in deriving equation 2.5 are not valid anymore.

If one compares the fit coefficients derived from the piston cylinder experiments with those from the diamond cell experiments, it is obvious that the coefficient C in front of the concentration term is very similar. However, there is a significant difference in the coefficients D for the density term and a particularly large difference in B, which describes the temperature dependence. This is because the fluid density itself also depends somewhat on temperature and therefore, there is some co-variance between the fit coefficients for the temperature and the fluid density term. At the lower pressures covered by the DAC fit, the effect of temperature on fluid density is much stronger than at the higher pressures covered by the regression fit from the piston cylinder data, which causes the difference in B and D. In the 1 - 2 GPa range, both equations reproduce the data generally well, but the piston cylinder calibrated equation should not be used below 1 GPa.

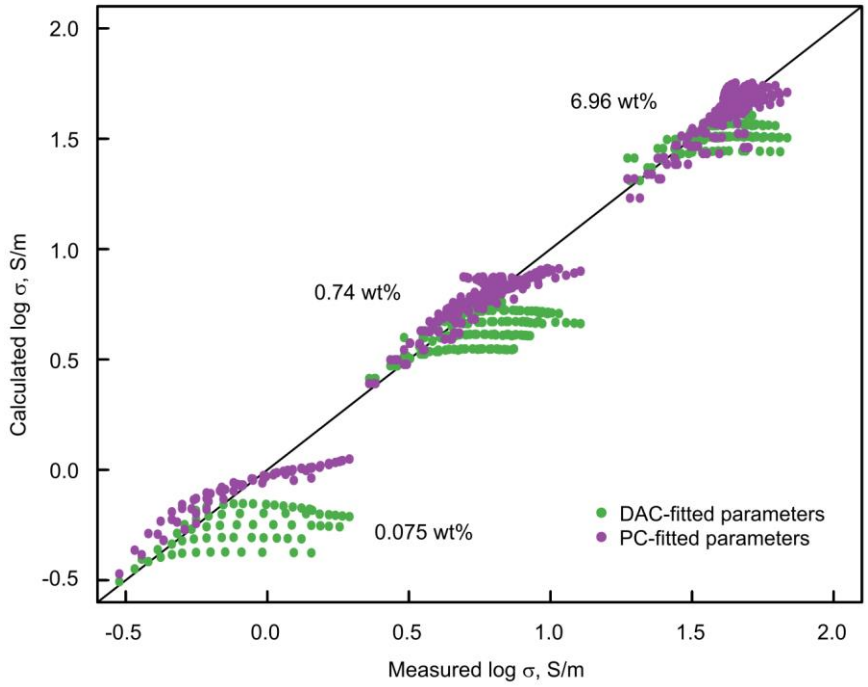

Figure 2.8. *Electrical conductivity of KCl-H_2O fluids measured in the piston cylinder apparatus and predicted by Equation 2.5, with fit parameters derived from DAC measurements (green) and from PC measurements (purple).*

For higher concentrations above 6.96 wt%, we do not have direct experimental data at high temperatures and pressures. Yet Figure 2.6b suggests that this type of model should provide reasonable results even for 25 wt% solutions, which may justify its use for concentrated brines.

2.4. Discussion

2.4.1. Comparison of the electrical conductivity of NaCl and KCl-bearing fluids

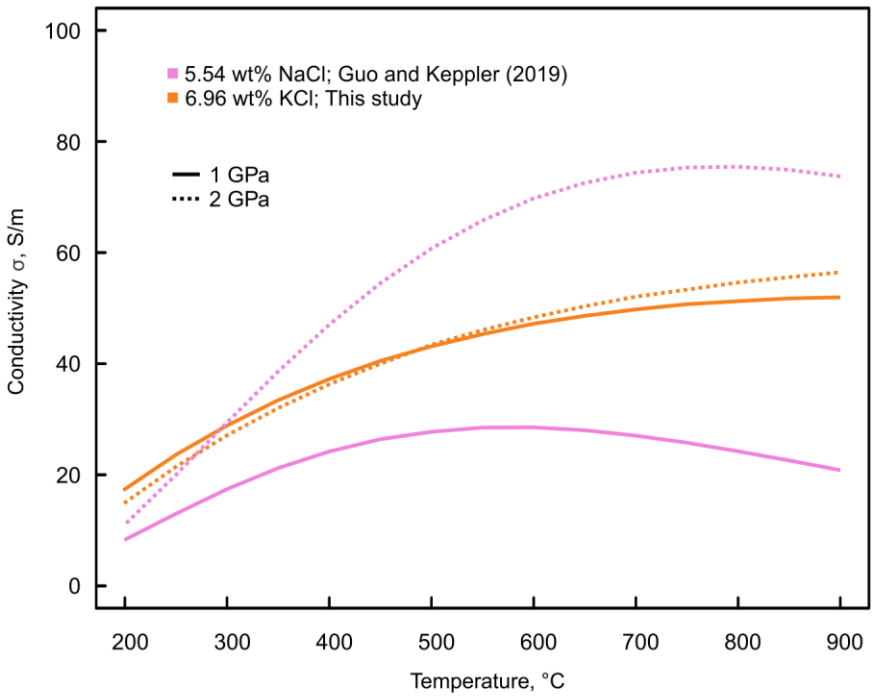

Figure 2.9. *Electrical conductivities of 5.54 wt% (1 M) of NaCl-H_2O fluids calculated based on the model of H. Guo and Keppler (2019) and 6.96 wt% KCl-H_2O fluid (1M, this study, piston-cylinder model) at 1 and 2 GPa. 1 M refers to a concentration of 1 mol per liter at standard conditions.*

At ambient conditions, 1 M NaCl (5.54 wt%) and 1 M (6.96 wt%) KCl electrical conductivities are 8.5 and 10.9 S/m respectively (Weiner, 1960). This is somewhat surprising, as the ionic radius of Na^+ (0.97 Å) in aqueous solution is less than for K^+ (1.41 Å; Marcus, 1988) and without any additional factors the latter should be less mobile. However, in aqueous solutions, solvation shells are formed around ions. The solvation shell around the potassium ion was traditionally believed to

be smaller than the one around sodium, due to the smaller electrostatic field strength (charge/radius ratio) of K^+ (Nightingale, 1959). This concept was used to explain why K^+ is more mobile and more conductive than Na^+ in aqueous solutions at ambient conditions. However, more recent neutron diffraction data (Ohtomo & Arakawa, 1980) suggest that the nearest ion-oxygen distances around Na^+ (2.5 Å) and K^+ (2.7 Å) in aqueous solutions at ambient conditions are similar. The higher conductivity of KCl relative to NaCl at ambient conditions may therefore more be due to weaker interactions between K^+ and H_2O (Džidić & Kebarle, 1970) leading to shorter lifetimes of the associations between K^+ and H_2O molecules (Bakker, 2008). The difference between the conductivity of KCl versus NaCl in aqueous fluids at low pressure and at high pressure may be related to some structural change in the fluid. At low pressure, liquid water has a rather open (ice-like) structure with defined hydration shells around ions (e.g. Ohtomo & Arakawa, 1980). At higher pressures, this structure should break down to a more or less dense packing of oxygen atoms without defined hydration shells. Under these conditions, one would expect KCl to be less conductive than NaCl, because the larger ion (K^+) should move more slowly, consistent with our experimental observations.

Figure 2.9 compares electrical conductivities of NaCl and KCl-bearing aqueous solutions at elevated pressures and temperatures, calculated with PC-derived parameters from Equation 2.5 for 6.96 wt% KCl and from H. Guo and Keppler (2019) for 5.54 wt% NaCl. Similar to the situation at ambient conditions, the electrical conductivity of potassium chloride at 1 GPa exceeds that of sodium chloride by approximately a factor of two. However, at higher pressures and temperatures this relation reverses. While NaCl conductivity greatly increases with pressure, the effect on KCl conductivity is small. This may be attributed to a decrease or even loss of hydration shells around the Na^+ and K^+ ions, which may particularly increase sodium mobility as compared to potassium. Although some recent experimental and computational data on Na^+, K^+, and Rb^+ coordination and solvation shell structure at elevated pressure-temperature conditions exist (Filipponi et al., 2003; Rozsa & Galli, 2021; Sakuma & Ichiki, 2016; Yamaguchi et al., 2021), no measurements of the K^+ and Na^+ solvation shells at up to 5 GPa and relevant high temperatures were performed so far. However, a recent theoretical study by Fowler and Sherman (2020) indeed suggests that at high P and T (up to 4.5 GPa and 800 ˚C), the presence of NaCl has essentially no effect on water structure anymore, in agreement with the idea that at these conditions, ordered hydration shells around ions cease to exist.

2.4.2. KCl-rich aqueous fluid as possible electrical conductor in the upper mantle

Highly conductive zones (0.02-1 S/m, see Fig. 2.10, 2.11) detected by magnetotelluric surveys in the lithospheric mantle below cratons may be successfully explained by the presence of small (< 1 vol%) fractions of various fluids and melts, sulfide minerals, graphite films or hydrous olivine (Naif et al., 2021). Unless there is a localized heat source, the low lithospheric mantle temperatures (Hasterok & Chapman, 2011; Rudnick & Fountain, 1995) allow to safely rule out silicate melts and hydrated olivine (Naif et al., 2021). Minimal temperatures of 900-1000 °C necessary for the beginning of water-saturated peridotite melting (Katz et al., 2003) are achieved only at depth of 125-150 km (4-5 GPa) with fluids of variable silicate content (Ryabchikov et al., 1982) being present at more shallow depths. Based on a case of sulfide-containing Sierra Nevada xenoliths (Ducea & Park, 2000), an argument for small amount of sulfides as conductivity enhancing phase can be made. Yet there are significant obstacles for a widespread use of this phase for the interpretation of MT data, given it extremely high conductivity on the order of 10^4-10^5 S/m (e.g. Bagdassarov et al., 2009). Similar problems arise when attempting to interpret such conductive anomalies as zones containing graphite (~10^5 S/m) (R. B. Frost et al., 1989; Mareschal et al., 1992). Recent studies suggested that carbon films will not form interconnected networks, neither in crust nor in the lithospheric mantle (Yoshino & Noritake, 2011; B. Zhang & Yoshino, 2017), thus making them unlikely candidates. Melts and aqueous fluids, however, typically have conductivities on the order of 10^0-10^2 S/m at upper mantle conditions (Naif et al., 2021 and references within) and do not require improbably large volume fractions to explain the elevated conductivities below cratons. The carbonatite solidus, for example, is located at 500-800 °C at 2-5 GPa (Litasov et al., 2013) and hydrous carbonatites have conductivities on the order of 10^1-10^2 S/m along the cratonic geotherm (Yoshino et al., 2018), which makes them a plausible choice as conductive phase. Despite having even lower solidus temperatures (Journaux et al., 2013), higher conductivities (H. Guo & Keppler, 2019), and direct evidence from diamond inclusions, saline aqueous fluids are less frequently considered.

Elevated bulk rock conductivities as inferred by MT data can only be attributed to fluids, if they are interconnected at given conditions (Wannamaker, 2000; Yardley & Valley, 1997). While at lower crustal conditions the presence of fluid is currently debated (Manning, 2018; Naif et al., 2021; Yardley & Valley, 1997), in the upper mantle above 2 GPa and 1000 °C (Mibe et al., 1998), aqueous fluids may remain interconnected. Recent work, investigating the connectivity of mixed

H_2O-NaCl-CO_2 fluid in olivine aggregates, demonstrated that for such compositions the fluid is wetting grain boundaries even along a cool geotherm (Y. Huang et al., 2020). Starting from 50 km (1.5-2 GPa) and 750 °C, the dihedral angles were experimentally found to be less then 60°.

To investigate KCl-rich aqueous fluids as a possible conducting phase in lithospheric mantle of cratons, we calculated possible fluid fractions with Hashin and Shtrikman (1962) upper bound (HS^+) model for several known conductive anomalies (Fig. 2.10, 2.11) using Equation 2.5 with PC-fitted set of parameters (exact model values are available in the Appendices, Table A4). NaCl-bearing fluid (H. Guo & Keppler, 2019) and hydrous carbonatite (Yoshino et al., 2018) fluid fractions are calculated as well for comparison. Peridotite conductivity is estimated from the model of Gardés et al. (2014). Fluid salinities of 5 and 10 wt% were chosen for the model. Frezzotti and Touret (2014) constrain upper mantle fluid salinity at 5-50 wt% in NaCl equivalent, specifying that the lowest values (<15 wt% NaCl eq.) are observed for inclusions with high concentration of CO_2 , an prominent component of diamond fluid inclusions. We do not provide estimates for higher salinities on Figure 2.10, but in general, a salinity increase would almost inversely proportionally decrease the calculated fluid fraction. As an example, the fluid fraction necessary to explain a 0.03-0.1 S/m mantle conductivity at 3.1 GPa (100 km) and 750 °C (Fig. 2.10, (a) – 2) by a 10 wt% NaCl or KCl fluid would be 0.02-0.07 vol% and 0.07-0.21 vol%, while a 20 wt% concentration would require 0.01-0.04 vol% and 0.04-0.12 vol% respectively.

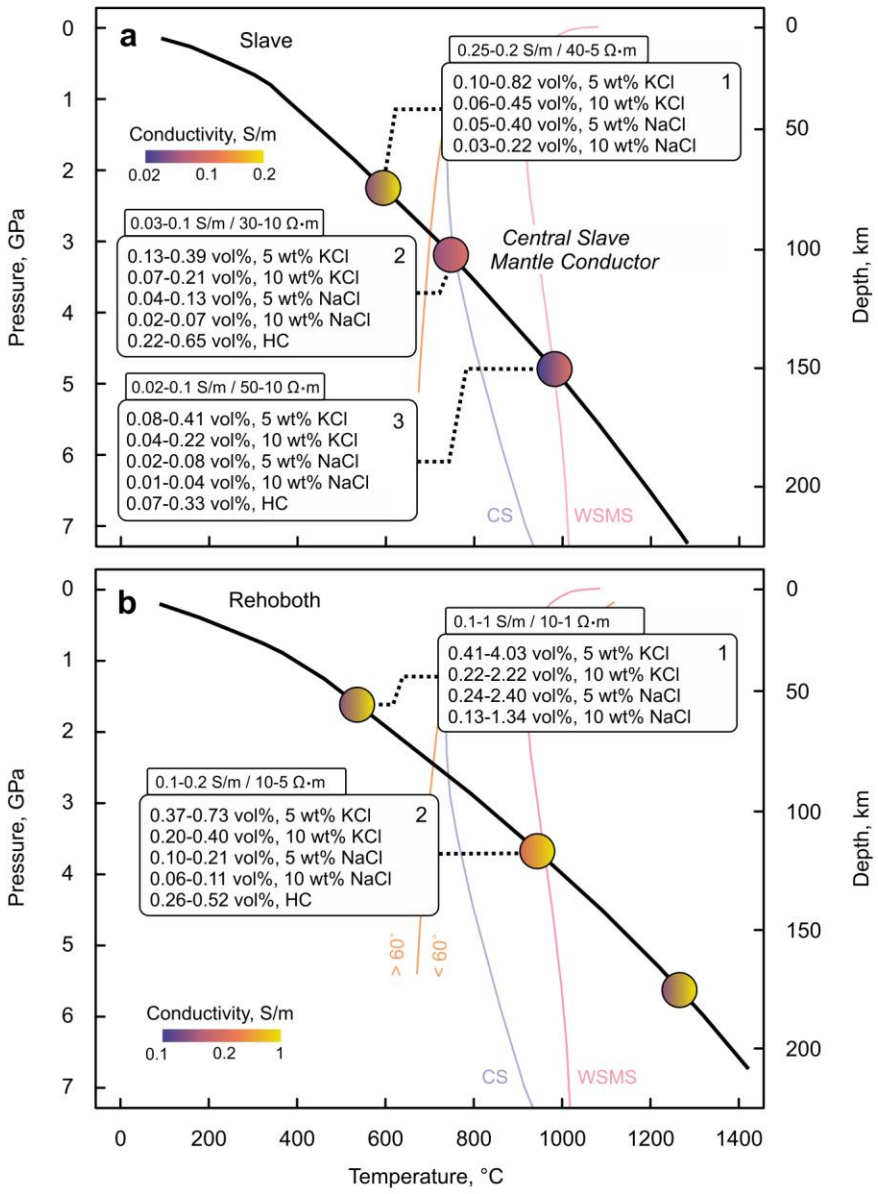

Figure 2.10. *Fractions of various non-silicate fluids, required to explain electrical conductivity anomalies below (a) Slave craton (MT data from Jones et al. (2001, 2003), geotherm from Russell and Kopylova (1999), (b) Rehoboth terrane and Kaapvaal craton (MT data from Evans et al. (2011) and Jones et al. (2009), geotherm from Rudnick and Nyblade (1999)). Gradients inside the circles on diagrams represent lateral variations in conductivity at given depth at geotherm temperature. HC – hydrous carbonatite melt (Yoshino et al., 2018), CS – coldest possible potassic carbonatite solidus from Litasov et al. (2013), WSMS – water saturated mantle solidus from Katz et al. (2003), the dashed orange line is the 60° dihedral angle isopleth (Y. Huang et al., 2020).*

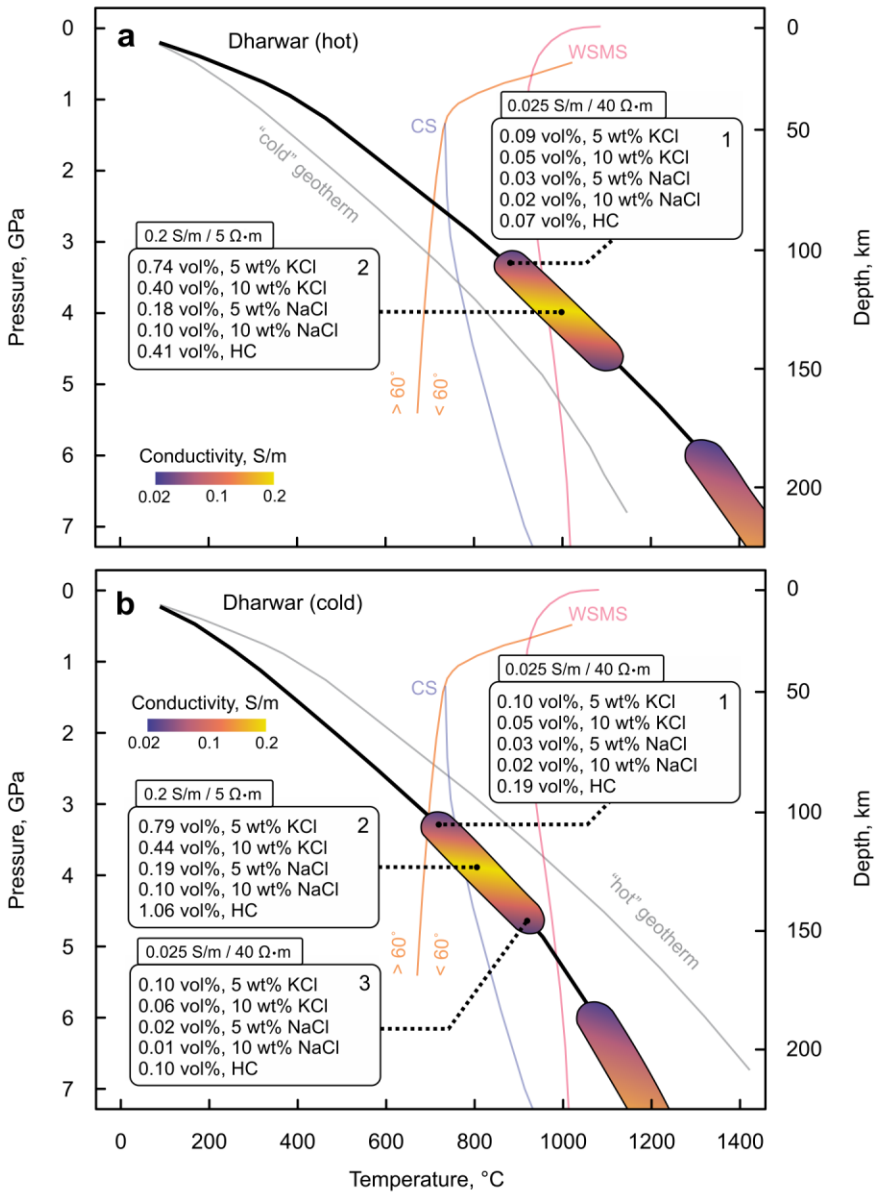

Figure 2.11. *Fractions of various non-silicate fluids, required to explain electrical conductivity anomalies below Dharwar craton (MT data from Kusham et al. (2018, 2019), with "hot" (Rudnick & Nyblade, 1999) (a) and "cold" (Gupta et al., 1991) (b) geotherms. Colored areas on diagrams are vertical cross-sections of conductivity anomalies with each shade representing single conductivity value at given depth and temperature. HC – hydrous carbonatite melt (Yoshino et al., 2018), CS – coldest possible potassic carbonatite solidus from Litasov et al. (2013), WSMS – water saturated mantle solidus from Katz et al. (2003), the dashed orange line is the 60° dihedral angle isopleth (Y. Huang et al., 2020).*

2.4.3. Conductivity anomalies in the lithospheric mantle of cratons

As noted in the introduction, there is very good evidence from fluid inclusions in diamonds suggesting the widespread occurrence of KCl-bearing fluids in the cratonic mantle. We will therefore explore here the possible contribution of such fluids to observed zones of elevated conductivities. To qualify as a possible location of KCl-bearing aqueous fluids, a conductive area needs to satisfy several important criteria. (i) The fluid needs to remain interconnected i.e. it has to form dihedral angles below 60°. As there are no data for KCl-bearing fluids, we use the 60° isopleth for NaCl-CO_2-H_2O from the study of Y. Huang et al. (2020) as the best approximation. (ii) The region has to be below the water-saturated mantle solidus. Depending on the geotherm, those two conditions define a narrow window of 700-1000 °C and 3-5 GPa or 100-150 km. These considerations effectively exclude some of the deep hot anomalies, shown in Figures 2.10 and 2.11 as an example without calculated fluid fractions, and some of the shallower anomalies like Figure 2.10 (a) & (b) – 1. For the extremely conductive zone (> 1 S/m) in the Rehoboth terrane, sulfides may perhaps be a plausible explanation, as there is evidence for mantle sulfides from Kaapvaal (Alard et al., 2000). (iii) Another criterion, which makes KCl-bearing aqueous fluids a natural choice, is to be below the carbonatite solidus. This criterion defines a region in the lithospheric mantle where such fluids are the most probable choice for explaining elevated conductivities: 3-3.5 GPa below 800 °C. This requires a cooler geotherm, as for the Slave craton, where the Central Slave Mantle Conductor (CSMC) (Fig. 2.10, (a) – 2) is located approximately at those pressures and temperatures. For this particular case, numerous potassic saline fluid inclusions from Panda and Diavik diamonds (see section 2.1, Fig. 2.1) provide additional evidence for the presence of KCl-bearing aqueous fluids. The 60° isopleth almost exactly matches the upper border of the CSMC, which is additional evidence for the involvement of aqueous fluid.

In hotter regions of the mantle, KCl-bearing aqueous fluids may also be present. Estimates from Panda inclusions suggest 930-1010 °C as diamond formation temperature. However, at those temperatures, carbonatites would also be a plausible option as highly conductive phase. Our calculations suggest that based on conductivities alone a distinction between carbonatites and saline fluids is not possible. Hydrous carbonatites and 5-10 wt% KCl fluids require almost identical fluid fraction at cratonic geotherm conditions (Fig. 2.10, 2.11). Interestingly, for the majority of fluid inclusion populations in diamonds, saline high density fluids coexist with carbonatites (e.g. Klein-BenDavid et al., 2004, 2007; Navon et al., 1988; Schrauder & Navon, 1994) and form a

continuous series of intermediate compositions. Therefore, both phases may perhaps contribute to the conductive anomalies.

In general, as illustrated by Figures 2.10 and 2.11, accounting for even the most conductive parts of subcratonic upper mantle typically requires less than a volume percent for any of the examined fluids. At the depth below 75 km the most conductive phase is NaCl-rich fluid with the fluid fractions in the order of 10^{-2} vol%. A comparison of saline solution fractions for two Dharwar craton geotherms (Figure 2.11 (a) & (b)) shows that for both the colder one (Gupta et al., 1991) and the hotter one (Rudnick & Nyblade, 1999), the required volume fractions for KCl and NaCl-bearing aqueous fluids at same depth are very similar, showing little dependence on temperature change within 150 degrees. The fluid fraction required for hydrous carbonatite, for comparison, changes by more than a factor of two – from 1.1 vol% to 0.4 vol%.

The fluid fractions calculated here are based on the conductivity data for pure NaCl-H_2O or KCl-H_2O fluids. Actual mantle fluids may dissolve some additional silica component and this may increase the viscosity of the fluid and thereby reduce ion mobilities. There is some support for this effect from the comparison of NaCl-H_2O fluid conductivity data (Sinmyo & Keppler, 2017) with conductivity data in polyphase systems containing saline fluids (X. Guo et al., 2015; Shimojuku et al., 2014). However, direct viscosity measurements of silica-bearing aqueous fluids suggest only a minor viscosity increase for plausible silica contents in mantle fluids (Audétat & Keppler, 2004). We therefore estimate that our calculated fluid fractions should be accurate within a factor of two.

If saline aqueous fluids are indeed responsible for some of the conductivity anomalies as discussed above, they need to be in some kind of thermodynamic equilibrium with the surrounding mantle assemblage. Moreover, fluid ascent by gravitational instability has to be limited by some mechanism. We propose that there are plausible mechanisms how fluids may be highly connected without being able to ascent rapidly. This is possible if the fluid connectivity is mostly horizontal, with little vertical connectivity. Experimentally, such structures have been produced by deformation in partially molten rocks (Holtzman, 2016). Moreover, the wetting properties of olivine are certainly anisotropic and it is therefore conceivable that in a deformed peridotite with lattice preferred orientation of mineral grains, fluid connectivity will also be anisotropic. There are two lines of evidence supporting this idea: (i) Experimental measurements of the dihedral angle in the olivine-H_2O-NaCl system suggest values that are rather close to the critical angle of 60° (Y. Huang et al. 2020). But they also show - for the same P,T conditions - a rather wide spread. This

is at least partially due to the effects of anisotropy, implying that for some crystal faces, the value may actually below 60°, while it is above 60° for other crystal faces under the same conditions. A lattice preferred orientation of olivine crystals in the mantle could therefore very well produce fluid connectivity only in one (e.g. horizontal) direction. (ii) Seismic data provide strong evidence for the presence of small degrees of partial melt in the form of tubes or thin films of nearly horizontal orientation near the lithosphere-asthenosphere boundary (e.g. Rychert et al., 2021). The stabilization of such connected melt structures over geologic timescales poses the same problems as for fluids as it requires that the vertical connectivity and the buoyant ascent of the melt has to be somehow reduced or suppressed. The lattice preferred orientation of olivine and other mantle minerals, as it results from mantle convection, together with the anisotropy of wetting properties could offer here a plausible explanation. An alternative possibility could be that aqueous fluid is constrained to depths where it forms an interconnected network and it cannot ascent any further, because the wetting properties of the fluid become unfavorable at low pressures corresponding to more shallow depths. Indeed, the data of Y. Huang et al. (2020) suggest that for NaCl-bearing fluids, such a change in connectivity occurs in the shallow mantle (see the orange line in Fig. 2.11). However, the intersection of this line with the geotherm (Fig. 2.11) is not always at the right depth for stabilizing a fluid in the region where elevated conductivity is observed.

Thermodynamic equilibrium between a saline fluid and the nominally anhydrous minerals of the upper mantle is also possible, if one considers that in such a fluid the activity of water may be greatly reduced. The NaCl-H_2O system at high pressure has a strong negative deviation from ideality, which increases with pressure, as the degree of dissociation of NaCl increases (e.g. Manning & Aranovich, 2014). For KCl, which is more dissociated than NaCl, this effect should be even stronger. Moreover, at mantle pressures and temperatures, the solubility of silicate species in the water is very significant, which further reduces water activity. Both effects together will tend to destabilize hydrous phases and reduce water solubility in nominally anhydrous minerals, such that a saline fluid containing some dissolved silicates may well be in stable equilibrium with a mostly anhydrous mantle assemblage. Moreover, the bulk water content of conductive mantle regions may well be elevated above average bulk mantle water contents. This is completely consistent with data on water contents in mantle xenoliths, which show quite a large regional variation (e.g. Demouchy & Bolfan-Casanova, 2016).

2.5. Conclusion

In this work we present improvements to previously proposed high-temperature – high-pressure electrochemical cells, allowing more accurate electrical conductivity measurements, as well as a detailed equivalent circuit that allows to interpret such data. Based on those methodological developments we investigated the electrical conductivities of KCl-H_2O fluids and proposed two conductivity models: one for crustal conditions (to 2.5 GPa and 675 °C) and one for the upper mantle (to 5 GPa and 900 °C). Using these models, we interpreted a class of known lithospheric mantle conductive anomalies as possible zones containing traces of KCl-bearing fluid. Comparing our data with previously measured conductivities of NaCl -bearing aqueous fluids reveals that at high pressures and temperatures NaCl-bearing fluid of same molality is significantly more conductive than KCl-bearing. This may be caused by major changes in the hydration shell structure.

3. The critical curve in the H_2O-H_2 system

3.1. Introduction

Hydrogen speciation in the interior of planets depends on oxidation state. For example, in the top part of Earth's lithospheric upper mantle, oxygen fugacity $f(O_2)$ ranges from +2 to -3 log units relative to the quartz-fayalite-magnetite buffer (ΔQFM) (Ballhaus, 1993; D. J. Frost & McCammon, 2008). Such conditions are typically considered as relatively oxidizing for the mantle, with the primary hydrogen species being molecular H_2O or bound hydroxyl groups (OH^-). At greater depths and pressures, exceeding 200 km and 5-7 GPa respectively, oxygen fugacity evolves towards more reducing values, approaching the iron-wüstite (IW) buffer with relatively little further deviation (1-1.5 log units) (D. J. Frost & McCammon, 2008). As the environment becomes more reducing, the fraction of water in fluids decreases and molecular hydrogen H_2 as well as methane CH_4 become primary H-species. Recent studies indicate that in the more reduced parts of the mantle, H_2 may not only be present in a free fluid phase, but also as dissolved species in minerals and melts (Hirschmann et al., 2012; Yang et al., 2016).

While the depth-dependent fugacity profile described above holds true for the majority of the contemporary mantle environments, there exist a number of local, though geologically significant exceptions such as super reducing domains, with mineral assemblages recording log $f(O_2)$ significantly below IW buffer. A characteristic phase, most commonly cited as an indicator of such super-reducing environments is moissanite (SiC). It is widely accepted that moissanite formation requires extremely low oxygen fugacities with log $f(O_2)$ approximately 5-8 units below the IW buffer (e.g. Golubkova et al., 2016; Ulmer et al., 1998). In the past, the natural origin of moissanite has been frequently questioned. However, it has now been discovered *in situ* in a wide range of geological settings - kimberlites and lamproites (Kaminsky, 2012; Shiryaev et al., 2011), ophiolites (Golubkova et al., 2016; Pujol-Solà et al., 2018; Trumbull et al., 2009), alkaline basalt tuffs (Dobrzhinetskaya et al., 2018), and syenites (Nazzareni et al., 2019). In super-reducing mineral assemblages, moissanite is commonly associated with native iron, silicon, various alloys, wüstite, phosphides and nitrides. Traditionally, such phases were thought to originate at great depth (< 200-250 km), where conditions are expected to be more reducing. While this may be so in some cases, Bali et al. (2013) suggested that super-reducing conditions can emerge even at 100-

200 km depth from the percolation of hydrogen-rich fluids, produced via unmixing in the H_2-H_2O system.

Today, Earth's upper mantle is quite oxidized and comparatively cold (e.g. Abbott et al., 1994; Herzberg et al., 2010). However, at the dawn of the Archean, its oxidation and thermal state used to be dramatically different. This is especially true for the first two hundred million years of Earth's history. During and immediately after core formation, as indicated by existing models (Rubie et al., 2011), Earth's interior was very reduced, perhaps 4-5 log units below the IW buffer. Throughout this stage, our planet, as well as Mars and Venus, may have had a hydrogen-rich atmosphere, supported by magma ocean outgassing (Lammer et al., 2018). However, for Earth, the upper mantle remained reduced at most for about 200 Myr. Based on the oxygen fugacity estimates of Trail et al. (2011), the redox state of the upper mantle was already close to that prevailing today at 4350 Myr before present. An early oxidation of the upper mantle has been noted for Mars as well, suggesting that it may be a common phase of the evolution of the terrestrial planets (Tuff et al., 2013).

The short timescale of the oxidation event points towards a fast process responsible for it. While the exact mechanism is still under discussion (Armstrong et al., 2019; Williams et al., 2012), the emergence of the miscibility gap between water and hydrogen upon cooling of the mantle was considered as a plausible cause (Bali et al., 2013). Global degassing of a highly mobile and buoyant H_2-rich phase could have rapidly oxidized the remaining mantle. Moreover, it would certainly have affected the mantle abundances of other elements, especially noble gases, such as xenon or argon. An early loss of radiogenic ^{129}Xe and of xenon isotopes by plutonium fission has indeed been reported (Kunz et al., 1998), but linking it to H_2-H_2O unmixing requires the knowledge of partition coefficients between water and hydrogen at reduced upper mantle conditions that are currently missing from the literature.

In this chapter, I present new data on the position of the critical curve in the H_2-H_2O system from 1 to 4 GPa together with some first experiments on element partitioning between the two coexisting fluid phases. The data will be applied to better understand the formation of ultra-reducing domains and the processes of mantle degassing during the first stages of Earth´s history. Moreover, the data also provide insights into the interior state of Neptune, Uranus (Bergermann et al., 2021), and H_2O-rich planets in general.

3.2. Experimental methods

3.2.1. Starting material and capsule preparation

Small crystal cylinders (diameter 2.2 mm, length 1 mm), used for trapping fluid inclusions, were cut out of bulk pieces of pure natural quartz (Brazil) and of synthetic and natural (Dac Lac, Vietnam) forsterite. Cylinders were thermally cracked by heating them to 1000 °C in a furnace and then immediately dropping into distilled water. For experiments performed at pressures below 2.5 GPa, quartz was used to trap the inclusions, with forsterite being the choice for this and greater pressures. This change of the host crystal is necessary due to the quartz-coesite transition at temperatures of interest, which transforms the single crystal of quartz into a polycrystalline aggregate of coesite unsuitable for trapping inclusions (Lathe et al., 2005).

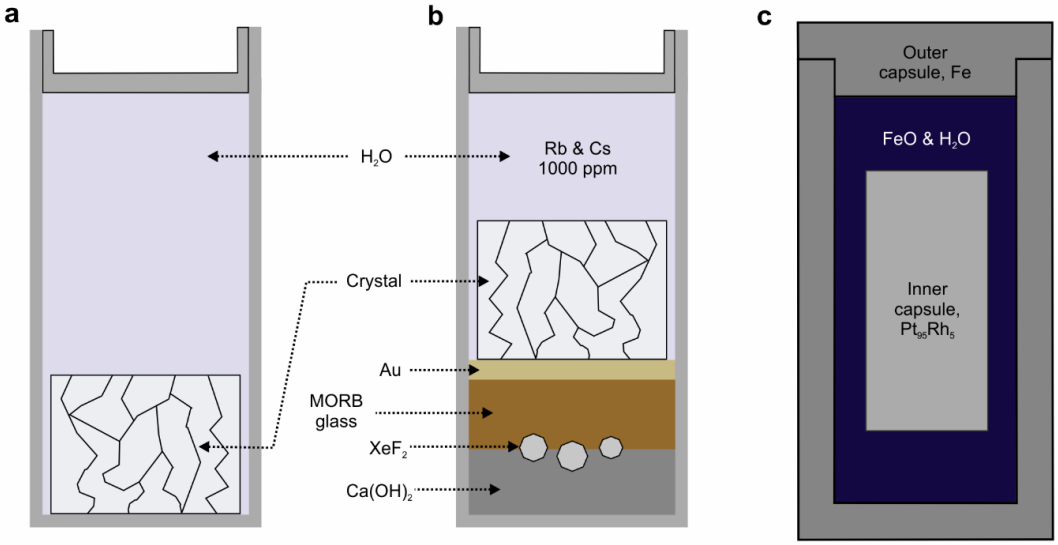

Figure 3.1. *Design of double capsules used for experiments. (a) and (b) show details of inner capsules, (c) shows the entire double capsule. For experiments used to locate the critical curve, inner capsule type (a) was used, while (b) was used for element partitioning experiment. Diagrams are not on scale.*

A double capsule technique was used to buffer the oxygen fugacity at the Fe-FeO equilibrium, to contain hydrogen during the experiment, and to protect the crystals from Fe contamination. In several early test runs of critical curve position determination experiments the forsterite crystal core was loaded directly into the buffering mixture (Fe + FeO), without the inner capsule. We found out that with olivine, this method cannot be utilized at temperatures above 1100-1200 °C in

the selected pressure range due to the precipitation of Fe-rich brucite and pure iron that complicate the analysis of H_2 and H_2O in the fluid inclusions. Two low temperature (900 and 1000 °C) 3 GPa samples produced in this way were used in the present study, as they show no signs of the aforementioned additional solid phases. For the rest of the experiments in this study an inner capsule was used, regardless of the crystal type. Depending on the specification of the run – critical curve position determination or element partitioning experiments – only the contents of the inner capsule differed, with the rest of the assembly remaining unchanged and being generally similar to the technique utilized by Bali et al. (2013).

For experiments to determine the position of the critical curve, the inner $Pt_{95}Rh_5$ capsule (outer diameter 2.5 mm, inner diameter 2.3 mm, length 5-6 mm) contained only the crystal cylinder, with the rest being filled up with ultrapure water (Millipore, σ = 0.06 μS) (Fig. 3.1a). For element partitioning experiments the, capsule was filled from bottom to top in the following sequence: a layer of $Ca(OH)_2$ (Merck, >96 %), XeF_2 crystals (Alfa Aesar, 99.5 %), a layer of synthetic diopside-glass powder doped with about 25 trace elements at the 0.5 - 1 wt. % level (Rustioni et al. 2019), Au foil (24 carat, Noris Blattgoldfabrik), the crystal cylinder, and ~10 μl of water containing 1000 ppm of both Rb and Cs (Fig. 3.1b). The solution, replacing pure water in this type of capsule, was prepared by the addition of RbCl (chemPUR, 99.9 %) and CsCl (chemPUR, 99.99 %) to the distilled water. Here, Xe and Rb/Cs are introduced for use as internal standards during later analysis, assuming that they would be incorporated primarily into the H_2 and H_2O phases, respectively. The $Ca(OH)_2$ layer binds excess fluorine, released during the XeF_2 decomposition in the presence of H_2O, in the form of CaF_2. This prevents the formation of HF as an undesired component. The thin gold membrane insulated H_2O from XeF_2 during the capsule preparation process, in order to avoid premature decomposition.

After the addition of the crystal and water or solution the capsule was micro-welded (Lampert PUK U3, 9 % power, 6 ms). To avoid overheating and water loss, the top cap of the capsule had ~0.5 mm long edges that were pressed toward the capsule wall with plyers before welding. Subsequently, the cap was filled with distilled water, which was refilled throughout the welding process to always fully cover the cap bottom. The capsule itself was sitting in a cooling jacket made of wet paper tissue. Based on weighing and test openings of the welded capsules this technique allows to achieve similar results as the one proposed by Audétat and Bali (2010) and

used in the original Bali et al. (2013) study. However, it allows to more efficiently pack the capsule, which is critical for the complex capsule design in the element partitioning experiments.

Following the welding procedure, the inner capsule was inserted into the outer capsule machined of Fe (GoodFellow, 99.8%, outer diameter 5 mm, inner diameter 3 mm, length 10 mm) together with a mixture of distilled water and FeO (Sigma-Aldrich, 99.7 %) that ensured Fe-FeO buffer conditions (Fig. 3.1c). This inner capsule was closed by inserting the lid and mechanically sealed on compression.

3.2.2. Piston-cylinder experiments

Experiments were carried out in an end-loaded piston-cylinder apparatus using ½'' Talc/Pyrex assemblies with a tapered graphite heater. A friction correction of 18% was applied to the nominal pressure, according to a calibration by the quartz-coesite transition at 790 °C (Bose & Ganguly, 1995). Temperature was measured by S-type thermocouple (Pt-$Pt_{90}Rh_{10}$) below 1300 °C and with a D-type ($W_{97}Re_3$ - $W_{75}Re_{25}$) above. To ensure that the secondary alteration and recrystallization of the inclusions is minimal, run durations varied between 24 and 5 hours (for exact run durations see Table 3.1). At the end of the run, 25-30% of the pressure was released over the period of 10-30 minutes, followed by several hours of continuous decompression to ambient conditions. Simultaneously with initial pressure release, the runs were quenched at ~100 °C/minute. As known from previous research performed at similar conditions, this approach allows to preserve inclusions and minimize the opportunity for any secondary changes (Bali et al., 2013; Tingle et al., 1992). For pressures ≥ 3 GPa the decompression P-T paths were slightly adjusted to avoid ice formation, with an addition of low temperature heating step (~50-75 °C, max time – 2 h) during the final pressure release.

Table 3.1. *List of experiments performed to determine the position of H_2-H_2O critical curve. Experiments performed without the double capsule technique were not used for critical curve position establishment, except for cases specifically mentioned in the text.*

Experiment	Pressure, GPa	Temperature, °C	Run duration, h	Crystal	Double capsule	Run products description
KVH01	3	900	24	Olivine (Dac Lac, Vietnam)	-	H_2, H_2O, H_2+H_2O
KVH02	3	1000	24	Olivine (Dac Lac, Vietnam)	-	H_2, H_2O, H_2+H_2O
KVH03	3	1100	24	Olivine (Dac Lac, Vietnam)	-	H_2, H_2O, H_2+H_2O
KVH04	3	1200	24	Olivine (Dac Lac, Vietnam)	-	H_2+H_2O+Fe+FeO+Brc
KVH05	3	1250	24	Olivine (Dac Lac, Vietnam)	-	H_2+H_2O+Fe+FeO+Brc
KVH06	3	1300	24	Olivine (Dac Lac, Vietnam)	-	H_2+H_2O+Fe+FeO+Brc
KVH07	3	1250	22	Olivine (Dac Lac, Vietnam)	-	H_2+H_2O+Fe+FeO+Brc
KVH08	3.5	1100	22	Olivine (Dac Lac, Vietnam)	-	H_2, H_2O, H_2+H_2O
KVH09	3.5	1200	22	Olivine (Dac Lac, Vietnam)	-	H_2+H_2O+Fe+FeO+Brc
KVH10	3.5	1300	23	Olivine (Dac Lac, Vietnam)	-	H_2+H_2O+Fe+FeO+Brc
KVH11	4	1200	20	Olivine (Dac Lac, Vietnam)	-	H_2+H_2O+Fe+FeO+Brc
KVH13	3.5	1300	20	Olivine (Dac Lac, Vietnam)	-	H_2+H_2O+Fe+FeO+Brc
KVH14	4	1400	20	Olivine (Dac Lac, Vietnam)	-	Fe+FeO
KVH15	3	1200	24	Olivine (Dac Lac, Vietnam)	-	H_2+H_2O+Fe+FeO+Brc
KVH16	3	1175	24	Olivine (Dac Lac, Vietnam)	-	H_2+H_2O+Fe+FeO
KVH18	3	1225	24	Olivine (Dac Lac, Vietnam)	-	H_2+H_2O+Fe+FeO+Brc
KVH19	3.5	1200	21	Synthetic forsterite	+	H_2, H_2O, H_2+H_2O
KVH20	3.5	1250	21	Synthetic forsterite	+	H_2, H_2O, H_2+H_2O
KVH21	3.5	1350	21	Synthetic forsterite	+	H_2, H_2O, H_2+H_2O, Brc
KVH22	4	1300	21	Synthetic forsterite	+	H_2, H_2O, H_2+H_2O
KVH30	3	1150	20	Synthetic forsterite	+	H_2, H_2O, H_2+H_2O
KVH32	2.5	1100	22	Synthetic forsterite	+	H_2+H_2O
KVH33	2.5	1000	22	Synthetic forsterite	+	H_2, H_2O, H_2+H_2O
KVH35	2.5	950	24	Synthetic forsterite	+	H_2, H_2O, H_2+H_2O
KVH36	2.5	1050	24	Synthetic forsterite	+	H_2+H_2O
KVH37	2.5	1050	21	Synthetic forsterite	+	H_2+H_2O
KVH38	2.5	950	24	Synthetic forsterite	+	H_2, H_2O, H_2+H_2O
KVH39	2.5	1050	24	Synthetic forsterite	+	H_2+H_2O
KVH41	2.5	1150	21	Synthetic forsterite	+	H_2+H_2O
KVH42	2.5	900	24	Synthetic forsterite	+	H_2, H_2O, H_2+H_2O

Experiment	Pressure, GPa	Temperature, °C	Run duration, h	Crystal	Double capsule	Run products description
KVH43	2	900	24	Quartz (Brazil)	+	H_2+H_2O
KVH44	2	800	24	Quartz (Brazil)	+	H_2, H_2O, H_2+H_2O
KVH45	2	950	24	Quartz (Brazil)	+	H_2+H_2O
KVH46	2	850	24	Quartz (Brazil)	+	H_2, H_2O, H_2+H_2O
KVH47	2	850	24	Quartz (Brazil)	+	H_2, H_2O, H_2+H_2O
KVH48	2	850	19	Quartz (Brazil)	+	H_2, H_2O, H_2+H_2O
KVH49	2	900	18	Quartz (Brazil)	+	H_2+H_2O
KVH50	2.5	1050	21	Synthetic forsterite	+	H_2+H_2O
KVH51	2.5	1100	19	Synthetic forsterite	+	H_2+H_2O
KVH52	2.5	1150	19	Synthetic forsterite	+	H_2+H_2O
KVH53	3.5	900	12	Synthetic forsterite	+	H_2, H_2O, H_2+H_2O
KVH54	3.5	1200	14	Synthetic forsterite	+	H_2, H_2O, H_2+H_2O
KVH55	3.5	1300	9	Synthetic forsterite	+	H_2, H_2O, H_2+H_2O
KVH56	4	1250	10	Synthetic forsterite	+	H_2, H_2O, H_2+H_2O, Brc
KVH57	3.5	1350	7	Synthetic forsterite	+	H_2, H_2O, H_2+H_2O, Brc
KVH60	3	1250	10	Synthetic forsterite	+	H_2+H_2O
KVH62	1.5	650	24	Quartz (Brazil)	+	H_2, H_2O, H_2+H_2O
KVH63	1.5	700	24	Quartz (Brazil)	+	H_2, H_2O, H_2+H_2O
KVH64	1.5	750	24	Quartz (Brazil)	+	H_2+H_2O
KVH65	1	750	24	Quartz (Brazil)	+	H_2+H_2O
KVH66	1	700	24	Quartz (Brazil)	+	H_2+H_2O
KVH67	1	650	24	Quartz (Brazil)	+	H_2+H_2O
KVH68	1	600	24	Quartz (Brazil)	+	H_2, H_2O, H_2+H_2O
KVH69	2	750	24	Quartz (Brazil)	+	H_2, H_2O, H_2+H_2O
KVH70	2.5	1000	19	Synthetic forsterite	+	H_2, H_2O, H_2+H_2O
KVH71	3	1200	10	Synthetic forsterite	+	H_2, H_2O, H_2+H_2O
KVH72	3.5	1300	5	Synthetic forsterite	+	H_2, H_2O, H_2+H_2O,Brc
KVH73	4	1300	5	Synthetic forsterite	+	H_2, H_2O, H_2+H_2O,Brc

3.2.3. Sample preparation and Raman investigation

Capsules were cut open after the runs, crystals retrieved, mounted in epoxy resin and doubly polished to the thickness of 100-200 μm. Initial run product investigation and inclusion mapping were undertaken with the use of Leica DMLP polarization microscope with objectives ranging from 5^x to 50^x. Photographs were taken with a Canon EOS D60 camera, mounted on the microscope. Raman spectra of coexisting fluid phases were collected with a Horiba Labram 800 HR UV confocal Raman spectrometer using the 514 nm line of an argon laser at 200 mW output power, a 1800 mm^{-1} grating and a confocal pinhole of 100 μm with a 50^x long distance objective.

3.2.4 LA-ICP-MS analyses

Prior to the LA-ICP-MS measurements, fluid inclusions were selected under the microscope, photographed and the presence of H_2 and H_2O phases confirmed with Raman spectroscopy. LA-ICP-MS analyses were performed with a 193 nm ArF Excimer laser ablation unit (GeolasPro system, Coherent, USA) connected to an Elan DRC-e quadrupole ICP-MS (Perkin Elmer, Canada). The sample chamber was flushed with He at 0.4 l/min, to which 5 ml/min of H_2 was added on the way to the ICP-MS machine. Inclusions and standards were ablated with a repetition rate of 10 Hz, with the energy for standards being 90 mJ and for the inclusions 180 mJ. Laser diameter varied based on the size of the inclusion from 8 to 25 μm. NIST SRM 610 glass was used as a standard for all analyzed elements, except for Xe – for which a separate standard was prepared. Analyzed isotopes were ^{131}Xe, ^{132}Xe, ^{85}Rb, ^{7}Li, ^{11}B, ^{27}Al, ^{90}Zr, ^{133}Cs.

As there are no commercially available EPMA or ICP-MS standards for xenon, a new standard was synthesized. A xenon-bearing glass was produced from a mixture of XeF_2 and powdered natural Armenian obsidian (S. Wu et al., *in print*) as starting materials. Xenon was added to ensure 1 wt% concentration (B. C. Schmidt & Keppler, 2002; Shibata et al., 1998). Those compounds were mixed, loaded into a Pt capsule, and heated for 1 hour at 1500 °C and 2 GPa in a piston-cylinder apparatus (½'' Talc/Pyrex assembly) and quenched. Optical examination showed no inhomogeneity.

3.3. Results

3.3.1. Position of the critical curve in the H_2-H_2O system

Fluid inclusions capturing experiments were performed for 30 individual pressure-temperature conditions to investigate the location of critical curve in the H_2-H_2O system from 1 to 4 GPa (Fig. 3.2, Table 3.1). Three types of inclusions can be observed in the samples: Darker, nearly pure H_2 inclusions with strong optical contrast to the host crystal and lighter H_2O-rich inclusions with weak optical contrast, as well as inclusions containing both phases at the same time.

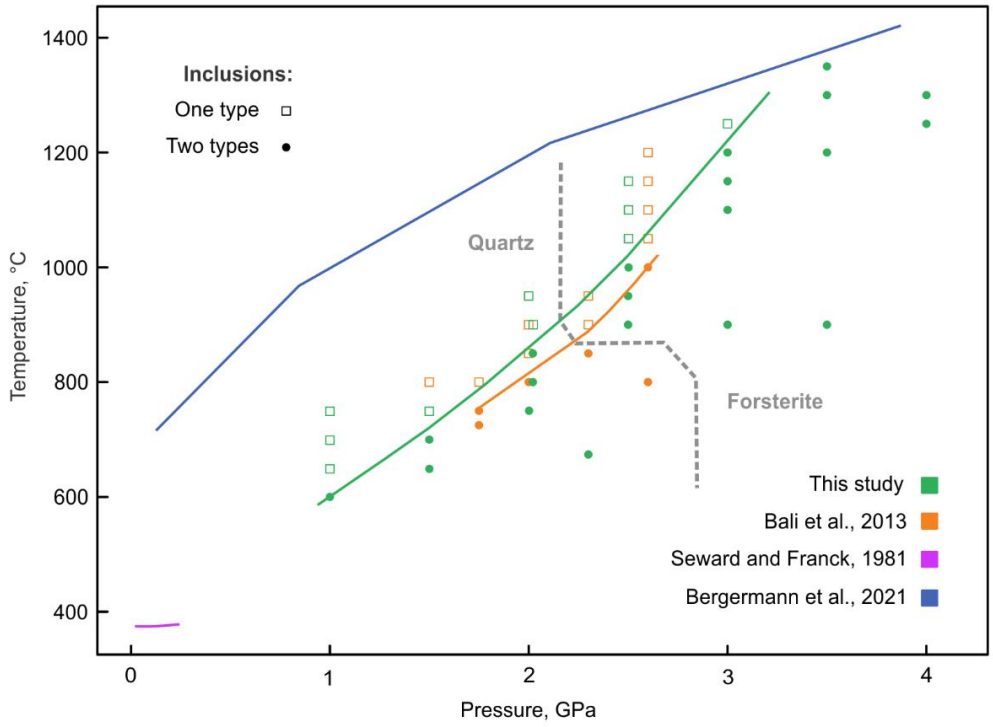

Figure 3.2. *Location of the critical curve in the H_2-H_2O system (green line) according to our experimental data (green symbols). Open squares – only mixed water-hydrogen inclusions are present (full miscibility), filled circles indicate the presence of pure water and pure hydrogen inclusions (immiscibility). The critical curve from Bali et al. (2013) is plotted as orange line with experimental data being symbols of the same color. The lavender line is a critical curve established by Seward and Franck (1981) and the blue line is a critical curve from a recent computational (Gibbs-ensemble Monte Carlo simulations) study by Bergermann et al. (2021). The thick, dashed dark grey line separates experiments performed with quartz or olivine both in this work and in (Bali et al., 2013).*

Depending on the phase assemblages present in the inclusions, two distinctively different groups of experimental run products can be identified. The first group, produced at lower temperatures, contains all three types of inclusions – with H_2, H_2O, and their mixture. Following Bali et al. (2013), we interpret this as entrapment within the region of H_2-H_2O immiscibility (Fig. 3.3a). The second group, synthesized at higher temperatures, contains only mixed H_2-H_2O inclusions which is interpreted as evidence for full miscibility between those two components at entrapment conditions (Fig. 3.3b).

Pure liquid water inclusions without any additional phases are observed only in samples synthesized at pressures above ~2.5 GPa. Below this value (e.g. Fig. 3.4a,c,e), the change in fluid density during cooling causes nucleation of a water vapour bubble. Often this vapour bubble contains trace amounts of hydrogen as the solubility of hydrogen in water increases as the critical curve is approached from within the immiscibility region. At pressures < 2 GPa, the temperature range with notable H_2 solubility appears to be larger (~100 degrees or even more) than at higher pressures, as indicated by detectable amounts of hydrogen in water inclusions (Fig. 3.3a). The water inclusion in Figure 3.3a was synthesized in quartz at 1.5 GPa and 700 °C, i.e., at conditions close to critical curve, but still in the immiscibility region. Two phases can be seen in the inclusion – liquid water with minor amounts of dissolved hydrogen (blue spectrum) and water vapour (orange spectrum), with a weak peak of gaseous hydrogen. No dissolved hydrogen was detected in inclusions containing a water phase at higher pressures than 2 GPa. Occasionally, metastable water inclusions synthetized in the immiscibility region at pressures < 2.5 GPa were observed to nucleate a gas phase, triggered by laser ablation of nearby inclusions or upon laser irradiation during Raman analysis. In general, the density of water along the investigated immiscibility curve from 1.5 to 3 GPa is relatively constant (Pitzer & Sterner, 1994); it ranges from 1.02 g/cm^3 at 1.5 GPa and 700 °C to 1.07 g/cm^3 at 3 GPa and 1200 °C (the highest temperatures at which immiscibility is observed at a given pressures).

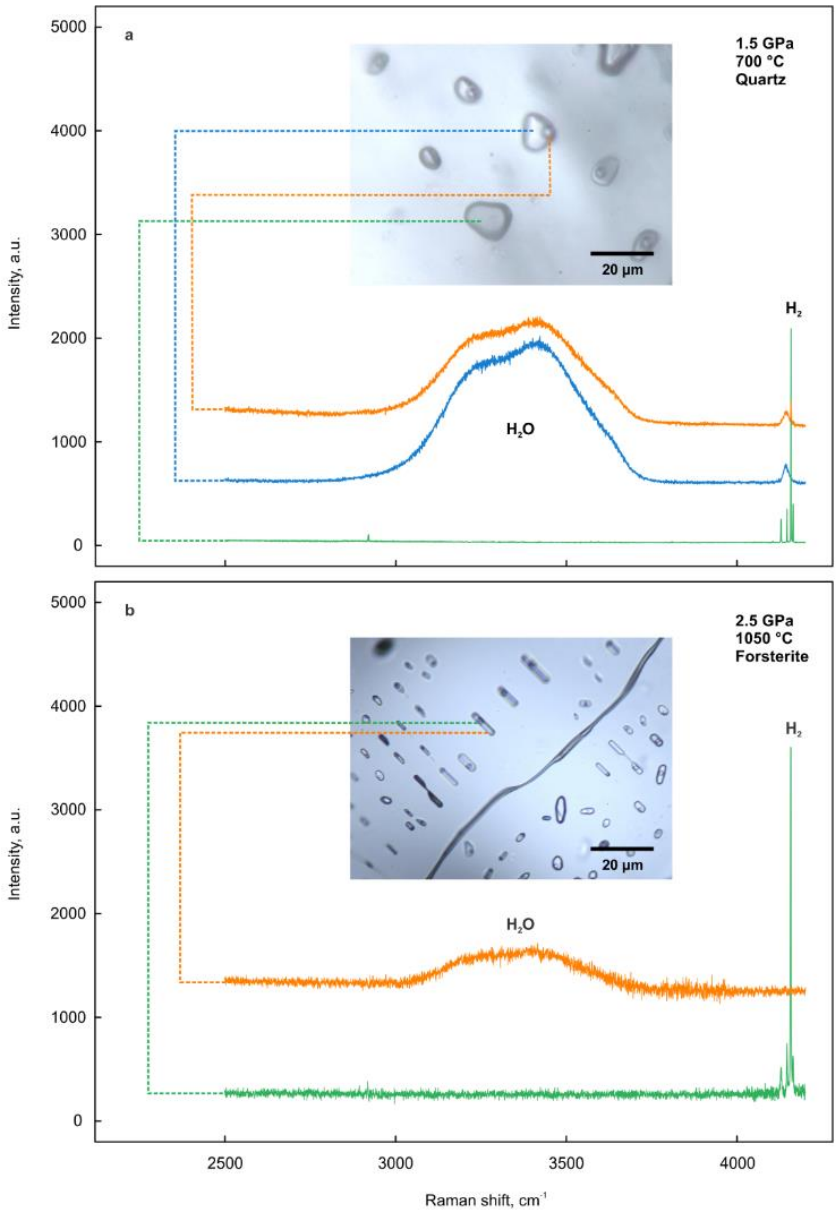

Figure 3.3. *Synthetic fluid inclusions formed in (a) quartz at 1.5 GPa and 700 °C, with Raman spectra of the vapor bubble in a water-rich inclusion in orange, liquid water in blue and hydrogen gas in green, and in (b) synthetic forsterite at 2.5 GPa and 1050 °C with Raman spectra of water in orange and hydrogen in green. The spectra in Figure (b) were baseline corrected, the image of inclusions in the same figure is a combination of two photographs made at different focal depths.*

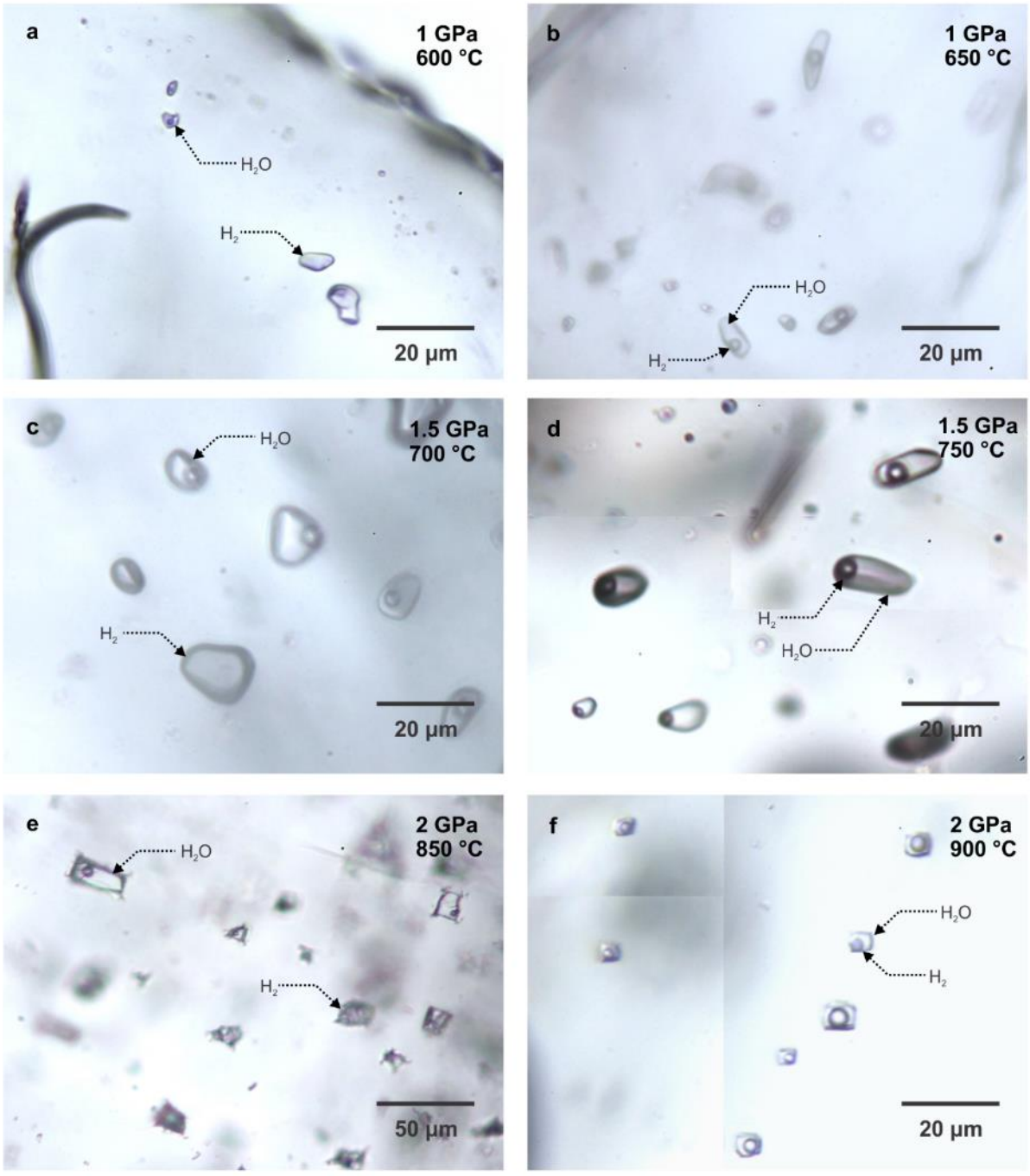

Figure 3.4. *Synthetic fluid inclusions formed at 1 - 2 GPa in the immiscibility region, below the H_2-H_2O critical curve (a, c, e) and above it in the miscibility area (b, d, f). Images (d) and (f) are combinations of several separate photographs taken at different focal depth.*

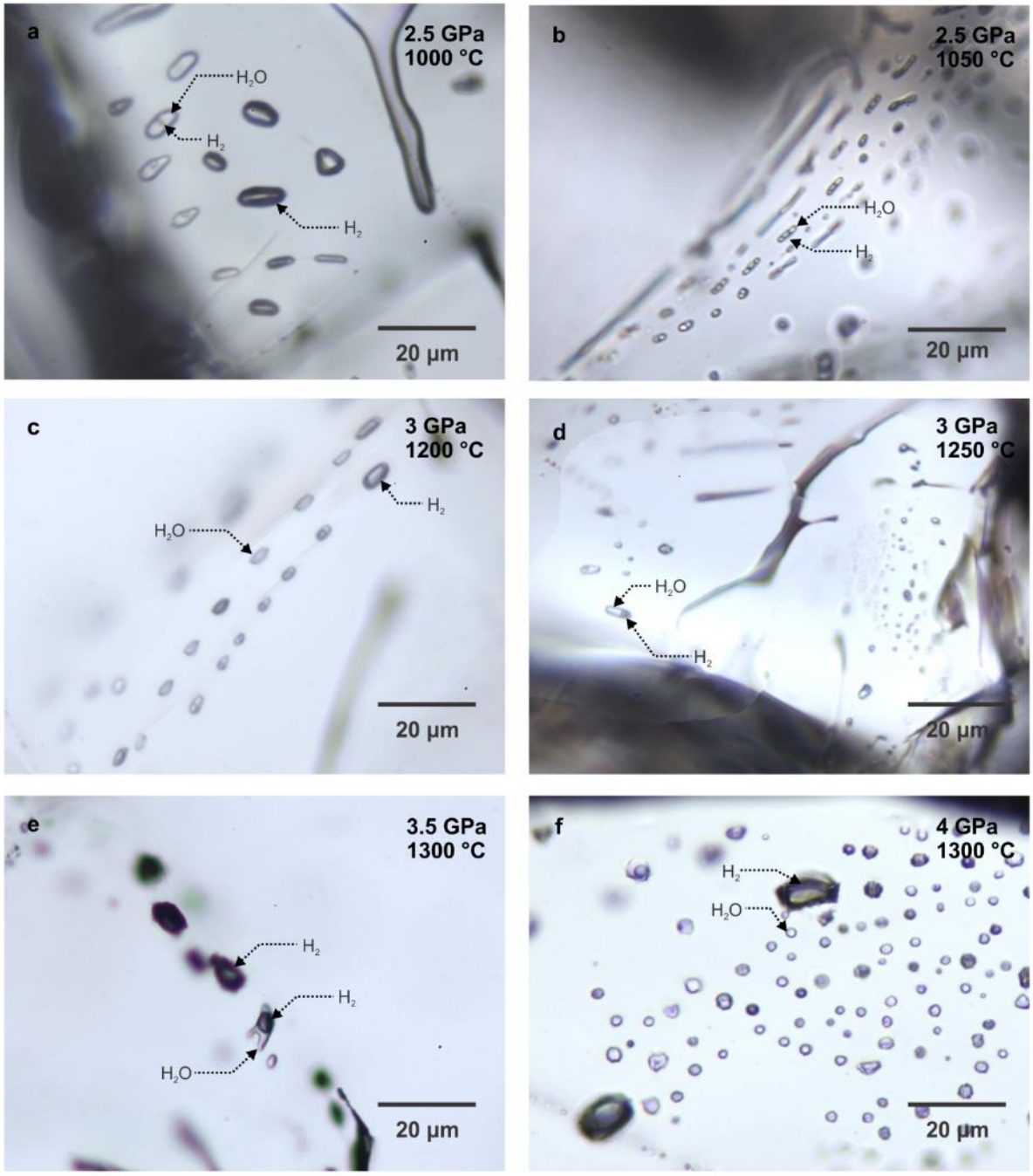

Figure 3.5. *Synthetic fluid inclusions formed at 2.5 - 4 GPa in the immiscibility region, below the H_2-H_2O critical curve (a, c, e, f) and above it in the miscibility region (b, d). Images (c), (d) and (f) are combinations of several separate photographs taken at different focal depths.*

Inclusions where H_2 is the dominant or only detectable phase are typically larger, compared to the size of mixed and pure water inclusions. According to Raman measurements, they appear to be

either completely free from H_2O or they contain only a thin coating of water along the walls of the inclusion. They also tend to be more resistant to recrystallization in our experiments, due to the extremely low solubility of major rock forming elements in non-polar hydrogen gas (Walther & Orville, 1983). Combined with their size, this makes H_2-rich inclusions easily detectable even at temperatures >1000 °C (e.g. Fig. 3.5c,e,f) and even in failed experiments, where water-containing inclusions show strong recrystallization features. Thus, a disappearance of distinctive hydrogen inclusions is a very reliable optical marker of full miscibility between H_2O and H_2. The disappearance of pure water inclusions is less noticeable, as they commonly exhibit vapour bubbles that may be confused with pure hydrogen without Raman analysis.

Fluids trapped in the inclusions contained some silica and magnesium, from the dissolution of quartz and forsterite. As water is diluted by non-polar hydrogen molecules, the solubility of silica decreases dramatically (Walther & Orville, 1983). In laser-heated diamond cell experiments, the formation of SiH_4 was observed as the result of H_2 and SiO_2 interaction (Shinozaki et al., 2014), however no detectable Raman signal SiH_4 was observed in our samples in the region of 2180 – 2300 cm^{-1}. This suggests that this species either was not present in our experiments or its concentration even in the low density pure hydrogen phase is negligible.

3.3.2. H_2-H_2O immiscibility in Fe-rich systems

The first batch of 16 experiments investigating the location of immiscibility curve in the H_2-H_2O system was performed without the inner platinum capsule, with crystals of natural inclusion-free forsterite submerged directly into FeO powder. In this particular experimental setup, we were able to produce fluid inclusions suitable for analysis only below 1175 °C at 3 and 3.5 GPa (Fig. 3.6f). Starting from 1175 °C, we observed an increasing number of Fe and FeO inclusions inside the sample (Fig. 3.6a-e).

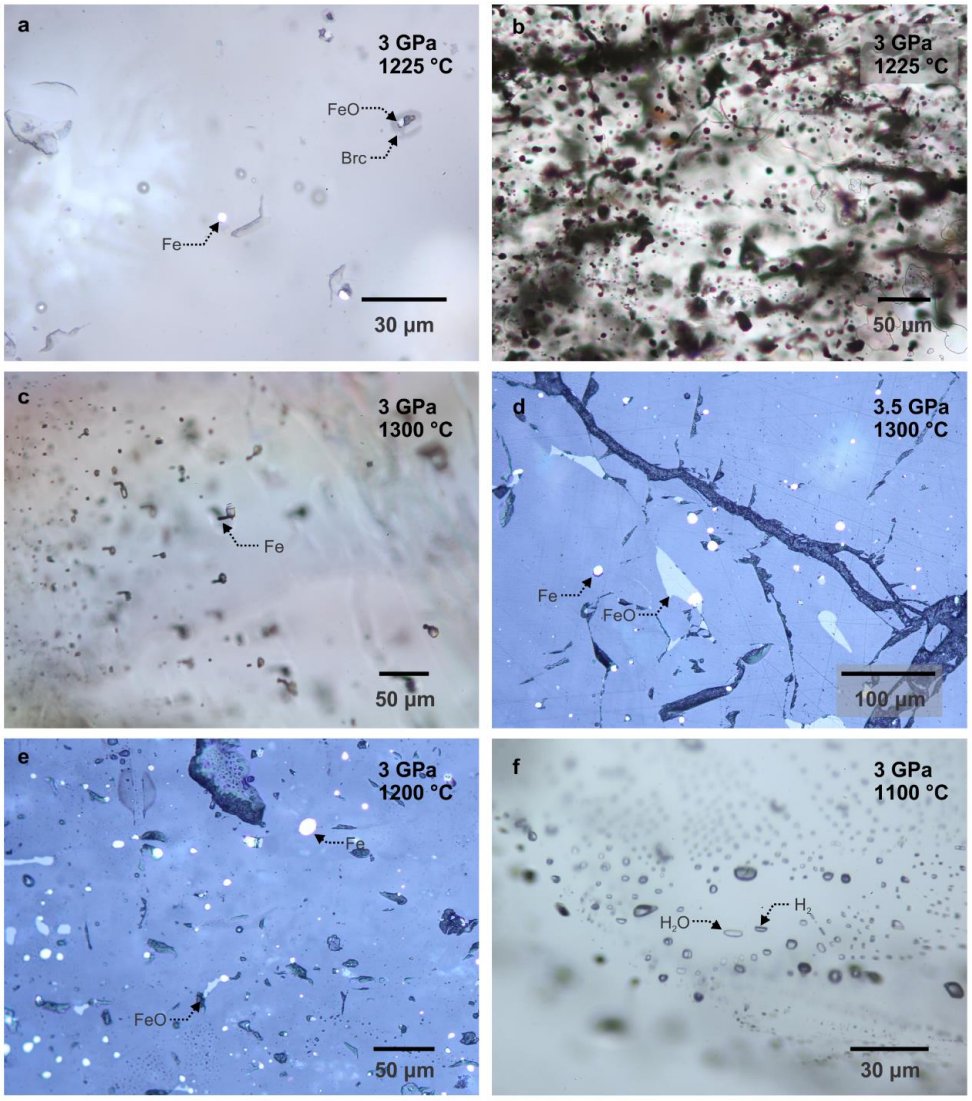

Figure 3.6. *Native iron and wüstite found alongside fluid inclusions in olivine samples. (a) – Iron melt inclusions near the surface of a sample, captured in olivine at 3 GPa and 1225 °C. A crystal of FeO alongside brucite in an exposed inclusion is visible as well (combination of reflected and transmitted light images); (b) – black spherical iron and irregular orange wüstite inclusions produced in olivine at 3 GPa and 1225 °C (transmitted light); (c) – inclusions with water, hydrogen and brucite showing signs of iron melt migration (transmitted light); (d) – iron inclusions produced at 3.5 GPa and 1300 °C and (e) – at 3 GPa and 1200 °C (reflected light). (f) – experiment without inner capsule that was carried out at 3 GPa and 1100 °C exhibiting well developed inclusions demonstrating evidence of H_2-H_2O immiscibility at those conditions. No Fe or FeO inclusions are visible (transmitted light).*

Almost all inclusions of iron exhibit a spherical or ellipsoid shape (Fig. 3.6a, b, d, e), some having crescent-shaped or irregular FeO rims. Those are extremely reminiscent of spheres of native Fe and Fe-Ni alloys found in ophiolites (e.g. Xu et al., 2015) where they are commonly attributed to iron melts (Liou et al., 2014). In one particular case at 3 GPa and 1300 °C (Fig. 3.6c, 24 h run duration) iron formed "tails" behind the inclusions, migrating in thermal gradient. Such a morphological feature is not at all uncommon in natural inclusions, but it requires the "tail" material to be a liquid or fluid, e.g. as in the classic case of CO_2 loss from migrating melt inclusions (Schiano et al., 2006).

At 3 GPa the melting point of pure iron is located ~450 °C above the lowest temperatures where we observed Fe inclusion formation (Saxena & Dubrovinsky, 2000). Thus interpreting them as remnants of metallic melt may appear counterintuitive. However the Fe-H alloy melting temperature is significantly lower (Yagi & Hishinuma, 1995). At 3 GPa in the Fe-H_2 system melting was observed at 800 °C (Fukai et al., 2003; Hiroi et al., 2005) – 375 °C colder compared to the temperature of our experiment. Based on morphological observations and experimental data we therefore attribute the appearance of spherical native iron inclusions to the formation of low-temperature hydrogen-rich metallic melt.

If no inner capsule is present, in addition to iron melt brucite formation is observed at temperatures exceeding 1200 °C at 3, 3.5 and 4 GPa (Fig. 3.6a, Fig 3.7b,d,e). It occurs in characteristic tabular elongated crystals across the inclusions, however no crystals have been found outside of the inclusions themselves. While this brucite is probably a result of post-entrapment inclusion alteration, it is likely that the process itself occurred at the temperatures and pressures of the experiments and $Mg(OH)_2$ did not form during cooling or decompression. Firstly – our cooling and decompression process is quite rapid, and secondly – in longer runs we observe partially recrystallized inclusions with brucite crystal-shaped holes in the middle, as it is replaced with forsterite.

In experiments where a double capsule was used, brucite emerged at slightly higher temperatures (compare Fig. 3.7a, b) of 1300 °C and above (Fig. 3.7c). But the crystals were significantly smaller, typically covering the walls of inclusions, and making them appear darker, optically similar to pure H_2 inclusions (Fig. 3.7c). In double capsule experiments, the observation of μm-sized brucite and iron inside the inclusions was a clear sign of inner capsule collapse (Fig. 3.7d), while the absence of hydrogen in inclusions indicating the failure of the outer capsule.

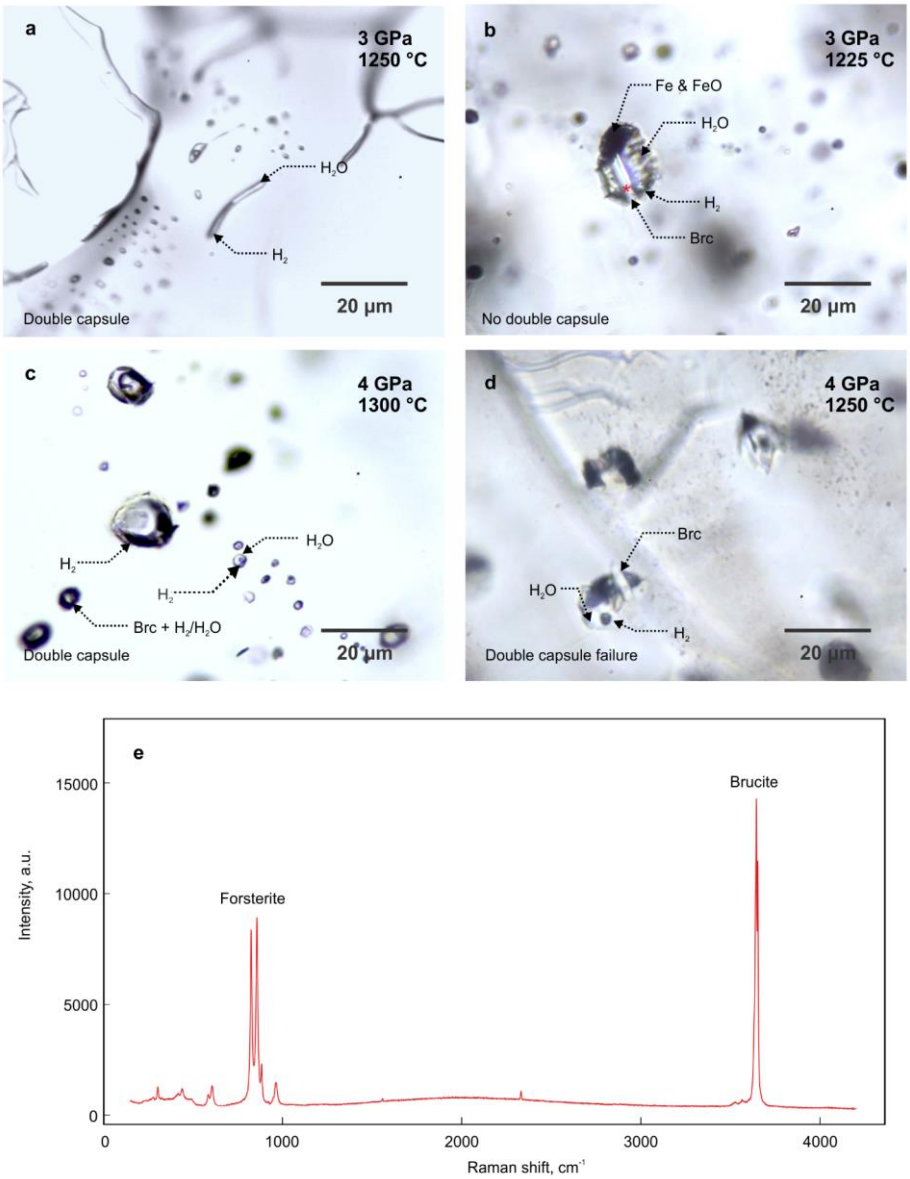

Figure 3.7. *(a) – experiment produced at 3 GPa and 1250 °C with the use of double capsule showing no signs of brucite; (b) – experiment produced at 3 GPa and 1225 °C without the inner capsule, red star shows the spot of Raman analysis from (e); (c) – minor inclusion formation on the walls of inclusions at 1300 °C and 4 GPa; (d) – large brucite crystals formed inside the inclusions as the result of double capsule failure at 4 GPa and 1250 °C; (e) – Raman spectrum of brucite inside the inclusion in forsterite.*

3.3.3. H_2-H_2O element partitioning experiments

Six experiments were performed (Table 3.2) in an attempt to investigate the partitioning of various elements between the coexisting H_2-rich and H_2O-rich fluid phases. Initially elements capable of producing gaseous hydrides at our experimental conditions such as C, P, As, Se, Te (Greenwood & Earnshaw, 2012) were the primary targets of our investigation, as well as Xe, Cs and Rb used as internal standards.

However, the majority of those experiments failed due to the reactivity of the selected chemical elements. Quantification of phosphorus in fluid inclusions in quartz (KVHP6) with the use of LA ICP-MS turned out to be impossible due to incorporation of this element into newly formed quartz, with the signal intensity from inclusion-free areas being comparable to the signal intensity from the inclusion itself. As, Se and Te (KVHP7, KVHP8) either were completely lost to the inner platinum capsule or they damaged the capsule during experiment due to the formation of platinum compounds. However, the experiments with carbon, xenon, rubidium, caesium and other elements present in the doped diopside glass (KVHP9, KVHP10, KVHP11) were successful.

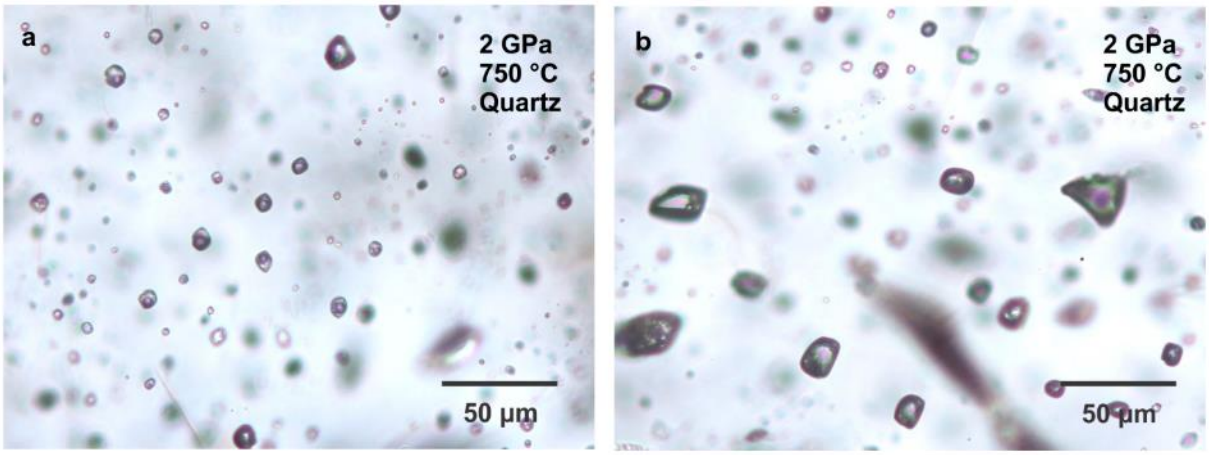

Figure 3.8. *Inclusions produced in experiment KVHP9 in quartz at 2 GPa and 750 °C. Though the immiscibility between H_2 and H_2O is visible – the element partitioning effects were too subtle to be detected.*

Experiments KVHP9 and KVHP10 were carried out at 2 GPa and 750 °C, less than 100 degree below the critical curve. Though the inclusions are relatively small, the immiscibility still can be easily observed. Samples from KVHP9 (Fig. 3.8) experiment were analysed with LA ICP-MS, but

the small size of the inclusions (~10-30 μm) did not allow to detect a clear fractionation effect between the water and hydrogen-rich phases.

Inclusions were also produced in the experiment KVHP11 at 2.3 GPa and 675 °C (Fig. 3.9), ~275 degrees below the critical curve. At those pressure and temperature, inclusions were trapped deep in the immiscibility region to highlight any possible element partitioning. They range in size from 10 μm to 100 μm with multiple water and hydrogen inclusions of comparable size, while inclusions with H_2 are typically larger (Fig. 3.9b).

Raman measurements of all types of inclusions and phases present in this sample yielded the first valuable result – hydrogen inclusions are very rich with CH_4 (Fig. 3.9c, orange), while this species is almost absent from water inclusions. Only a minor CH_4 signal can be seen in the vapour bubble of water-rich inclusions (Fig. 3.9c, green and blue). Initially, carbon was added to the capsule in the form of $CaCO_3$, as a minor impurity in the $Ca(OH)_2$ used. During the experiment in the Fe-FeO buffered capsule the presence of free hydrogen led to a rapid conversion of CO_3^{2-} to CH_4 - a dominant carbon species at such conditions (C. Zhang & Duan, 2009).

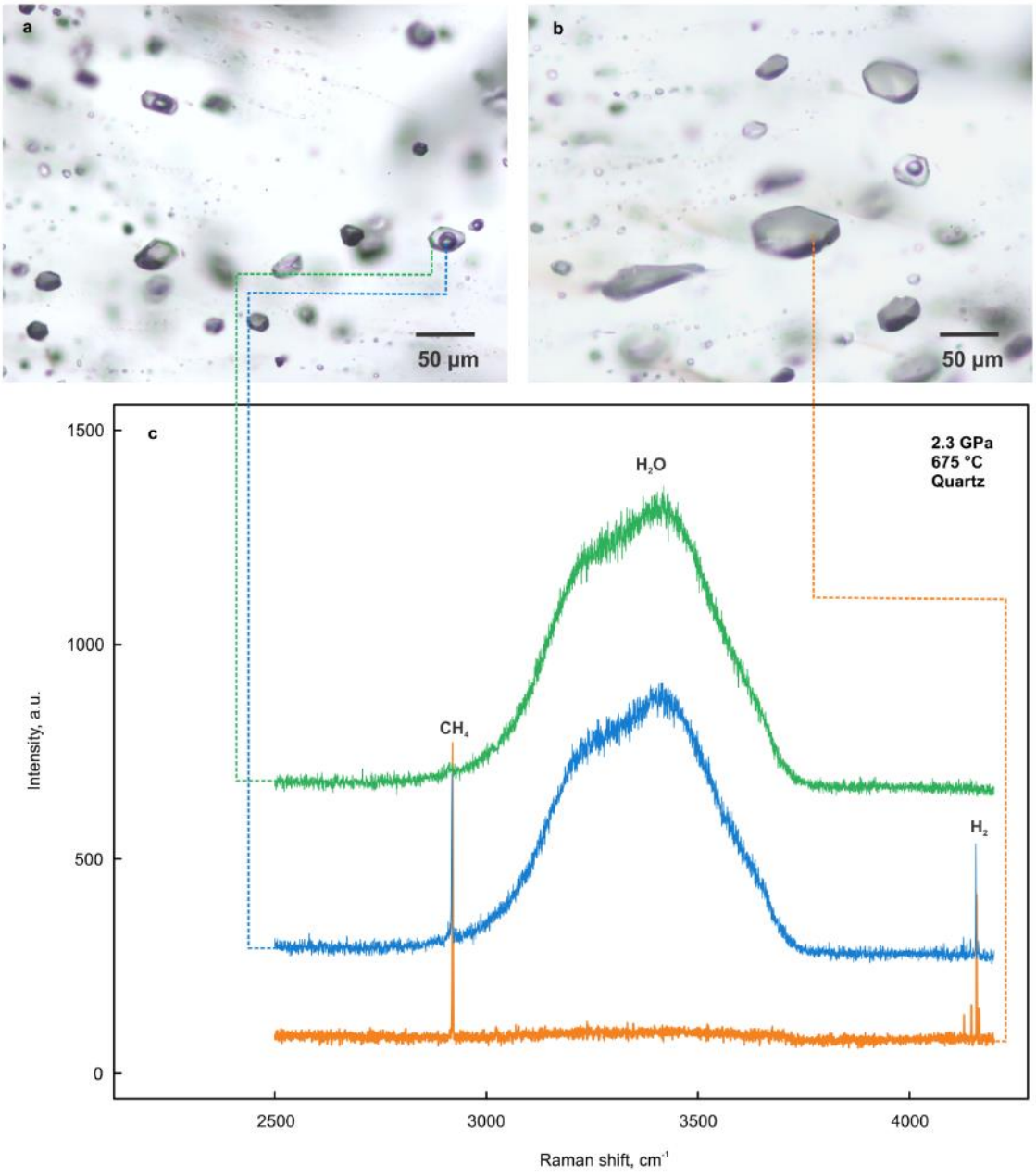

Figure 3.9. *Inclusions synthesized in quartz at 2.3 GPa and 675 °C in a partitioning experiment KVHP11 (a, b) with Raman spectra of the phases trapped in inclusions: liquid water (green), water vapor with hydrogen and methane (blue), mixture of methane and hydrogen (orange).*

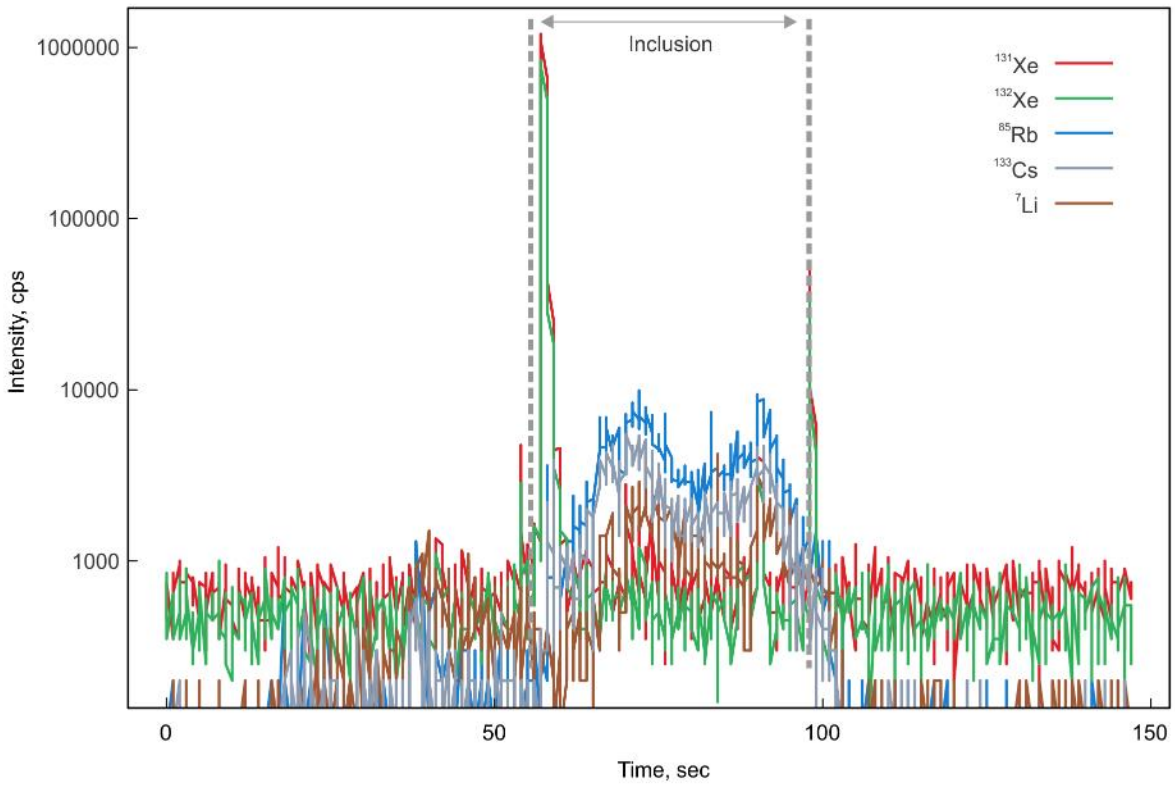

Figure 3.10. *Laser ablation analysis of an individual water-rich inclusion produced in the element partitioning experiment KVHP11.*

Further partitioning effects were unraveled with the use of LA ICP-MS with a typical inclusion laser ablation profile presented at Figure 3.10. During ablation the gas phase is released first, hence the strongest xenon peak at 65 seconds, followed by the remaining contents of the inclusion itself. Quite often during the ablation of larger inclusion, smaller neighboring inclusions were cracked, releasing the gas phase contents (see Xe peaks at 54 and 98 seconds, such data was not included in the integration). As the fraction of gas phase increases (Fig. 3.11a) the Xe/Rb and Xe/Cs ratios tend to increase, demonstrating strong partitioning of alkali metals into water phase. Xenon, on the other hand, tends to partition into the gas phase. Even though for similar sized inclusions, the maximum intensity of xenon signal is generally comparable (Fig. 3.11b), the difference in hydrogen and water density at experimental conditions implies strong partitioning of Xe into the H_2 phase. At 2.3 GPa and 675 °C, the densities of pure hydrogen and of pure water differ by a factor of about eight - 0.148 g/cm^3 (Leachman et al., 2009) and 1.138 g/cm^3 (Wagner & Pruß,

2002) respectively. Accordingly, if for water and hydrogen inclusions of similar size the intensity of xenon signal is about the same – the Xe_{H_2O}/Xe_{H_2} ratio in ppm by weight is 8-10.

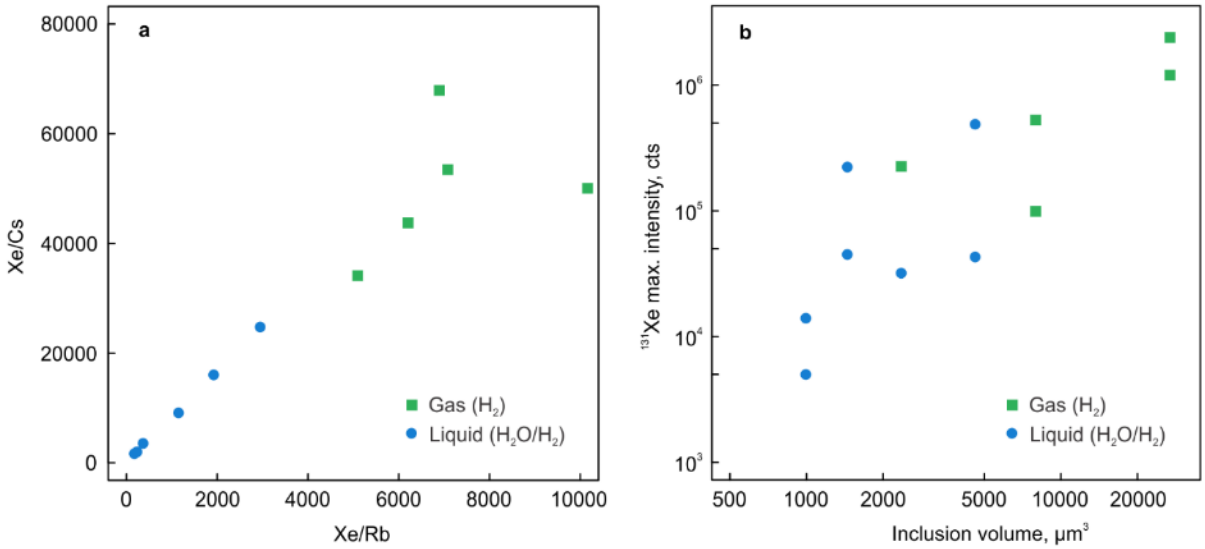

Figure 3.11. *LA ICP-MS established Xe/Cs count ratio plotted versus Xe/Rb count ratio for individual inclusions (a) and the intensity of ^{131}Xe signal plotted versus the inclusion volume (b). Data for hydrogen-rich inclusions is given in green, for inclusions with liquid water and possible co-trapped hydrogen in blue.*

Table 3.2. *Experiments investigating element partitioning associated with H_2-H_2O unmixing. In all experiments H_2, H_2O and H_2+H_2O inclusions were present.*

Experiment	Pressure, GPa	Temperature, °C	Run duration, h	Crystal	Double capsule	Starting materials
KVHP 6	2	750	22	Quartz (Brazil)	+	$Ca(OH)_2$+$CaCO_3$, XeF_2,SiO_2, H_2O+RbCl+CsCl, Au, H_3PO_4
KVHP 7	2	750	22	Quartz (Brazil)	+	$Ca(OH)_2$+$CaCO_3$, XeF_2,SiO_2, H_2O+RbCl+CsCl, Au, As
KVHP 8	2	750	22	Quartz (Brazil)	+	$Ca(OH)_2$+$CaCO_3$, XeF_2,SiO_2, H_2O+RbCl+CsCl, Au, Se, Te
KVHP 9	2	750	22	Quartz (Brazil)	+	$Ca(OH)_2$+$CaCO_3$, XeF_2,MORB glass, H_2O+RbCl+CsCl, Au
KVHP 10	2	750	22	Quartz (Brazil)	+	$Ca(OH)_2$+$CaCO_3$, XeF_2,MORB glass, H_2O+RbCl+CsCl, Au
KVHP 11	2.3	675	18.5	Quartz (Brazil)	+	$Ca(OH)_2$+$CaCO_3$, XeF_2,MORB glass, H_2O+RbCl+CsCl, Au

3.4. Discussion

3.4.1. Comparison with previous results

The experimental method used in the current study to establish the position of the H_2-H_2O critical curve is very similar to the one of Bali et al. (2013). The only significant difference is the reduced run times at temperatures above 850 °C (Table 3.1). As can be seen from Figure 3.2, the experimental data are extremely similar in the pressure range where the two studies overlap, with both critical curves having the same slope. The only significant deviation between two datasets that cannot be explained by thermocouple uncertainty or temperature gradients in the piston-cylinder assembly is a single experiment of Bali et al. at 2.3 GPa and 900 °C, showing immiscibility where our data suggests that fluids are still miscible. Yet in their work the critical curve was drawn not below this experimental point, but across it, which indicates that it may have been a border case located extremely close to the curve, where distinguishing between immiscibility or miscibility patterns is not straightforward.

Results of Seward and Franck (1981), who measured immiscibility in systems with variable H_2-H_2O fractions to 440 °C and 250 MPa, are located outside of our experimental range and just slightly below the extrapolation of our critical curve. Though the discrepancy between this extrapolation and Seward and Franck's data is minor, the explanation for it straightforward. Our 600 °C and 1 GPa experiment is probably located almost exactly on the critical curve itself, as the pure hydrogen inclusions in this run are small and comparatively rare. Thus, at 1 GPa the real slope may be a bit steeper than we assumed. The extrapolation would then almost perfectly align with the critical curve of Seward and Franck (1981).

A direct comparison of our experiments with the computational results of Bergermann et al. (2021), supporting the existence of immiscibility between water and hydrogen, or Soubiran and Militzer (2015), advocating for the lack of such an effect, is complicated. Due to the sensitivity of the simulations to the choice of the cutoff radius value and the imperfections of analytical two-body interaction potentials, the disagreement of existing computational studies with our experimental data is quite significant. The results of Bergermann et al. (2021) indicate that at temperatures above 1100 °C the experimental critical curve approaches the simulated curve and intersects it at ~ 1350 °C. With no miscibility observed in our experiments above 3 GPa the experimental data for 3.5 and 4 GPa is in seeming agreement with the simulated critical curve,

however the general difference in slopes of the two curves suggests that this agreement is partially coincidental.

3.4.2. H_2-H_2O immiscibility in Earth's interior and the formation of super-reduced mineral assemblages

Several mechanisms for the formation of super-reduced mineral associations were proposed in the past. A first hypothesis suggested their deep origin (e.g. R. Y. Zhang et al., 2016), stating that phases such as moissanite, native silicon, iron, nitrides and phosphides crystallized at depths exceeding 200 km, where oxygen fugacity is naturally low, although by far not low enough to stabilize SiC (D. J. Frost & McCammon, 2008). For example, the SiC grains coexisting with diamond, native Fe and FeO from the Luobusa ophiolites (Tibet) were assumed to have formed at pressures of 8.5-9 GPa (R. Y. Zhang et al., 2016), corresponding to a depth of ~300 km.

A second hypothesis, described in detail by Bali et al. (2013), proposes that oxygen fugacity at the level of the IW buffer and below does not necessarily require deep mantle conditions. They theorize that low fugacities can be achieved locally, via gradual water removal from immiscible H_2-H_2O fluids even at relatively shallow conditions in the upper mantle. At first, reducing fluids may form at 150-200 km depth (Fig. 3.11a,b) via slab dehydration (Kawamoto, 2018). As water and hydrogen fluids percolate through the mantle, water is being sequestered in hydrous melts (Ni, Keppler, Behrens, 2011; Shen & Keppler, 1995), incorporated into nominally anhydrous minerals (Fei & Katsura, 2020; Hirschmann et al., 2005; Mierdel et al., 2007) or hydrous phases (Smyth, 2018). As the fraction of H_2O in the fluid decreases, the oxygen fugacity decreases as well (Bali et al., 2013) making the formation of super reducing phases plausible.

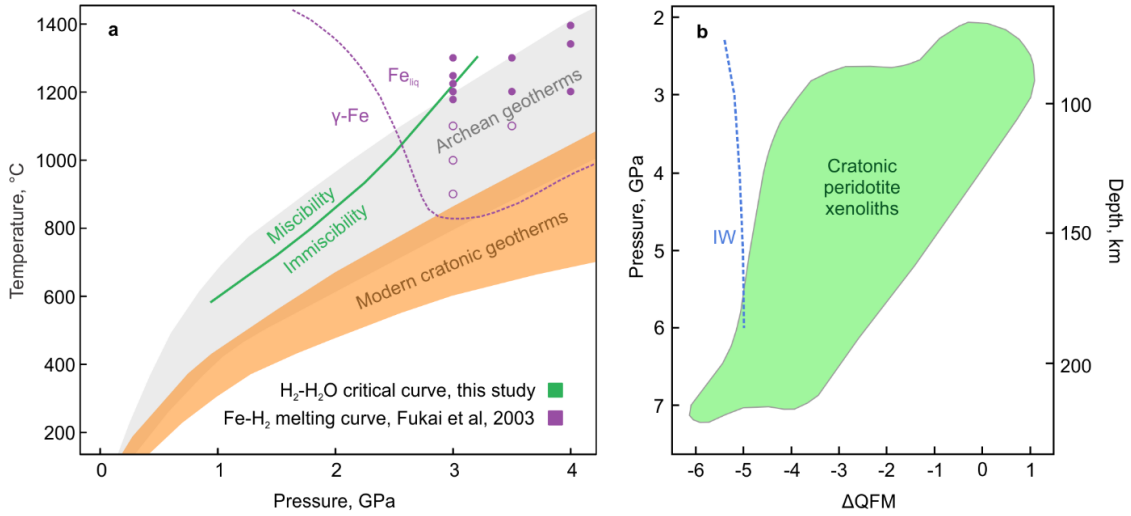

Figure 3.11. *(a) Archean (grey) (Mareschal, Jaupart. 2006) and modern (orange) geotherms (Hasterok & Chapman, 2011; Rudnick & Nyblade, 1999), compared with the H_2-H_2O immiscibility curve. The violet dashed line is a phase boundary between γ-Fe and Fe melt in a hydrogen-rich system (Fukai et al., 2003). Violet closed circles indicate the presence of iron melt in our experiments without double capsule, violet open circles indicate the absence of iron melt. (b) Fugacity range of cratonic peridotites based on xenolith data (Creighton et al., 2009; Goncharov, Ionov, Doucet, & Pokhilenko, 2012; Lazarov, Woodland, & Brey, 2009; McCammon & Kopylova, 2004; Woodland & Koch, 2003; Yaxley, Berry, Kamenetsky, Woodland, & Golovin, 2012). Dashed blue line - IW buffer conditions (Campbell et al., 2009) calculated along the hot Kalahari geotherm (Rudnick & Nyblade, 1999) shown on (a) as an upper bound of modern cratonic geotherms.*

As our experimental data suggests, low temperature iron melt can form in reducing environments of the upper mantle, as hydrogen causes significant depression of the Fe melting point to 800 °C at 3 GPa (Fukai et al., 2003; Hiroi et al., 2005). A similar melting point depression was observed at 3 GPa in the Fe-Ni-H system (Shibazaki et al., 2014). In our experiments at 3 GPa, which corresponds to ~100 km depth, iron melt inclusions emerged between 1100 and 1175 °C (Fig. 3.11a). For the melting to occur immiscibility is not a necessary condition (Fig. 3.11a), though at higher hydrogen fractions in the immiscibility field the temperature required for it is probably lower.

In addition to Fe and FeO, carbon compounds - graphite, diamond or hydrocarbons - are extremely important parts of the upper mantle reduced environments (D. J. Frost & McCammon, 2008). Though the in-detail investigation of carbon geochemistry in the presence of H_2-H_2O fluids at IW buffer conditions is beyond the scope of our study, we did observe significant methane generation from minor carbonate impurities (< 0.5 wt %) in the capsule. In general, if methane is available at upper mantle conditions diamond formation may occur during the evolution of such fluids in the lithospheric mantle (e.g. Matjuschkin et al., 2019; Thomassot et al., 2007). In addition, metastable low-pressure, low-temperature diamonds have been found to form in CH_4-rich fluid inclusions during the serpentinization of oceanic lithosphere (Pujol-Solà et al., 2020). However, it is currently unknown how widespread this process is. Observations from our element partitioning experiments suggest that in the of H_2-H_2O immiscibility field, methane is incorporated into the highly mobile H_2-rich fluid phase that in turn may be a precursor to diamonds, graphite or moissanite.

Native iron, nickel, iron silicide, platinum and other metals and alloys have been described in metal-enriched xenoliths from Avacha volcano that samples the mantle wedge below Kamchatka peninsula (Ishimaru et al., 2009; Kepezhinskas et al., 2022). Formation conditions for this suite of rocks and associated metals are estimated as 792-1100 °C and 1-3 GPa (Kepezhinskas et al., 2022 and references within). At 2-3 GPa, the H_2-H_2O immiscibility curve is situated between 800 and 1200 °C (Fig. 3.11a), and the phase assemblage present in xenoliths indicates fugacities at the level of the IW buffer. We suggest that in this particular case, the coexistence of water and hydrogen-rich immiscible fluids may be the cause of the observed proximity of super reduced areas and zones with the typical mantle wedge oxygen fugacity of ΔQFM ± 1 (Fig. 3.11a). As can be seen from the diagram (Fig. 3.11a) at 3 GPa, hydrated metallic melt formation is not implausible as well, if H_2 is the dominating fluid species.

In general, our experiments strongly suggest that super-reduced phases are not necessarily associated with UHP or UHT conditions and can form at ~100-150 km or even more shallow conditions in upper mantle with the participation of reducing H_2-CH_4 fluids.

3.4.3 H_2-H_2O unmixing as a possible cause for the early loss of Earth's noble gases

Isotopes of noble gases, especially of xenon and neon, have been traditionally used by to constrain Earth's early outgassing and atmosphere composition (e.g Allègre et al., 1987; Marty, 1989). The first atmospheres of Earth, Mars and Venus supposedly formed as the result of rapid gas release

from the planetary interior, or by equilibration with a magma ocean, occurring shortly after core formation (Lammer et al., 2018; Trieloff et al., 2000). A prominent feature of such planetary gas envelopes was their reducing nature with H_2 and CH_4 being the dominant gas species. During those times Earth's upper mantle, according to the model of Rubie at al. (2011), was hotter than Archaean estimates (Fig. 3.11a), extremely reduced and in equilibrium with the atmosphere. However, this state did not last for a long time: Cerium concentrations in oldest surviving zircons suggest rapid upper mantle oxidation (Smythe & Brenan, 2016; Trail et al., 2011), that was completed 200 Myr after planetary formation, though the atmosphere itself may have remained reducing for a loner time (e.g. Aulbach & Stagno, 2016).

Bali et al. (2013) suggested that rapid upper mantle oxidation was caused by the appearance of miscibility gap between water and hydrogen when the planet cooled down. As noted by Sharp et al. (2013), rapid hydrogen degassing allows to explain not only fugacity values, but also differences in water content and isotope compositions (H, Cl) in the Earth-Moon system. Hydrogen is easily transferred to the fluid phase during degassing of silicate melts (Hirschmann et al., 2012; Moore et al., 1998), thus the emergence of immiscibility between H_2 and H_2O triggers the formation of a buoyant and low viscosity H_2-dominant phase, followed by its rapid upward percolation (Bali et al., 2013; Sharp et al., 2013).

Such a scenario becomes plausible upon cooling of a planetary interior (Rubie et al., 2011), when geotherms crossed the immiscibility curve, intensifying hydrogen phase loss rate and driving the upper mantle fugacity to higher values. Noble gas isotope data supports this idea, suggesting increased outgassing flux during the first 20-30 Myr after the core formation (Kunz et al., 1998). One of the anomalies observed in the Earth's upper mantle noble gas compositions is the relative underabundance of ^{129}Xe, produced via the decay of ^{129}I ($t_{1/2} = 1.6 \times 10^7$ yr) that went extinct ~100 Myr after the formation of the solar system (Mukhopadhyay, 2012). Xenon is the least soluble in silicate melts of all noble gases (B. C. Schmidt & Keppler, 2002; Shibata et al., 1998) and thus one would expect it to preferentially partition into a fluid phase. As can be seen from our partitioning experiments, xenon enters preferentially the reduced H_2-rich phase. Thus, the early and rapid decrease in the quantities of radiogenic ^{129}Xe in the mantle can be explained by its partitioning into a hydrogen-rich phase during unmixing, subsequent degassing and then loss from the Earth's atmosphere for example by impact erosion during the late veneer (Kruijer et al., 2015; Walker, 2009).

Based on existing thermal evolution models (Herzberg et al., 2010; Korenaga, 2006; Rubie et al., 2011) and degassing constraints (Kunz et al., 1998; Mukhopadhyay, 2012) we estimate the H_2-H_2O unmixing to occur ~50-150 Myr after planetary formation, which is consistent with the evidences for oxidized upper mantle 4350 Myr before present (Smythe & Brenan, 2016; Trail et al., 2011). A wide number of the aforementioned studies suggest that proposed H_2 degassing is not exclusive to Earth, but was a feature of Lunar and Martian planetary evolution as well. This makes rapid and early hydrogen escape, catalyzed by the emergence of H_2-H_2O immiscibility, a possible common feature of the evolution of rocky planets, with the underabundance of radiogenic ^{129}Xe being a prominent marker of this process.

3.4.4. H_2-H_2O immiscibility in the exterior of Uranus and Neptune

H_2 and H_2O are known to be major constituents of Uranus and Neptune (Helled et al., 2020). Those two planets are commonly referred to as "ice giants", but the exact state of H_2O in these planets remains an enigma (Helled & Fortney, 2020), due to the scarcity of available data and the lack of dedicated interplanetary missions.

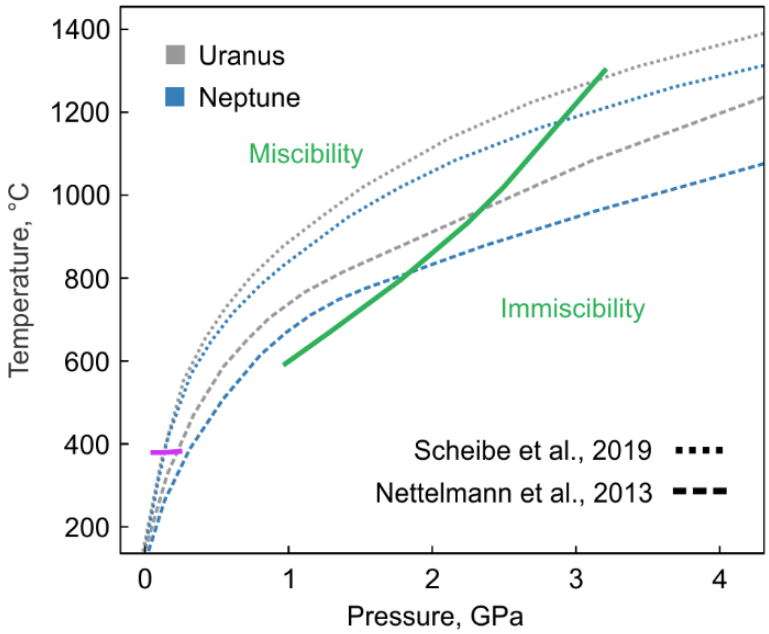

Figure 3.12. *Interior conditions of Uranus and Neptune (Nettelmann et al., 2013; Scheibe et al., 2019) compared with the experimentally observed H_2-H_2O critical curves from this study (green) and from (Seward & Franck, 1981) (purple).*

Multiple models of Neptune and Uranus interiors exist, including ones in which temperature-pressure profiles predict the possible existence of deep water oceans (Nettelmann, Helled, Fortney, & Redmer, 2013; Scheibe, Nettelmann, & Redmer, 2019).

If water is indeed a liquid in the outer shells of those planets, our data (Fig. 3.12) suggests the possible existence of the near-surface layer, where H_2O and H_2 are fully miscible. Such layer will strongly affect heat transfer and will require more complex interior models than perfectly adiabatic gradients (Podolak et al., 2019).

4. On the stability of acetate in subduction zone fluids

4.1. Introduction

Aqueous fluids released from the subducted slab are likely the main agent for melting and mass transport in subduction zones (e.g. Manning & Frezzotti, 2020; Rustioni, Audétat, & Keppler, 2021; Tatsumi, 1989). They also return subducted volatiles, such as water, carbon, and nitrogen back to the surface. Over long geologic time, this fluid flux therefore is involved in the processes regulating global sea level (e.g. Rüpke et al., 2004), the carbon dioxide content of the atmosphere (e.g. Plank & Manning, 2019), and climate. Traditionally, the fluids released by the dehydration of hydrous minerals, such as amphibole and serpentine, were considered to consist of simple solvent molecules, i.e. mostly H_2O and CO_2, plus some dissolved inorganic species (e.g. Manning, 2004). However, recently theoretical predictions have emerged which suggest that in high-pressure subduction fluids, most of the carbon may under some redox and pH conditions be present as organic molecules, such as acetate (Sverjensky et al., 2020; Sverjensky & Huang, 2015; Sverjensky, Stagno et al., 2014). In particular, acetate was predicted to be the predominant carbon species in aqueous fluids at 5 GPa, 600 °C and intermediate redox conditions (log $f(O_2)$ = 10^{-16} to 10^{-19}, not far from the Co-CoO buffer, O'Neill & Pownceby, 1993).

Evidence for the stability of acetate and similar organic species either from observations in natural samples or from high-pressure experiments is up to now rather limited. Frezzotti (2019) studied fluid inclusions in diamond-bearing rocks from the Alps by Raman spectroscopy. She concluded that the data provide evidence that diamond surfaces are coated by sp^2-, and sp^3-bonded amorphous carbon containing functional groups of carboxylic acids. This conclusion is, however, based on the deconvolution of rather broad Raman bands into various components and on band assignments that may not be unique. F. Huang et al. (2017) heated sodium acetate solutions in an externally heated diamond cell to 300 °C and 2.4–3.5 GPa and observed the partial decomposition of acetate to immiscible isobutane. However, they did not reach the predicted *P*,*T* stability field of acetate and it remains unclear whether the isobutane observed in these experiments is a stable species or just some intermediate, metastable decomposition product of the acetate. Y. Li (2017) studied the speciation in aqueous C-H-O fluids using synthetic fluid inclusions. He observed traces of ethane and perhaps higher hydrocarbons together with methane at 2.5 GPa, 600 °C, and Fe-FeO buffer conditions, but no

indication of acetate or other organic acid anions. We therefore carried out some exploratory experiments to test the predicted stability of acetate at 5 GPa and 600 °C.

4.2. Experimental methods

4.2.1. Overview of the experimental strategy

All experiments were carried out with a solution of 10 wt% of sodium acetate ($CH_3COONa \cdot 3\ H_2O$) in water. We made no attempt to externally buffer oxygen fugacity or pH. Rather, we assumed that if acetate were stable, it should at high concentrations buffer these parameters to its intrinsic stability range. We carried out two types of experiments:

(1) Piston cylinder experiments using very thick-walled silver capsules. Silver is poorly permeable for hydrogen at 600 °C (Chou, 1986), such that hydrogen loss from the capsule should be minimal and the intrinsic oxygen fugacity of the solution should be preserved during the experiments. Runs were designed to form a times series, from a nominally "zero-time experiment" (quenching 8 minutes after heating to 600 °C at 5 GPa) to 24 hours run duration. For mechanical stabilization, capsules were filled with silica powder in addition to the acetate solution. Run products were investigated by Raman spectroscopy and by powder X-ray diffraction.

(2) In-situ experiments using externally-heated diamond anvil cells. Here, the solution was directly observed under a microscope and studied by Raman spectroscopy during different heating and cooling paths. In one of these experiments, we reached 4.65 GPa and 600 °C, essentially the predicted stability field of acetate.

4.2.2. Piston-cylinder experiments

Piston cylinder experiments (Boyd & England, 1960) were carried out using mechanically sealed silver capsules with a length of 10 mm, an outer diameter of 5 mm and a wall thickness of 1 mm. A solution of 10 wt% $CH_3COONa \cdot 3\ H_2O$ (Merck, 99.5 %) in distilled water was loaded into the capsules together with SiO_2 powder (Chempur, 99.9%) for mechanical stabilization. The fluid/solid ratio ranged from 0.34 to 0.9. Experiments were carried out with low-friction ½'' NaCl-MgO assemblies containing a stepped graphite heater in an automated, end-loaded piston cylinder press (Voggenreiter GmbH, Mainleus, Germany). This device contains two spindle presses that allow a precise control of the oil pressures on the master ram and the endload, such that continuous compression and decompression profiles can be run under computer-control. Experiments were

slowly pressurized and de-pressurized over 19 to 21 hours in order to limit bomb and piston failures at 5 GPa. Runs were heated to the target temperature of 600 °C within 30 minutes and cooled down at the end of the run again within about 30 minutes. However, the "zero time" experiment was heated more rapidly within ~10 min, maintained for ~8 min at 600 °C and cooled to room temperature in 9 minutes. Temperatures were measured by a type S (Pt-PtRh) thermocouple close to the sample and controlled by a Eurotherm controller. A constant friction correction of - 0.12 GPa was applied to the nominal pressures. This correction was calibrated by the quartz–coesite transition near 3 GPa and by the density of synthetic fluid inclusions at 800 °C and 0.5–1.0 GPa.

4.2.3. Diamond anvil cell experiments

In-situ spectroscopic experiments were carried out with a Bassett-type externally-heated diamond anvil cell (Bassett et al., 1993) using synthetic, low-fluorescence type IIa diamond anvils with 700 μm culet. The cell was heated using molybdenum wires around the tungsten carbide seats supporting the diamonds. Temperature was monitored using K-type thermocouples (NiCr-Ni) directly attached to the diamonds. Gaskets made of Re or Ir with an initial thickness of 250 μm and a 150-180 μm drillhole were used. The 10 wt% sodium acetate solution was loaded into the sample chamber together with a small zircon crystal (natural zircon from Sri Lanka) as a pressure sensor. The cell was flushed during experiments with a 98 % Ar - 2 % H_2 gas mixture to prevent oxidation of the molybdenum heaters and the diamonds. Pressures during runs were determined based on the Raman shift of the $_{v3}(SiO_4)$ band in zircon (~1008 cm^{-1}) following the calibration of C. Schmidt et al. (2013). The objectives of the Raman spectrometer were cooled with air at high temperatures.

4.2.4. Raman spectroscopy

Raman spectra were measured using a Horiba/Jobin Yvon LabRam HR UV confocal Raman spectrometer in backscatter geometry. The 514 nm line of an argon laser with 75 - 200 mW output power was used for excitation. Spectra were measured with a 50^x objective, a 1800 groves/mm grating and a Peltier-cooled CCD detector. The confocal pinhole was set to 100 - 1000 μm, the spectral resolution was about 3.5 cm^{-1}, and each spectrum was typically collected using two 35 s accumulations.

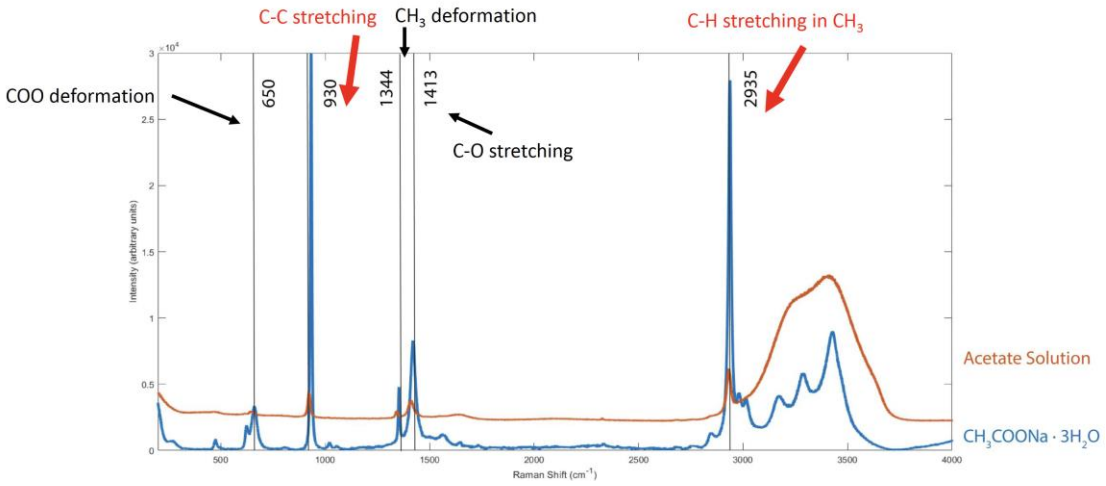

Figure 4.1. *Raman spectra of crystalline sodium acetate ($CH_3COONa \cdot 3\ H_2O$) and of a 10 wt% solution of sodium acetate in water, measured at ambient conditions.*

Since Raman spectroscopy was used as the main tool for identifying acetate and other organic species, Figure 4.1 shows the Raman spectra of both crystallized sodium acetate and of the 10 wt% sodium acetate solution used in our experiments. Band assignments are after Ito and Bernstein (1956). For identifying acetate in the experiments, we mostly relied on the strong C-C stretching band near 930 cm^{-1} and the C-H stretching vibration of the methyl group at 2935 cm^{-1}.

4.3. Results

4.3.1. Results from piston cylinder experiments

The piston cylinder experiments were all carried out at 5 GPa and 600 °C, with run durations of 0.1, 0.5, 2, 6, and 24 hours. In all runs, the SiO_2 powder had been converted to coesite, as indicated by X-ray diffraction. No other crystalline phases were detected. Raman spectra of the quenched run products (Fig. 4.2) failed to detect any acetate. Instead, bands similar to a highly-disordered graphite or perhaps kerogen-like material were observed. This is consistent with the gray discoloration observed in the run products (Fig. 4.2). There was no fundamental difference between the results of the "zero-time" experiment and the experiments with longer run durations up to 24 hours; only the bands of the carbonaceous material became more narrow with increasing run duration.

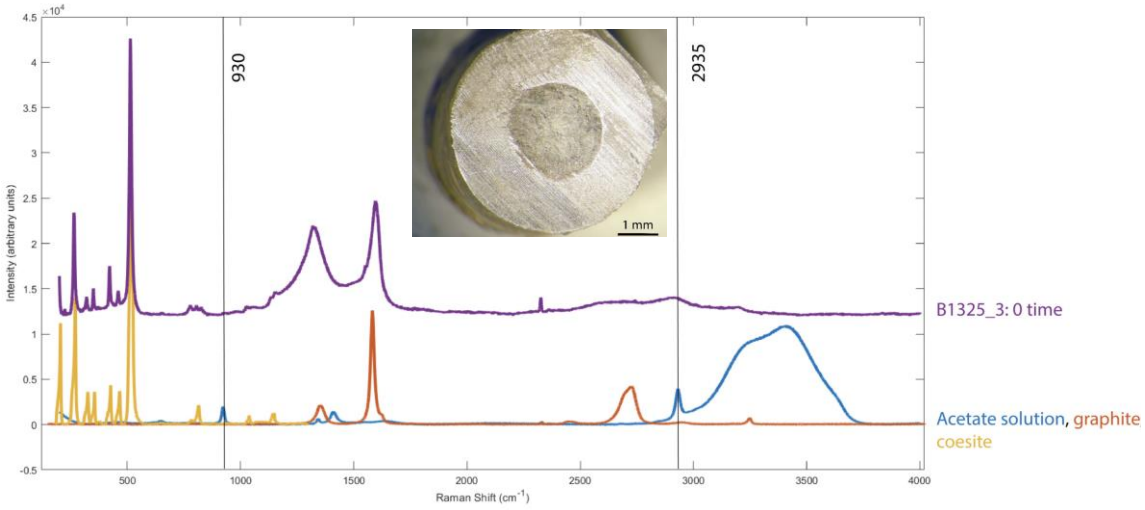

Figure 4.2. *Raman spectrum of run products from a "zero-time" piston cylinder experiment (purple) at 5 GPa and 600 °C. Reference spectra of the initial acetate solution (blue), of graphite (orange) and of coesite (yellow) are shown for comparison. Neither the 930 cm^{-1} nor the 2935 cm^{-1} band of acetate can be detected in the run products. The inset shows the opened silver capsule with the charge. The gray discoloration is due to some carbonaceous material formed by decomposition of acetate.*

4.3.2. Results from in-situ experiments in the diamond cell

A total of four experiments were carried out by heating the acetate solution in the diamond anvil cell. Detailed pressure-temperature paths for all experiments are given in the Figures 4.3 and 4.4. Run AB1 reached a maximum of 125 °C and 2.25 GPa before losing pressure.

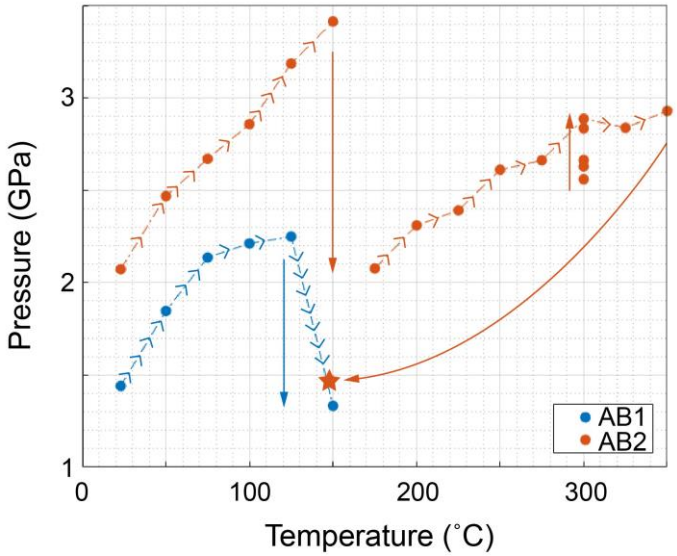

Figure 4.3. *Pressure-temperature paths of the diamond anvil cell runs AB1 and AB2. The star at 148 °C for run AB2 indicates the end of run when the gasket cracked. Straight arrows indicate pressure addition (by tightening the cell) or pressure drop (due to gasket flow or leakage).*

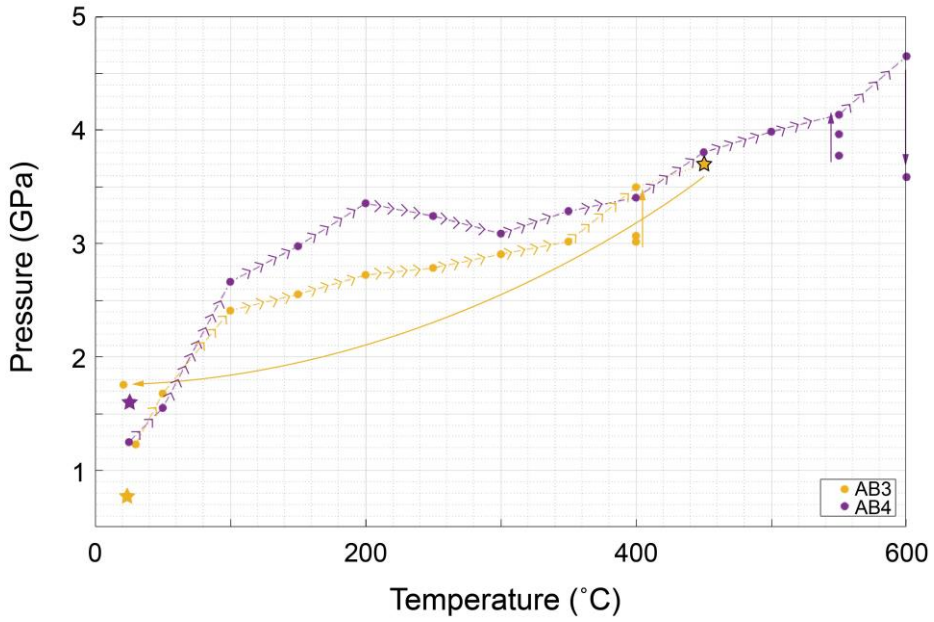

Figure 4.4. *Pressure-temperature paths of the diamond anvil cell runs AB3 and AB4. The black-outlined star for run AB3 at 450 °C marks a heater failure. The data point at 21 °C for run AB3 indicates the residual pressure immediately after the run. Stars indicates the pressures measured on the day after the runs.*

The Raman spectrum of acetate was observed up to the maximum temperature, the solution remained clear and no decomposition products of acetate were detectable. After cooling to room temperature, pressure was increased by tightening the cell such that the solution solidified to ice. Run AB2 was then conducted with this charge and reached 350 °C and 2.93 GPa before the gasket cracked. In this experiment, some dark precipitate started to form around 150 °C.

However, as shown in Figure 4.5a, even at the highest temperatures, the C-C stretching bands (930 cm^{-1}) and the C-H stretching bands (2935 cm^{-1}) of acetate were still detectable in the Raman spectrum of the solution, although shifted to slightly higher wavenumbers due to the elevated pressure. After cooling experiment AB2 to room temperature, bubbles of some immiscible liquid were observed inside the sample chamber. Raman spectra (Fig. 4.5b) suggest that they consist of newly formed hydrocarbons, in particular propane and isobutane, in very good agreement with similar observations made by F. Huang et al. (2017).

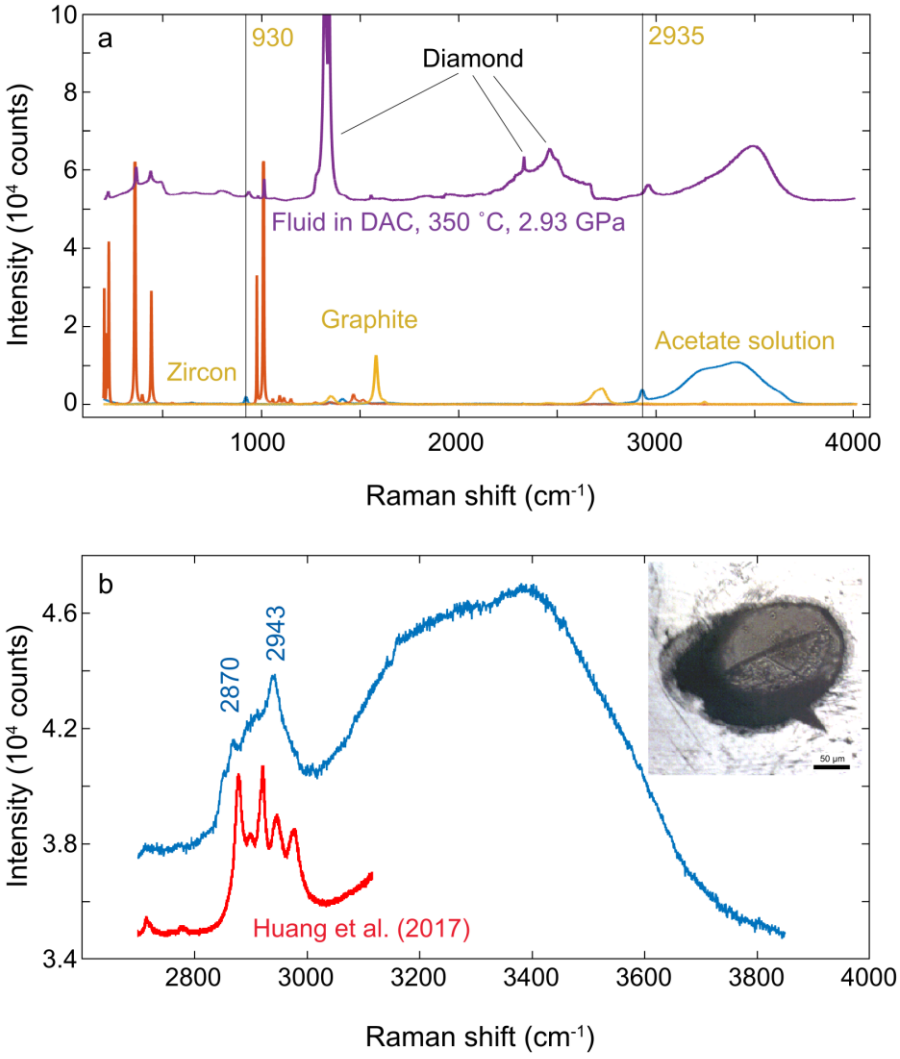

Figure 4.5. *(a) In-situ Raman spectrum of sodium acetate solution heated to 350 °C and 2.93 GPa inside an externally-heated diamond cell. Reference spectra of the acetate solution at ambient conditions, of graphite and of zircon (used as pressure sensor in the cell) are also shown. The 930 cm^{-1} and 2935 cm^{-1} bands of the acetate are still seen in the solution, shifted to slightly higher wavenumbers due to the elevated pressure. (b) Detail of the Raman spectrum of acetate solution after heating to 350 °C and 2.93 GPa and cooling to room temperature. New C-H stretching bands of hydrocarbons, likely isobutane and propane can be observed. The hydrocarbons form small droplets in the sample chamber, particularly in the area highlighted in yellow (inset).*

The formation of propane and isobutane suggest that already under these rather mild conditions, new C-C bonds may form rapidly, probably via some radical mechanism. In particular, the reaction of acetate to isobutane requires a complete re-arrangement of the C-C bonds.

Experiment AB3 reached maximum conditions of 400 °C and 3.50 GPa. After cooling to room temperature, some patches of dark material were visible in the solution and a small crystal of some (not further identified) alkali carbonate was detected by Raman spectroscopy, similar to observations made by F. Huang et al. (2017). Despite these results, which indicate partial decomposition, some acetate was still detectable in the solution. The charge from experiment AB3 was then re-run in experiment AB4, which reached 600 °C and 4.65 GPa, essentially the predicted stability field of acetate. However, already at 3.99 GPa and 500 °C, no acetate was detectable in the fluid anymore (Fig. 4.8). Instead, the Raman spectrum of some carbonaceous material resembling highly disordered graphite was detected. No acetate could be detected in the fluid after cooling it back to room temperature; instead, abundant dark, carbonaceous material was visible inside the cell (Fig. 4.6, 4.7), which yielded Raman spectra resembling highly disordered graphite.

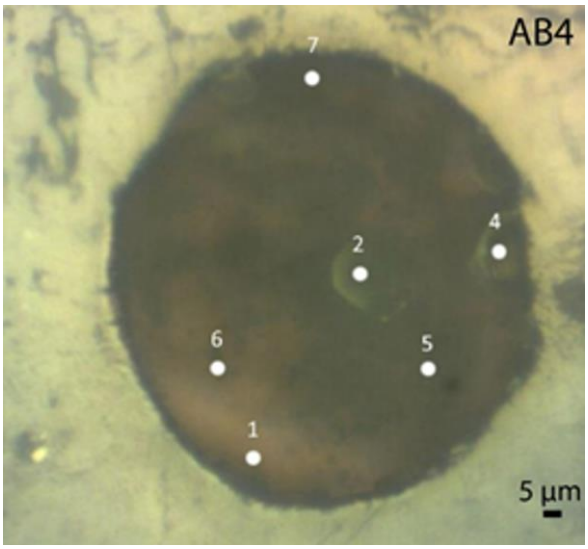

Figure 4.6. *Sample chamber of experiment AB4 after cooling back to room temperature from 600 °C and 4.65 GPa. Note the dark, carbonaceous material floating inside the solution. White spots refer to the location of Raman measurements given in Figure 4.7.*

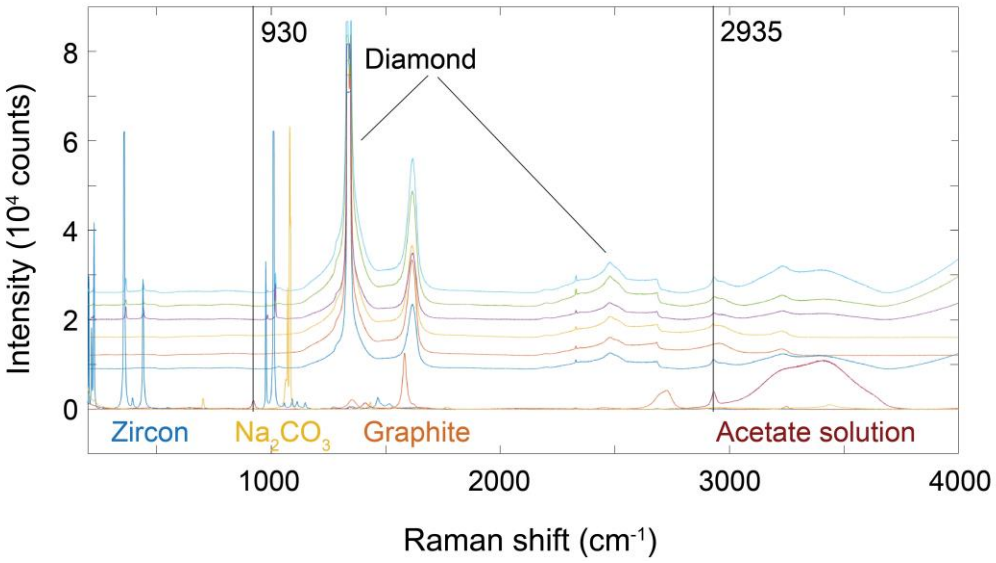

Figure 4.7. *Raman spectra of quench products from run AB4. The presence of a carbonaceous material resembling disordered graphite is obvious in all spectra. While there is a band in the C-H stretching region at ~2935 cm^{-1}, similar to acetate, the C-C stretching band of acetate at 930 cm^{-1} is clearly missing. The sequence of the spectra from bottom to top is from point 1 to point 7 according to Figure 4.6.*

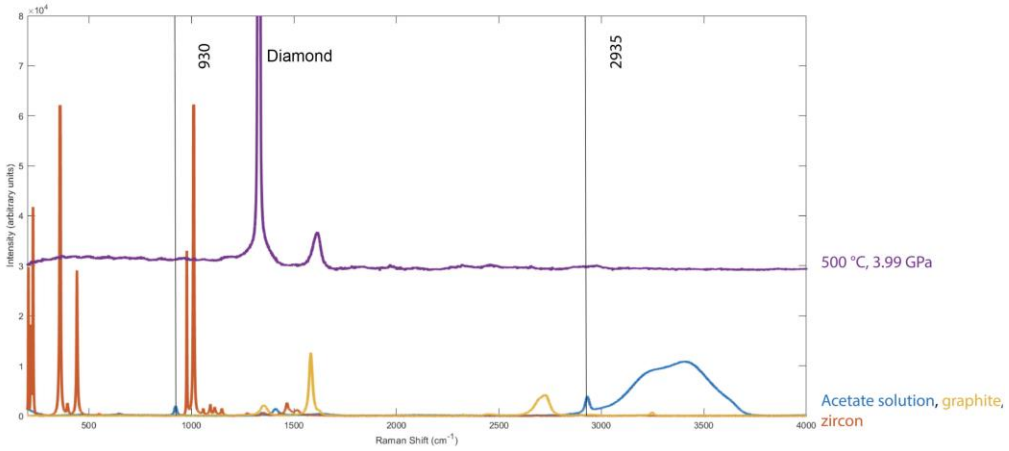

Figure 4.8. *In-situ Raman spectrum of sodium acetate solution heated to 500 ˚C and 3.99 GPa inside an externally-heated diamond cell. Reference spectra of the acetate solution at ambient conditions, of graphite and of zircon (used as pressure sensor in the cell) are also shown. The 930 cm^{-1} and 2935 cm^{-1} bands of the acetate are not detectable anymore, while some graphitic material has formed by decomposition of the acetate.*

4.4. Discussion

The results both from the piston cylinder and the in-situ diamond cell experiments appear very consistent and suggest that above 500 °C, acetate is not stable anymore in aqueous fluids and decomposes to some carbonaceous material. This observation has important consequences for the fate of subducted carbon. While carbon in oxidized form, i.e. as carbonates may be readily mobilized during the release of aqueous fluids, the fate of reduced carbon during subduction is much less understood (Plank & Manning, 2019). Reduced carbon in the form of former organic material is abundant in many sediments. If acetate, which is highly water-soluble were stable in aqueous fluids, such fluids would likely be very efficient in returning subducted carbon back to the surface. In the absence of such mobile organic species, graphitic material is likely almost insoluble in water and very poorly soluble in silicate melts (e.g. Eguchi & Dasgupta, 2017), at least in an intermediate range of oxygen fugacities, where neither the oxidation to CO or CO_2 nor the reduction to CH_4 is thermodynamically favorable. Such graphitic material may therefore be recycled deep into the mantle during subduction.

The discrepancy between our experimental results and theoretical predictions (Sverjensky, Stagno et al., 2014; Sverjensky et al., 2020) is likely due to uncertainties in some of the most basic properties of water at high pressure and high temperature. The stability of ionic species in aqueous fluids very strongly depends on the precise value of the dielectric constant. However, up to now, direct experimental measurements of the dielectric constant are limited to 550 °C and 0.5 GPa (Heger et al., 1980). Moreover, while the stability of acetate as a main carbon species in deep subduction fluids appears rather unlikely in the light of the experimental results presented here, the stability of minor concentrations of organic species is still possible and requires further investigation. For example, oxalate $(COO)_2^{2-}$, the most simple dicarbonic acid ion is known to form very strong complexes with many cations in aqueous solutions (e.g. Krishnamurty & Harris, 1961). Already minor concentrations of oxalate could therefore have a significant effect on the chemical transport properties of subduction zone fluids.

5. References

Abbott, D., Burgess, L., Longhi, J., & Smith, W. H. F. (1994). An empirical thermal history of the Earth's upper mantle. *Journal of Geophysical Research, 99*(B7), 13835–13850. https://doi.org/10.1029/94jb00112

Abramson, E. H., & Brown, J. M. (2004). Equation of state of water based on speeds of sound measured in the diamond-anvil cell. *Geochimica et Cosmochimica Acta*, *68*(8), 1827–1835. https://doi.org/10.1016/j.gca.2003.10.020

Alard, O., Griffin, W. L., Lorand, J. P., Jackson, S. E., & O'Reilly, S. Y. (2000). Non-chondritic distribution of the highly siderophile elements in mantle sulphides. *Nature*, *407*(6806), 891–894. https://doi.org/10.1038/35038049

Allègre, C. J., Staudacher, T., & Sarda, P. (1987). Rare gas systematics: formation of the atmosphere, evolution and structure of the Earth's mantle. *Earth and Planetary Science Letters*, *81*(2–3), 127–150. https://doi.org/10.1016/0012-821X(87)90151-8

Armstrong, K., Frost, D. J., McCammon, C. A., Rubie, D. C., & Ballaran, T. B. (2019). Deep magma ocean formation set the oxidation state of Earth's mantle. *Science*, *365*(6456), 903–906. https://doi.org/10.1126/science.aax8376

Audétat, A., & Keppler, H. (2004). Viscosity of fluids in subduction zones. *Science*, *303*(5657), 513–516. https://doi.org/10.1126/science.1092282

Aulbach, S., & Stagno, V. (2016). Evidence for a reducing Archean ambient mantle and its effects on the carbon cycle. *Geology*, *44*(9), 751–754. https://doi.org/10.1130/G38070.1

Bagdassarov, N., Golabek, G. J., Solferino, G., & Schmidt, M. W. (2009). Constraints on the Fe-S melt connectivity in mantle silicates from electrical impedance measurements. *Physics of the Earth and Planetary Interiors*, *177*(3–4), 139–146. https://doi.org/10.1016/j.pepi.2009.08.003

Bakker, H. J. (2008). Structural dynamics of aqueous salt solutions. *Chemical reviews*, *108*(4), 1456-1473. https://doi.org/10.1021/cr0206622

Bali, E., Audétat, A., & Keppler, H. (2013). Water and hydrogen are immiscible in Earth's mantle. *Nature*, *495*(7440), 220–222. https://doi.org/10.1038/nature11908

Ballhaus, C. (1993). Redox states of lithospheric and asthenospheric upper mantle. *Contributions to Mineralogy and Petrology*, *114*(3), 331–348. https://doi.org/10.1007/BF01046536

Barsoukov, E., & Macdonald, J. R. (2005). *Impedance Spectroscopy: Theory, Experiment, and Applications*. Hoboken, NJ: John Wiley & Sons, Inc. https://doi.org/10.1002/0471716243

Bassett, W. A., Shen, A. H., Bucknum, M., & Chou, I. M. (1993). A new diamond anvil cell for hydrothermal studies to 2.5 GPa and from -190 to 1200 °C. *Review of Scientific Instruments*, *64*(8), 2340–2345. https://doi.org/10.1063/1.1143931

Berendsen, H. J. C., Grigera, J. R., & Straatsma, T. P. (1987). The missing term in effective pair potentials. *Journal of Physical Chemistry*, *91*(24), 6269–6271. https://doi.org/10.1021/j100308a038

Bergermann, A., French, M., & Redmer, R. (2021). Gibbs-ensemble Monte Carlo simulation of H_2-H_2O mixtures. *Physical Chemistry Chemical Physics*, *23*(22), 12637–12643. https://doi.org/10.1039/d1cp00515d

Berndt, J., Liebske, C., Holtz, F., Freise, M., Nowak, M., Ziegenbein, D., … Koepke, J. (2002). A combined rapid-quench and H_2-membrane setup for internally heated pressure vessels: Description and application for water solubility in basaltic melts. *American Mineralogist*, *87*(11–12), 1717–1726. https://doi.org/10.2138/am-2002-11-1222

Bodinier, J. L., Vasseur, G., Vernieres, J., Dupuy, C., & Fabries, J. (1990). Mechanisms of mantle metasomatism: Geochemical evidence from the Lherz orogenic peridotite. *Journal of Petrology*, *31*(3), 597–628. https://doi.org/10.1093/petrology/31.3.597

Bose, K., & Ganguly, J. (1995). Quartz-coesite transition revisited: reversed experimental determination at 500-1200 °C and retrieved thermochemical properties. *American Mineralogist*, *80*(3–4), 231–238. https://doi.org/10.2138/am-1995-3-404

Boyd, F. R., & England, J. L. (1960). Apparatus for phase-equilibrium measurements at pressures up to 50 kilobars and temperatures up to 1750 °C. *Journal of Geophysical Research*, *65*(2), 741–748. https://doi.org/10.1029/jz065i002p00741

Bureau, H., & Keppler, H. (1999). Complete miscibility between silicate melts and hydrous fluids in the upper mantle: Experimental evidence and geochemical implications. *Earth and Planetary Science Letters*, *165*(2), 187–196. https://doi.org/10.1016/S0012-821X(98)00266-0

Burgess, R., Cartigny, P., Harrison, D., Hobson, E., & Harris, J. W. (2009). Volatile composition of microinclusions in diamonds from the Panda kimberlite, Canada: Implications for chemical and isotopic heterogeneity in the mantle. *Geochimica et Cosmochimica Acta*,

73(6), 1779–1794. https://doi.org/10.1016/j.gca.2008.12.025

Campbell, A. J., Danielson, L., Righter, K., Seagle, C. T., Wang, Y., & Prakapenka, V. B. (2009). High pressure effects on the iron-iron oxide and nickel-nickel oxide oxygen fugacity buffers. *Earth and Planetary Science Letters*, *286*(3–4), 556–564. https://doi.org/10.1016/j.epsl.2009.07.022

Chau, R., Mitchell, A. C., Minich, R. W., & Nellis, W. J. (2001). Electrical conductivity of water compressed dynamically to pressures of 70-180 GPa (0.7-1.8 Mbar). *Journal of Chemical Physics*, *114*(3), 1361–1365. https://doi.org/10.1063/1.1332079

Chou, I. M. (1986). Permeability of precious metals to hydrogen at 2 kb total pressure and elevated temperatures. *American Journal of Science*, *286*(8), 638–658. https://doi.org/10.2475/ajs.286.8.638

Corti, H. R. (2008). Electrical conductivity in hydrothermal binary and ternary systems. In V. M. Valyashko (Ed.), *Hydrothermal Properties of Materials*,(pp. 207-226). Hoboken, NJ: John Wiley & Sons, Inc. https://doi.org/10.1002/9780470094679.ch4

Creighton, S., Stachel, T., Matveev, S., Höfer, H., McCammon, C. A., & Luth, R. W. (2009). Oxidation of the Kaapvaal lithospheric mantle driven by metasomatism. *Contributions to Mineralogy and Petrology*, *157*(4), 491–504. https://doi.org/10.1007/s00410-008-0348-3

Dawson, J. B. (1980). *Kimberlites and their xenoliths*. Heidelberg: Springer Verlag-Berlin. https://doi.org/10.1007/978-3-642-67742-7

Demouchy, S., & Bolfan-Casanova, N. (2016). Distribution and transport of hydrogen in the lithospheric mantle: A review. *Lithos* , 240, 402-425. https://doi.org/10.1016/j.lithos.2015.11.012

Dobrzhinetskaya, L. F., Mukhin, P., Wang, Q., Wirth, R., O'Bannon, E., Zhao, W., … Sokhonchuk, T. (2018). Moissanite (SiC) with metal-silicide and silicon inclusions from tuff of Israel: Raman spectroscopy and electron microscope studies. *Lithos*, *310–311*, 355–368. https://doi.org/10.1016/j.lithos.2017.04.001

Dobrzhinetskaya, L. F., Wirth, R., & Green, H. W. (2005). Direct observation and analysis of a trapped COH fluid growth medium in metamorphic diamond. *Terra Nova*, *17*(5), 472–477. https://doi.org/10.1111/j.1365-3121.2005.00635.x

Ducea, M. N., & Park, S. K. (2000). Enhanced mantle conductivity from sulfide minerals, southern Sierra Nevada, California. *Geophysical Research Letters*, *27*(16), 2405–2408.

https://doi.org/10.1029/2000GL011565

Džidić, I., & Kebarle, P. (1970). Hydration of the alkali ions in the gas phase. Enthalpies and entropies of reactions $M^+(H_2O)_{n-1} + H_2O = M^+(H_2O)_n$. *Journal of Physical Chemistry*, *74*(7), 1466–1474. https://doi.org/10.1021/j100702a013

Eguchi, J., & Dasgupta, R. (2017). CO_2 content of andesitic melts at graphite-saturated upper mantle conditions with implications for redox state of oceanic basalt source regions and remobilization of reduced carbon from subducted eclogite. *Contributions to Mineralogy and Petrology*, *172*(2–3), 1–16. https://doi.org/10.1007/s00410-017-1330-8

Evans, R. L., Jones, A. G., Garcia, X., Muller, M. R., Hamilton, M. P., Evans, S., … Hutchins, D. (2011). Electrical lithosphere beneath the Kaapvaal craton, southern Africa. *Journal of Geophysical Research: Solid Earth*, *116*(4), 4105. https://doi.org/10.1029/2010JB007883

Evans, R. L., Wannamaker, P. E., McGary, R. S., & Elsenbeck, J. (2014). Electrical structure of the central Cascadia subduction zone: The EMSLAB Lincoln Line revisited. *Earth and Planetary Science Letters*, *402*(C), 265–274. https://doi.org/10.1016/j.epsl.2013.04.021

Fei, H., & Katsura, T. (2020). Pressure dependence of proton incorporation and water solubility in olivine. *Journal of Geophysical Research: Solid Earth*, *125*(2), e2019JB018813. https://doi.org/10.1029/2019JB018813

Fernández, D. P., Mulev, Y., Goodwin, A. R. H., & Sengers, J. M. H. L. (1995). A database for the static dielectric constant of water and steam. *Journal of Physical and Chemical Reference Data*, *24*(1), 33–70. https://doi.org/10.1063/1.555977

Filipponi, A., De Panfilis, S., Oliva, C., Ricci, M. A., D'Angelo, P., & Bowron, D. T. (2003). Ion hydration under pressure. *Physical Review Letters*, *91*(16), 165505. https://doi.org/10.1103/PhysRevLett.91.165505

Fowler, S. J., & Sherman, D. M. (2020). The nature of NaCl–H_2O deep fluids from ab initio molecular dynamics at 0.5–4.5 GPa, 20–800 °C, and 1–14 m NaCl. *Geochimica et Cosmochimica Acta*, *277*, 243–264. https://doi.org/10.1016/j.gca.2020.03.031

Frezzotti, M. L. (2019). Diamond growth from organic compounds in hydrous fluids deep within the Earth. *Nature Communications*, *10*(1), 1–8. https://doi.org/10.1038/s41467-019-12984-y

Frezzotti, M. L., & Ferrando, S. (2015). The chemical behavior of fluids released during deep subduction based on fluid inclusions. *American Mineralogist, 100(2-3)*, 352-377. https://doi.org/10.2138/am-2015-4933

Frezzotti, M. L., & Ferrando, S. (2018). The role of halogens in the lithospheric mantle. In *The role of halogens in terrestrial and extraterrestrial geochemical processes* (pp. 805-845). Cham: Springer Nature. https://doi.org/10.1007/978-3-319-61667-4_13

Frezzotti, M. L., Ferrando, S., Tecce, F., & Castelli, D. (2012). Water content and nature of solutes in shallow-mantle fluids from fluid inclusions. *Earth and Planetary Science Letters*, *351–352*, 70–83. https://doi.org/10.1016/j.epsl.2012.07.023

Frezzotti, M. L., & Touret, J. L. R. (2014). CO_2, carbonate-rich melts, and brines in the mantle. *Geoscience Frontiers*, *5*(5), 697–710. https://doi.org/10.1016/j.gsf.2014.03.014

Frost, D. J. (2006). The Stability of Hydrous Mantle Phases. *Reviews in Mineralogy and Geochemistry*, *62*(1), 243–271. https://doi.org/10.2138/rmg.2006.62.11

Frost, D. J., & McCammon, C. A. (2008). The redox state of Earth's mantle. *Annual Review of Earth and Planetary Sciences*, *36*(1), 389–420. https://doi.org/10.1146/annurev.earth.36.031207.124322

Frost, R. B., & Bucher, K. (1994). Is water responsible for geophysical anomalies in the deep continental crust? A petrological perspective. *Tectonophysics*, *231*(4), 293–309. https://doi.org/10.1016/0040-1951(94)90040-X

Frost, R. B., Fyfe, W. S., Tazaki, K., & Chan, T. (1989). Grain-boundary graphite in rocks and implications for high electrical conductivity in the lower crust. *Nature*, *340*(6229), 134–136. https://doi.org/10.1038/340134a0

Fukai, Y., Mori, K., & Shinomiya, H. (2003). The phase diagram and superabundant vacancy formation in Fe-H alloys under high hydrogen pressures. *Journal of Alloys and Compounds*, *348*(1–2), 105–109. https://doi.org/10.1016/S0925-8388(02)00806-X

Galvez, M. E., Connolly, J. A. D., & Manning, C. E. (2016). Implications for metal and volatile cycles from the pH of subduction zone fluids. *Nature*, *539*(7629), 420–424. https://doi.org/10.1038/nature20103

Gardés, E., Gaillard, F., & Tarits, P. (2014). Toward a unified hydrous olivine electrical conductivity law. *Geochemistry, Geophysics, Geosystems*, *15*(12), 4984–5000. https://doi.org/10.1002/2014GC005496

Golubkova, A., Schmidt, M. W., & Connolly, J. A. D. (2016). Ultra-reducing conditions in average mantle peridotites and in podiform chromitites: a thermodynamic model for moissanite (SiC) formation. *Contributions to Mineralogy and Petrology*, *171*(5), 1–17.

https://doi.org/10.1007/s00410-016-1253-9

Goncharov, A. G., Ionov, D. A., Doucet, L. S., & Pokhilenko, L. N. (2012). Thermal state, oxygen fugacity and C-O-H fluid speciation in cratonic lithospheric mantle: New data on peridotite xenoliths from the Udachnaya kimberlite, Siberia. *Earth and Planetary Science Letters*, *357–358*, 99–110. https://doi.org/10.1016/j.epsl.2012.09.016

Greenwood, N. N., & Earnshaw, A. (2012). *Chemistry of the Elements*. Oxford: Elsevier.

Guo, H., & Keppler, H. (2019). Electrical conductivity of NaCl-bearing aqueous fluids to 900 °C and 5 GPa. *Journal of Geophysical Research: Solid Earth*. https://doi.org/10.1029/2018jb016658

Guo, X., Yoshino, T., & Shimojuku, A. (2015). Electrical conductivity of albite-(quartz)-water and albite-water-NaCl systems and its implication to the high conductivity anomalies in the continental crust. *Earth and Planetary Science Letters*, *412*, 1–9. https://doi.org/10.1016/j.epsl.2014.12.021

Gupta, M. L., Sundar, A., & Sharma, S. R. (1991). Heat flow and heat generation in the Archaean Dharwar cratons and implications for the Southern Indian Shield geotherm and lithospheric thickness. *Tectonophysics*, *194*(1–2), 107–122. https://doi.org/10.1016/0040-1951(91)90275-W

Hanley, J. J., Pettke, T., Mungall, J. E., & Spooner, E. T. C. (2005). The solubility of platinum and gold in NaCl brines at 1.5 kbar, 600 to 800 °C: A laser ablation ICP-MS pilot study of synthetic fluid inclusions. *Geochimica et Cosmochimica Acta*, *69*(10), 2593–2611. https://doi.org/10.1016/j.gca.2004.11.005

Hashin, Z., & Shtrikman, S. (1962). A variational approach to the theory of the effective magnetic permeability of multiphase materials. *Journal of Applied Physics*, *33*(10), 3125–3131. https://doi.org/10.1063/1.1728579

Hasterok, D., & Chapman, D. S. (2011). Heat production and geotherms for the continental lithosphere. *Earth and Planetary Science Letters*, *307*(1–2), 59–70. https://doi.org/10.1016/j.epsl.2011.04.034

Heger, K., Uematsu, M., & Franck, E. U. (1980). The static dielectric constant of water at high pressures and temperatures to 500 MPa and 550 °C. *Berichte Der Bunsengesellschaft Für Physikalische Chemie*, *84*(8), 758–762. https://doi.org/10.1002/bbpc.19800840814

Helgeson, H. C., Kirkham, D. H., & Flowers, G. C. (1981). Theoretical prediction of the

thermodynamic behavior of aqueous electrolytes by high pressures and temperatures; IV, Calculation of activity coefficients, osmotic coefficients, and apparent molal and standard and relative partial molal properties to 600 °C and 5 kb. *American Journal of Science*, *281*(10), 1249–1516. https://doi.org/10.2475/ajs.281.10.1249

Helled, R., & Fortney, J. J. (2020). The interiors of Uranus and Neptune: Current understanding and open questions. *Philosophical Transactions of the Royal Society A, 378*(2187), 20190474. https://doi.org/10.1098/rsta.2019.0474

Helled, R., Nettelmann, N., & Guillot, T. (2020). Uranus and Neptune: origin, evolution and internal structure. *Space Science Reviews*. 216(3), 1-26. https://doi.org/10.1007/s11214-020-00660-3

Herzberg, C., Condie, K., & Korenaga, J. (2010). Thermal history of the Earth and its petrological expression. *Earth and Planetary Science Letters*, *292*(1–2), 79–88. https://doi.org/10.1016/j.epsl.2010.01.022

Hiroi, T., Fukai, Y., & Mori, K. (2005). The phase diagram and superabundant vacancy formation in Fe-H alloys revisited. *Journal of Alloys and Compounds*, *404–406* (spec. iss.), 252–255. https://doi.org/10.1016/j.jallcom.2005.02.076

Hirschmann, M. M., Aubaud, C., & Withers, A. C. (2005). Storage capacity of H_2O in nominally anhydrous minerals in the upper mantle. *Earth and Planetary Science Letters*, *236*(1–2), 167–181. https://doi.org/10.1016/j.epsl.2005.04.022

Hirschmann, M. M., Withers, A. C., Ardia, P., & Foley, N. T. (2012). Solubility of molecular hydrogen in silicate melts and consequences for volatile evolution of terrestrial planets. *Earth and Planetary Science Letters*, *345–348*, 38–48. https://doi.org/10.1016/j.epsl.2012.06.031

Ho, P. C., & Palmer, D. A. (1997). Ion association of dilute aqueous potassium chloride and potassium hydroxide solutions to 600 °C and 300 MPa determined by electrical conductance measurements. *Geochimica et Cosmochimica Acta*, *61*(15), 3027–3040. https://doi.org/10.1016/S0016-7037(97)00146-4

Holloway, J. R. (1971). Internally Heated Pressure Vessels. In *Research Techniques for High Pressure and High Temperature* (Vol. 53, pp. 217–258). Berlin, Heidelberg: GeoScienceWorld. https://doi.org/10.1007/978-3-642-88097-1_8

Holtzman, B. K. (2016). Questions on the existence, persistence, and mechanical effects of a

very small melt fraction in the asthenosphere. *Geochemistry, Geophysics, Geosystems*, *17*(2), 470–484. https://doi.org/10.1002/2015GC006102

Holzapfel, W. B., & Franck, E. U. (1966). Leitfähigkeit und Ionendissoziation des Wassers bis 1000 °C und 100 kbar. *Berichte Der Bunsengesellschaft Für Physikalische Chemie*, *70*(9–10), 1105–1112. https://doi.org/10.1002/BBPC.19660700937

Hou, R., Quan, Y., & Pan, D. (2020). Dielectric constant of supercritical water in a large pressure-temperature range. *Journal of Chemical Physics*, *153*(10), 101103. https://doi.org/10.1063/5.0020811

Huang, F., Daniel, I., Cardon, H., Montagnac, G., & Sverjensky, D. A. (2017). Immiscible hydrocarbon fluids in the deep carbon cycle. *Nature Communications*, *8*(1), 1–8. https://doi.org/10.1038/ncomms15798

Huang, F., & Sverjensky, D. A. (2019). Extended Deep Earth Water Model for predicting major element mantle metasomatism. *Geochimica et Cosmochimica Acta*, *254*, 192–230. https://doi.org/10.1016/j.gca.2019.03.027

Huang, J., Hao, J., Huang, F., & Sverjensky, D. A. (2019). Mobility of chromium in high temperature crustal and upper mantle fluids. *Geochemical Perspectives Letters*, *12*, 1–6. https://doi.org/10.7185/GEOCHEMLET.1926

Huang, Y., Nakatani, T., Nakamura, M., & McCammon, C. A. (2020). Experimental constraint on grain-scale fluid connectivity in subduction zones. *Earth and Planetary Science Letters*, *552*, 116610. https://doi.org/10.1016/j.epsl.2020.116610

Hwang, J. U., Lüdemann, H. D., & Hartmann, D. (1970). Die elektrische Leitfähigkeit konzentrierter wässriger Alkalihalogenidlösungen bei hohen Drucken und Temperaturen. *High Temp. High Pressures*, *2*, 651–669.

Hwang, S. L., Shen, P., Chu, H. T., Yui, T. F., Liou, J. G., Sobolev, N. V., & Shatsky, V. S. (2005). Crust-derived potassic fluid in metamorphic microdiamond. *Earth and Planetary Science Letters*, *231*(3–4), 295–306. https://doi.org/10.1016/j.epsl.2005.01.002

Irifune, T., Kurio, A., Sakamoto, S., Inoue, T., & Sumiya, H. (2003). Materials: Ultrahard polycrystalline diamond from graphite. *Nature*, *421*(6923), 599–600. https://doi.org/10.1038/421599b

Ishimaru, S., Arai, S., & Shukuno, H. (2009). Metal-saturated peridotite in the mantle wedge inferred from metal-bearing peridotite xenoliths from Avacha volcano, Kamchatka. *Earth*

and Planetary Science Letters, *284*(3–4), 352–360. https://doi.org/10.1016/j.epsl.2009.04.042

Ito, K., & Bernstein, H. J. (1956). The vibrational spectra of the formate, acetate, and oxalate ions. *Canadian Journal of Chemistry*, *34*(2), 170–178. https://doi.org/10.1139/v56-021

Izraeli, E. S., Harris, J. W., & Navon, O. (2001). Brine inclusions in diamonds: A new upper mantle fluid. *Earth and Planetary Science Letters*, *187*(3–4), 323–332. https://doi.org/10.1016/S0012-821X(01)00291-6

Izraeli, E. S., Harris, J. W., & Navon, O. (2004). Fluid and mineral inclusions in cloudy diamonds from Koffiefontein, South Africa. *Geochimica et Cosmochimica Acta*, *68*(11), 2561–2575. https://doi.org/10.1016/j.gca.2003.09.005

Johnson, J. W., Oelkers, E. H., & Helgeson, H. C. (1992). SUPCRT92: A software package for calculating the standard molal thermodynamic properties of minerals, gases, aqueous species, and reactions from 1 to 5000 bar and 0 to 1000 °C. *Computers and Geosciences*, *18*(7), 899–947. https://doi.org/10.1016/0098-3004(92)90029-Q

Jones, A. G., Evans, R. L., Muller, M. R., Hamilton, M. P., Miensopust, M. P., Garcia, X., … Wasborg, J. (2009). Area selection for diamonds using magnetotellurics: Examples from southern Africa. *Lithos*, *112*, 83–92. https://doi.org/10.1016/j.lithos.2009.06.011

Jones, A. G., Ferguson, I. J., Chave, A. D., Evans, R. L., & McNeice, G. W. (2001). Electric lithosphere of the Slave craton. *Geology*, *29*(5), 423–426. https://doi.org/10.1130/0091-7613(2001)029<0423:ELOTSC>2.0.CO;2

Jones, A. G., Lezaeta, P., Ferguson, I. J., Chave, A. D., Evans, R. L., Garcia, X., & Spratt, J. (2003). The electrical structure of the Slave craton. *Lithos*, *71*(2–4), 505–527. https://doi.org/10.1016/j.lithos.2003.08.001

Jorgensen, W. L., Chandrasekhar, J., Madura, J. D., Impey, R. W., & Klein, M. L. (1983). Comparison of simple potential functions for simulating liquid water. *The Journal of Chemical Physics*, *79*(2), 926–935. https://doi.org/10.1063/1.445869

Journaux, B., Daniel, I., Caracas, R., Montagnac, G., & Cardon, H. (2013). Influence of NaCl on ice VI and ice VII melting curves up to 6 GPa, implications for large icy moons. *Icarus*, *226*(1), 355–363. https://doi.org/10.1016/j.icarus.2013.05.039

Kaminsky, F. (2012). Mineralogy of the lower mantle: A review of "super-deep" mineral inclusions in diamond. *Earth-Science Reviews,* 110(1-4), 127-147.

https://doi.org/10.1016/j.earscirev.2011.10.005

Kato, A., Iidaka, T., Ikuta, R., Yoshida, Y., Katsumata, K., Iwasaki, T., … Hirata, N. (2010). Variations of fluid pressure within the subducting oceanic crust and slow earthquakes. *Geophysical Research Letters*, *37*(14), L14310. https://doi.org/10.1029/2010GL043723

Katz, R. F., Spiegelman, M., & Langmuir, C. H. (2003). A new parameterization of hydrous mantle melting. *Geochemistry, Geophysics, Geosystems*, *4*(9), 1073. https://doi.org/10.1029/2002GC000433

Kawamoto, T. (2018). Hydrous phases and water transport in the subducting slab. In *Water in Nominally Anhydrous Minerals* (Vol. 62, pp. 273–290). Berlin, Heidelberg: GeoScienceWorld. https://doi.org/10.2138/rmg.2006.62.12

Kell, G. S., McLaurin, G. E., & Whalley, E. (1978). The PVT properties of water, IV. Liquid water in the range 150-350 °C, from saturation to 1 kbar. *Proceedings of the Royal Society of London. A. Mathematical and Physical Sciences*, *360*(1702), 389–402. https://doi.org/10.1098/rspa.1978.0075

Kepezhinskas, P., Berdnikov, N., Kepezhinskas, N., & Konovalova, N. (2022). Metals in Avachinsky peridotite xenoliths with implications for redox heterogeneity and metal enrichment in the Kamchatka mantle wedge. *Lithos*, *412–413*, 106610. https://doi.org/10.1016/j.lithos.2022.106610

Keppler, H. (1996). Constraints from partitioning experiments on the composition of subduction-zone fluids. *Nature*, *380*(6571), 237–240. https://doi.org/10.1038/380237a0

Keppler, H. (2017). Fluids and trace element transport in subduction zones. *American Mineralogist, 102*(1), 5-20. https://doi.org/10.2138/am-2017-5716

Klein-BenDavid, O., Izraeli, E. S., Hauri, E., & Navon, O. (2004). Mantle fluid evolution - A tale of one diamond. *Lithos*, *77*(1-4, spec. iss.), 243–253. https://doi.org/10.1016/j.lithos.2004.04.003

Klein-BenDavid, O., Izraeli, E. S., Hauri, E., & Navon, O. (2007). Fluid inclusions in diamonds from the Diavik mine, Canada and the evolution of diamond-forming fluids. *Geochimica et Cosmochimica Acta*, *71*(3), 723–744. https://doi.org/10.1016/j.gca.2006.10.008

Konzett, J., Wirth, R., Hauzenberger, C., & Whitehouse, M. (2013). Two episodes of fluid migration in the Kaapvaal Craton lithospheric mantle associated with Cretaceous kimberlite activity: Evidence from a harzburgite containing a unique assemblage of metasomatic

zirconium-phases. *Lithos*, *182–183*, 165–184. https://doi.org/10.1016/j.lithos.2013.10.005

Korenaga, J. (2006). Archean geodynamics and the thermal evolution of Earth. *Geophysical Monograph-American Geophysical Union*, 164, 7. https://doi.org/10.1029/164GM03

Krishnamurty, K. V, & Harris, G. M. (1961). The chemistry of the metal oxalato complexes. *Chemical Reviews*, *61*(3), 213–246. https://doi:10.1021/cr60211a001

Kruijer, T. S., Kleine, T., Fischer-Gödde, M., & Sprung, P. (2015). Lunar tungsten isotopic evidence for the late veneer. *Nature*, *520*(7548), 534–537. https://doi.org/10.1038/nature14360

Kunz, J., Staudacher, T., & Allègre, C. J. (1998). Plutonium-fission xenon found in Earth's mantle. *Science*, *280*(5365), 877–880. https://doi.org/10.1126/science.280.5365.877

Kusham, Naick, B. P., Pratap, A., & Naganjaneyulu, K. (2021). Magnetotelluric 3-D full tensor inversion in the Dharwar craton, India: Mapping of subduction polarity and kimberlitic melt. *Physics of the Earth and Planetary Interiors*, *315*, 106708. https://doi.org/10.1016/j.pepi.2021.106708

Kusham, Pratap, A., Naick, B. P., & Naganjaneyulu, K. (2018). Lithospheric architecture in the Archaean Dharwar craton, India: A magnetotelluric model. *Journal of Asian Earth Sciences*, *163*, 43–53. https://doi.org/10.1016/j.jseaes.2018.05.022

Kusham, Pratap, A., Naick, B. P., & Naganjaneyulu, K. (2019). Crustal and lithospheric mantle conductivity structure in the Dharwar craton, India. *Journal of Asian Earth Sciences*, *176*, 253–263. https://doi.org/10.1016/j.jseaes.2019.02.015

Lammer, H., Zerkle, A. L., Gebauer, S., Tosi, N., Noack, L., Scherf, M., … Nikolaou, A. (2018). Origin and evolution of the atmospheres of early Venus, Earth and Mars. *Astronomy and Astrophysics Review* , 26(1), 1-72. https://doi.org/10.1007/s00159-018-0108-y

Lathe, C., Koch-Müller, M., Wirth, R., van Westrenen, W., Mueller, H. J., Schilling, F. R., & Lauterjung, J. (2005). The influence of OH in coesite on the kinetics of the coesite-quartz phase transition. *American Mineralogist*, *90*(1), 36–43. https://doi.org/10.2138/am.2005.1662

Lazarov, M., Woodland, A. B., & Brey, G. P. (2009). Thermal state and redox conditions of the Kaapvaal mantle: A study of xenoliths from the Finsch mine, South Africa. *Lithos*, *112*, 913–923. https://doi.org/10.1016/j.lithos.2009.03.035

Leachman, J. W., Jacobsen, R. T., Penoncello, S. G., & Lemmon, E. W. (2009). Fundamental

equations of state for parahydrogen, normal hydrogen, and orthohydrogen. *Journal of Physical and Chemical Reference Data*, *38*(3), 721–748. https://doi.org/10.1063/1.3160306

Li, J., Bassett, W. A., Chou, I. M., Ding, X., Li, S., & Wang, X. (2016). An improved hydrothermal diamond anvil cell. *Review of Scientific Instruments*, *87*(5), 053108. https://doi.org/10.1063/1.4947506

Li, Y. (2017). Immiscible C-H-O fluids formed at subduction zone conditions. *Geochemical Perspectives Letters*, *3*(1), 12–21. https://doi.org/10.7185/geochemlet.1702

Liou, J. G., Tsujimori, T., Yang, J.-S., Zhang, R. Y., & Ernst, W. G. (2014). Recycling of crustal materials through study of ultrahigh-pressure minerals in collisional orogens, ophiolites, and mantle xenoliths: A review. *Journal of Asian Earth Sciences*, 96, 386-420. https://doi.org/10.1016/j.jseaes.2014.09.011

Litasov, K. D., Shatskiy, A., Ohtani, E., & Yaxley, G. M. (2013). Solidus of alkaline carbonatite in the deep mantle. *Geology*, *41*(1), 79–82. https://doi.org/10.1130/G33488.1

Lussier, A., Ball, N. A., Hawthorne, F. C., Henry, D. J., Shimizu, R., Ogasawara, Y., & Ota, T. (2016). Maruyamaite, $K(MgAl_2)(Al_5Mg)Si_6O_{18}(BO_3)_3(OH)_3O$, a potassium-dominant tourmaline from the ultrahigh-pressure Kokchetav massif, northern Kazakhstan: Description and crystal structure. *American Mineralogist*, *101*(2), 355–361. https://doi.org/10.2138/am-2016-5359

Luth, W. C., & Tuttle, O. F. (1963). Externally heated cold-seal pressure vessels for use to 10,000 bars and 750 °C. *American Mineralogist*, *48*(11–12), 1401–1403.

Lvovich, V. F. (2015). *Impedance spectroscopy: Applications to electrochemical and dielectric phenomena*. Hoboken, NJ: John Wiley & Sons, Inc. https://doi.org/10.1002/9781118164075

Mangold, K., & Franck, E. U. (1969). Elektrische Leitfähigkeit wäßriger Lösungen bei hohen Temperaturen und Drucken. II [1]. Alkalichloride in Wasser bis 1000 °C und 12 kbar. *Berichte Der Bunsengesellschaft Für Physikalische Chemie*, *73*(1), 21–27. https://doi.org/10.1002/BBPC.19690730107

Manning, C. E. (1994). The solubility of quartz in H_2O in the lower crust and upper mantle. *Geochimica et Cosmochimica Acta*, *58*(22), 4831–4839. https://doi.org/10.1016/0016-7037(94)90214-3

Manning, C. E. (2004). The chemistry of subduction-zone fluids. *Earth and Planetary Science Letters*, *223*(1–2), 1–16. https://doi.org/10.1016/j.epsl.2004.04.030

Manning, C. E. (2018). Fluids of the Lower Crust: Deep Is Different. *Annual Review of Earth and Planetary Sciences*, *46*(1), 67–97. https://doi.org/10.1146/annurev-earth-060614-105224

Manning, C. E., & Aranovich, L. Y. (2014). Brines at high pressure and temperature: Thermodynamic, petrologic and geochemical effects. *Precambrian Research*, *253*, 6–16. https://doi.org/10.1016/j.precamres.2014.06.025

Manning, C. E., & Frezzotti, M. L. (2020). Subduction-zone fluids. *Elements*, *16*(6), 395–400. https://doi.org/10.2138/GSELEMENTS.16.6.395

Marcus, Y. (1988). Ionic Radii in Aqueous Solutions. *Chemical Reviews*, *88*(8), 1475–1498. https://doi.org/10.1021/cr00090a003

Mareschal, M., Fyfe, W. S., Percival, J., & Chan, T. (1992). Grain-boundary graphite in Kapuskasing gneisses and implications for lower-crustal conductivity. *Nature*, *357*(6380), 674–676. https://doi.org/10.1038/357674a0

Marshall, W., & Frantz, J. D. (1987). Electrical conductance measurement of dilute, aqueous electrolytes at temperatures to 800 ℃ and pressures to 4000 bars: Techniques and interpretations. In G. Ulmer & H. Barnes (Eds.), *Hydrothermal and Experimental Techniques* (pp. 261–292). New York, NY: Wiley-Interscience.

Marty, B. (1989). Neon and xenon isotopes in MORB: implications for the earth-atmosphere evolution. *Earth and Planetary Science Letters*, *94*(1–2), 45–56. https://doi.org/10.1016/0012-821X(89)90082-4

Matjuschkin, V., Woodland, A. B., & Yaxley, G. M. (2019). Methane-bearing fluids in the upper mantle: an experimental approach. *Contributions to Mineralogy and Petrology*, *174*(1), 1-14. https://doi.org/10.1007/s00410-018-1536-4

McCammon, C. A., & Kopylova, M. G. (2004). A redox profile of the Slave mantle and oxygen fugacity control in the cratonic mantle. *Contributions to Mineralogy and Petrology*, *148*(1), 55–68. https://doi.org/10.1007/s00410-004-0583-1

Mibe, K., Fujii, T., & Yasuda, A. (1998). Connectivity of aqueous fluid in the Earth's upper mantle. *Geophysical Research Letters*, *25*(8), 1233–1236. https://doi.org/10.1029/98GL00872

Mierdel, K., Keppler, H., Smyth, J. R., & Langenhorst, F. (2007). Water solubility in aluminous orthopyroxene and the origin of Earth's asthenosphere. *Science*, *315*(5810), 364–368.

https://doi.org/10.1126/science.1135422

Mikhno, A. O., Schmidt, U., & Korsakov, A. V. (2014). Origin of K-cymrite and kokchetavite in the polyphase mineral inclusions from Kokchetav UHP calc-silicate rocks: evidence from confocal Raman imaging. *European Journal of Mineralogy*, *25*(5), 807–816. https://doi.org/10.1127/0935-1221/2013/0025-2321

Moore, G., Vennemann, T., & Carmichael, I. S. E. (1998). An empirical model for the solubility of H_2O in magmas to 3 kilobars. *American Mineralogist*, *83*(1–2), 36–42. https://doi.org/10.2138/am-1998-1-203

Mukhopadhyay, S. (2012). Early differentiation and volatile accretion recorded in deep-mantle neon and xenon. *Nature*, *486*(7401), 101–104. https://doi.org/10.1038/nature11141

Musselwhite, D. S., Drake, M. J., & Swindle, T. D. (1991). Early outgassing of Mars supported by differential water solubility of iodine and xenon. *Nature*, *352*(6337), 697–699. https://doi.org/10.1038/352697a0

Naif, S., Selway, K., Murphy, B. S., Egbert, G. D., & Pommier, A. (2021). Electrical conductivity of the lithosphere-asthenosphere system. *Physics of the Earth and Planetary Interiors, 313,* 106661, 24 p. https://doi.org/10.1016/j.pepi.2021.106661

Navon, O., Hutcheon, I. D., Rossman, G. R., & Wasserburg, G. J. (1988). Mantle-derived fluids in diamond micro-inclusions. *Nature*, *335*(6193), 784–789. https://doi.org/10.1038/335784a0

Nazzareni, S., Nestola, F., Zanon, V., Bindi, L., Scricciolo, E., Petrelli, M., … Giuli, G. (2019). Discovery of moissanite in a peralkaline syenite from the Azores Islands. *Lithos*, *324–325*, 68–73. https://doi.org/10.1016/j.lithos.2018.10.036

Nettelmann, N., Helled, R., Fortney, J. J., & Redmer, R. (2013). New indication for a dichotomy in the interior structure of Uranus and Neptune from the application of modified shape and rotation data. *Planetary and Space Science*, *77*, 143–151. https://doi.org/10.1016/j.pss.2012.06.019

Newton, R. C., & Manning, C. E. (2006). Solubilities of corundum, wollastonite and quartz in H_2O-NaCl solutions at 800 °C and 10 kbar: Interaction of simple minerals with brines at high pressure and temperature. *Geochimica et Cosmochimica Acta*, *70*(22), 5571–5582. https://doi.org/10.1016/j.gca.2006.08.012

Newton, R. C., Touret, J. L. R., & Aranovich, L. Y. (2014). Fluids and H_2O activity at the onset

of granulite facies metamorphism. *Precambrian Research*, *253*, 17–25. https://doi.org/10.1016/j.precamres.2014.06.009

Ni, H., Chen, Q., & Keppler, H. (2014). Electrical conductivity measurements of aqueous fluids under pressure with a hydrothermal diamond anvil cell. *Review of Scientific Instruments*, *85*(11), 115107. https://doi.org/10.1063/1.4902152

Ni, H., Keppler, H., & Behrens, H. (2011). Electrical conductivity of hydrous basaltic melts: Implications for partial melting in the upper mantle. *Contributions to Mineralogy and Petrology*, *162*(3), 637–650. https://doi.org/10.1007/s00410-011-0617-4

Ni, H., Keppler, H., Manthilake, G., & Katsura, T. (2011). Electrical conductivity of dry and hydrous $NaAlSi_3O_8$ glasses and liquids at high pressures. *Contributions to Mineralogy and Petrology*, *162*(3), 501–513. https://doi.org/10.1007/s00410-011-0608-5

Nightingale, E. R. (1959). Phenomenological theory of ion solvation. Effective radii of hydrated ions. *Journal of Physical Chemistry*, *63*(9), 1381–1387. https://doi.org/10.1021/j150579a011

O'Neill, H. S. C., & Pownceby, M. I. (1993). Thermodynamic data from redox reactions at high temperatures. I. An experimental and theoretical assessment of the electrochemical method using stabilized zirconia electrolytes, with revised values for the Fe-"FeO", Co-CoO, Ni-NiO and Cu-Cu_2O oxygen buffe. *Contributions to Mineralogy and Petrology*, *114*(3), 296–314. https://doi.org/10.1007/BF01046533

O'Reilly, S. Y., & Griffin, W. L. (2013). Mantle metasomatism. In *Metasomatism and the chemical transformation of rock* (pp. 471-533). Heidelberg: Springer-Verlag Berlin. https://doi.org/10.1007/978-3-642-28394-9_12

Ohtani, E. (2015). Hydrous minerals and the storage of water in the deep mantle. *Chemical Geology*, *418*, 6–15. https://doi.org/10.1016/j.chemgeo.2015.05.005

Ohtani, E., Yuan, L., Ohira, I., Shatskiy, A., & Litasov, K. D. (2018). Fate of water transported into the deep mantle by slab subduction. *Journal of Asian Earth Sciences*, *167*, 2–10. https://doi.org/10.1016/j.jseaes.2018.04.024

Ohtomo, N., & Arakawa, K. (1980). Neutron Diffraction Study of Aqueous Ionic Solutions. II. Aqueous Solutions of Sodium Chloride and Potassium Chloride. *Bulletin of the Chemical Society of Japan*, *53*(7), 1789–1794. https://doi.org/10.1246/bcsj.53.1789

Palot, M., Jacobsen, S. D., Townsend, J. P., Nestola, F., Marquardt, K., Miyajima, N., …

Pearson, D. G. (2016). Evidence for H_2O-bearing fluids in the lower mantle from diamond inclusion. *Lithos*, *265*, 237–243. https://doi.org/10.1016/j.lithos.2016.06.023

Pamato, M. G., Myhill, R., Boffa Ballaran, T., Frost, D. J., Heidelbach, F., & Miyajima, N. (2015). Lower-mantle water reservoir implied by the extreme stability of a hydrous aluminosilicate. *Nature Geoscience*, *8*(1), 75–79. https://doi.org/10.1038/ngeo2306

Pan, D., Spanu, L., Harrison, B., Sverjensky, D. A., & Galli, G. (2013). Dielectric properties of water under extreme conditions and transport of carbonates in the deep Earth. *Proceedings of the National Academy of Sciences*, *110*(17), 6646–6650. https://doi.org/10.1073/pnas.1221581110

Patkó, L., Novák, A., Klébesz, R., Liptai, N., Lange, T. P., Molnár, G., … Szabó, C. (2021). Effect of metasomatism on the electrical resistivity of the lithospheric mantle – An integrated research using magnetotelluric sounding and xenoliths beneath the Nógrád-Gömör volcanic field. *Global and Planetary Change*, *197*, 103389. https://doi.org/10.1016/j.gloplacha.2020.103389

Peacock, S. M. (1990). Fluid processes in subduction zones. *Science*, *248*(4953), 329–337. https://doi.org/10.1126/science.248.4953.329

Peacock, S. M., & Hyndman, R. D. (1999). Hydrous minerals in the mantle wedge and the maximum depth of subduction thrust earthquakes. *Geophysical Research Letters*, *26*(16), 2517–2520. https://doi.org/10.1029/1999GL900558

Pitzer, K. S. (1983). Dielectric constant of water at very high temperature and pressure. *Proceedings of the National Academy of Sciences*, *80*(14), 4575–4576. https://doi.org/10.1073/pnas.80.14.4575

Pitzer, K. S., & Sterner, S. M. (1994). Equations of state valid continuously from zero to extreme pressures for H_2O and CO_2. *The Journal of Chemical Physics*, *101*(4), 3111–3116. https://doi.org/10.1063/1.467624

Plank, T., & Manning, C. E. (2019). Subducting carbon. *Nature* , 574(7778), 343-352. https://doi.org/10.1038/s41586-019-1643-z

Podolak, M., Helled, R., & Schubert, G. (2019). Effect of non-adiabatic thermal profiles on the inferred compositions of Uranus and Neptune. *Monthly Notices of the Royal Astronomical Society*, *487*(2), 2653–2664. https://doi.org/10.1093/mnras/stz1467

Pommier, A. (2014). Interpretation of Magnetotelluric Results Using Laboratory Measurements.

Surveys in Geophysics, *35*(1), 41–84. https://doi.org/10.1007/s10712-013-9226-2

Pommier, A., & Evans, R. L. (2017). Constraints on fluids in subduction zones from electromagnetic data. *Geosphere*, *13*(4), 1026-1041.. https://doi.org/10.1130/GES01473.1

Prouteau, G., Scaillet, B., Pichavant, M., & Maury, R. C. (1999). Fluid-present melting of ocean crust in subduction zones. *Geology*, *27*(12), 1111–1114. https://doi.org/10.1130/0091-7613(1999)027<1111:FPMOOC>2.3.CO;2

Pujol-Solà, N., Garcia-Casco, A., Proenza, J. A., González-Jiménez, J. M., del Campo, A., Colás, V., … Roqué-Rosell, J. (2020). Diamond forms during low pressure serpentinisation of oceanic lithosphere. *Geochemical Perspectives Letters*, *15*, 19–24. https://doi.org/10.7185/geochemlet.2029

Pujol-Solà, N., Proenza, J. A., Garcia-Casco, A., González-Jiménez, J. M., Andreazini, A., Melgarejo, J. C., & Gervilla, F. (2018). An alternative scenario on the origin of ultra-high pressure (UHP) and super-reduced (SuR) minerals in ophiolitic chromitites: A case study from the Mercedita deposit (Eastern Cuba). *Minerals*, *8*(10), 433. https://doi.org/10.3390/min8100433

Quist, A. S., & Marshall, W. (1968). Electrical conductances of aqueous sodium chloride solutions from 0 to 800 °C and at pressures to 4000 bars. *The Journal of Physical Chemistry*, *72*(2), 684–703. https://doi.org/10.1021/j100848a050

Randles, J. E. B. (1947). Kinetics of rapid electrode reactions. *Faraday Discussions*, *1*, 11–19. https://doi.org/10.1039/DF9470100011

Rege, S., Griffin, W. L., Pearson, N. J., Araujo, D., Zedgenizov, D. A., & O'Reilly, S. Y. (2010). Trace-element patterns of fibrous and monocrystalline diamonds: Insights into mantle fluids. *Lithos*, *118*(3–4), 313–337. https://doi.org/10.1016/j.lithos.2010.05.007

Ritzert, G., & Franck, E. U. (1968). Elektrische Leitfähigkeit wäßriger Lösungen bei hohen Temperaturen und Drucken. I. KCl, $BaCl_2$, $Ba(OH)_2$ und $MgSO_4$ bis 750 °C und 6 kbar. *Berichte Der Bunsengesellschaft Für Physikalische Chemie*, *72*(7), 798–808. https://doi.org/10.1002/BBPC.19680720712

Rozsa, V., & Galli, G. (2021). Solvation of simple ions in water at extreme conditions. *Journal of Chemical Physics*, *154*(14), 144501. https://doi.org/10.1063/5.0046193

Rubie, D. C., Frost, D. J., Mann, U., Asahara, Y., Nimmo, F., Tsuno, K., … Palme, H. (2011). Heterogeneous accretion, composition and core-mantle differentiation of the Earth. *Earth*

and Planetary Science Letters, *301*(1–2), 31–42. https://doi.org/10.1016/j.epsl.2010.11.030

Rudnick, R. L., & Fountain, D. M. (1995). Nature and composition of the continental crust: A lower crustal perspective. *Reviews of Geophysics*, 33(3), 267-309. https://doi.org/10.1029/95RG01302

Rudnick, R. L., & Nyblade, A. A. (1999). The thickness and heat production of Archean lithosphere: constraints from xenolith thermobarometry and surface heat flow. *Mantle Petrology: Field Observations and High Pressure Experimentation: A Tribute to Francis R.(Joe) Boyd*, *6*, 3–12.

Rüpke, L. H., Morgan, J. P., Hort, M., & Connolly, J. A. D. (2004). Serpentine and the subduction zone water cycle. *Earth and Planetary Science Letters*, *223*(1–2), 17–34. https://doi.org/10.1016/j.epsl.2004.04.018

Russell, J. K., & Kopylova, M. G. (1999). A steady state conductive geotherm for the north central Slave, Canada: Inversion of petrological data from the Jericho Kimberlite pipe. *Journal of Geophysical Research: Solid Earth*, *104*(B4), 7089–7101. https://doi.org/10.1029/1999jb900012

Rustioni, G., Audétat, A., & Keppler, H. (2019). Experimental evidence for fluid-induced melting in subduction zones. *Geochemical Perspectives Letters*, *11*, 49–54. https://doi.org/10.7185/geochemlet.1925

Rustioni, G., Audétat, A., & Keppler, H. (2021). The composition of subduction zone fluids and the origin of the trace element enrichment in arc magmas. *Contributions to Mineralogy and Petrology*, *176*(7), 1–19. https://doi.org/10.1007/s00410-021-01810-8

Ryabchikov, I. D., Schreyer, W., & Abraham, K. (1982). Compositions of aqueous fluids in equilibrium with pyroxenes and olivines at mantle pressures and temperatures. *Contributions to Mineralogy and Petrology*, *79*(1), 80–84. https://doi.org/10.1007/BF00376964

Rychert, C. A., Tharimena, S., Harmon, N., Wang, S., Constable, S., Kendall, J. M., … Schlaphorst, D. (2021). A dynamic lithosphere–asthenosphere boundary near the equatorial Mid-Atlantic ridge. *Earth and Planetary Science Letters*, *566*, 116949. https://doi.org/10.1016/j.epsl.2021.116949

Sakuma, H., & Ichiki, M. (2016). Electrical conductivity of NaCl-H_2O fluid in the crust. *Journal of Geophysical Research: Solid Earth*, *121*(2), 577–594.

https://doi.org/10.1002/2015JB012219

Sanchez-Valle, C., Mantegazzi, D., Bass, J. D., & Reusser, E. (2013). Equation of state, refractive index and polarizability of compressed water to 7 GPa and 673 K. *Journal of Chemical Physics*, *138*(5), 054505. https://doi.org/10.1063/1.4789359

Savova-Stoynov, B., & Stoynov, Z. B. (1987). Analysis of the inductance influence on the measured electrochemical impedance. *Journal of Applied Electrochemistry*, *17*(6), 1150–1158. https://doi.org/10.1007/BF01023598

Saxena, S. K., & Dubrovinsky, L. S. (2000). Iron phases at high pressures and temperatures: Phase transition and melting. *American Mineralogist*, *85*(2), 372–375. https://doi.org/10.2138/am-2000-2-316

Scheibe, L., Nettelmann, N., & Redmer, R. (2019). Thermal evolution of Uranus and Neptune: I. Adiabatic models. *Astronomy and Astrophysics*, *632*, A70. https://doi.org/10.1051/0004-6361/201936378

Schertl, H. P., & Sobolev, N. V. (2013). The Kokchetav Massif, Kazakhstan: "Type locality" Of diamond-bearing UHP metamorphic rocks. *Journal of Asian Earth Sciences*, 63, 5-38. https://doi.org/10.1016/j.jseaes.2012.10.032

Schiano, P., Provost, A., Clocchiatti, R., & Faure, F. (2006). Transcrystalline melt migration and earth's mantle. *Science*, *314*(5801), 970–974. https://doi.org/10.1126/science.1132485

Schmidt, B. C., & Keppler, H. (2002). Experimental evidence for high noble gas solubilities in silicate melts under mantle pressures. *Earth and Planetary Science Letters*, *195*(3–4), 277–290. https://doi.org/10.1016/S0012-821X(01)00584-2

Schmidt, C., Steele-MacInnis, M., Watenphul, A., & Wilke, M. (2013). Calibration of zircon as a Raman spectroscopic pressure sensor to high temperatures and application to water-silicate melt systems. *American Mineralogist*, *98*(4), 643–650. https://doi.org/10.2138/am.2013.4143

Schrauder, M., Koeberl, C., & Navon, O. (1996). Trace element analyses of fluid-bearing diamonds from Jwaneng, Botswana. *Geochimica et Cosmochimica Acta*, *60*(23), 4711–4724. https://doi.org/10.1016/S0016-7037(96)00274-8

Schrauder, M., & Navon, O. (1994). Hydrous and carbonatitic mantle fluids in fibrous diamonds from Jwaneng, Botswana. *Geochimica et Cosmochimica Acta*, *58*(2), 761–771. https://doi.org/10.1016/0016-7037(94)90504-5

Seno, T., & Rehman, H. U. (2011). When and why the continental crust is subducted: Examples of Hindu Kush and Burma. *Gondwana Research*, *19*(1), 327–333. https://doi.org/10.1016/j.gr.2010.05.011

Seward, T. M., & Franck, E. U. (1981). System hydrogen - water up to 440 °C and 2500 bar pressure. *Berichte Der Bunsengesellschaft/Physical Chemistry Chemical Physics*, *85*(1), 2–7. https://doi.org/10.1002/bbpc.19810850103

Sharp, Z. D., McCubbin, F. M., & Shearer, C. K. (2013). A hydrogen-based oxidation mechanism relevant to planetary formation. *Earth and Planetary Science Letters*, *380*, 88–97. https://doi.org/10.1016/j.epsl.2013.08.015

Sharygin, A. V., Wood, R. H., Zimmerman, G. H., & Balashov, V. N. (2002). Multiple ion association versus redissociation in aqueous NaCl and KCl at high temperatures. *Journal of Physical Chemistry B*, *106*(28), 7121–7134. https://doi.org/10.1021/jp013647uCCC:22.00

Shen, A. H., & Keppler, H. (1995). Infrared spectroscopy of hydrous silicate melts to 1000 °C and 10 kbar: direct observation of H_2O speciation in a diamond-anvil cell. *American Mineralogist*, *80*(11–12), 1335–1338. https://doi.org/10.2138/am-1995-11-1223

Shen, A. H., & Keppler, H. (1997). Direct observation of complete miscibility in the albite-H_2O system. *Nature*, *385*(6618), 710–712. https://doi.org/10.1038/385710a0

Shibata, T., Takahashi, E., & Matsuda, J. I. (1998). Solubility of neon, argon, krypton, and xenon in binary and ternary silicate systems: a new view on noble gas solubility. *Geochimica et Cosmochimica Acta*, *62*(7), 1241–1253. https://doi.org/10.1016/S0016-7037(98)00046-5

Shibazaki, Y., Terasaki, H., Ohtani, E., Tateyama, R., Nishida, K., Funakoshi, K.-I., & Higo, Y. (2014). High-pressure and high-temperature phase diagram for $Fe_{0.9}Ni_{0.1}$-H alloy. *Physics of the Earth and Planetary Interiors*, *228*, 192–201. https://doi.org/10.1016/j.pepi.2013.12.013

Shimojuku, A., Yoshino, T., & Yamazaki, D. (2014). Electrical conductivity of brine-bearing quartzite at 1 GPa: Implications for fluid content and salinity of the crust. *Earth, Planets and Space*, *66*(1), 1-9. https://doi.org/10.1186/1880-5981-66-2

Shinozaki, A., Kagi, H., Noguchi, N., Hirai, H., Ohfuji, H., Okada, T., … Yagi, T. (2014). Formation of SiH_4 and H_2O by the dissolution of quartz in H_2 fluid under high pressure and temperature. *American Mineralogist*, *99*(7), 1265–1269. https://doi.org/10.2138/am.2014.4798

Shiryaev, A. A., Griffin, W. L., & Stoyanov, E. (2011). Moissanite (SiC) from kimberlites:

Polytypes, trace elements, inclusions and speculations on origin. *Lithos, 122*(3–4), 152–164. https://doi.org/10.1016/j.lithos.2010.12.011

Sinmyo, R., & Keppler, H. (2017). Electrical conductivity of NaCl-bearing aqueous fluids to 600 °C and 1 GPa. *Contributions to Mineralogy and Petrology, 172*(1), 1-12. https://doi.org/10.1007/s00410-016-1323-z

Smith, E. M., Kopylova, M. G., Nowell, G. M., Graham Pearson, D., & Ryder, J. (2012). Archean mantle fluids preserved in fibrous diamonds from Wawa, Superior craton. *Geology*, *40*(12), 1071–1074. https://doi.org/10.1130/G33231.1

Smith, E. M., Shirey, S. B., Richardson, S. H., Nestola, F., Bullock, E. S., Wang, J., & Wang, W. (2018). Blue boron-bearing diamonds from Earth's lower mantle. *Nature*, 560 (7716), 84-87. https://doi.org/10.1038/s41586-018-0334-5

Smyth, J. R. (2018). Hydrogen in high pressure silicate and oxide mineral structures. In *Reviews in Mineralogy and Geochemistry*, 62(1), 85-115. https://doi.org/10.2138/rmg.2006.62.5

Smythe, D. J., & Brenan, J. M. (2016). Magmatic oxygen fugacity estimated using zircon-melt partitioning of cerium. *Earth and Planetary Science Letters*, *453*, 260–266. https://doi.org/10.1016/j.epsl.2016.08.013

Soubiran, F., & Militzer, B. (2015). Miscibility calculations for water and hydrogen in giant planets. *Astrophysical Journal, 806*(2), 228. https://doi.org/10.1088/0004-637X/806/2/228

Stolte, N., & Pan, D. (2019). Large presence of carbonic acid in CO_2-rich aqueous fluids under Earth's mantle conditions. *Journal of Physical Chemistry Letters*, *10*(17), 5135–5141. https://doi.org/10.1021/acs.jpclett.9b01919

Stolte, N., Yu, J., Chen, Z., Sverjensky, D. A., & Pan, D. (2021). Water-gas shift reaction produces formate at extreme pressures and temperatures in deep earth fluids. *Journal of Physical Chemistry Letters*, *12*(17), 4292–4298. https://doi.org/10.1021/acs.jpclett.1c00563

Sverjensky, D. A. (2019). Thermodynamic modeling of fluids from surficial to mantle Conditions. *Journal of the Geological Society*, 176(2), 348-374. https://doi.org/10.1144/jgs2018-105

Sverjensky, D. A., Daniel, I., & Brovarone, A. V. (2020). The changing character of carbon in fluids with pressure: organic geochemistry of Earth's upper mantle fluids. In C. E. Manning, J-F. Lin & W. L. Mao (Eds.), *Carbon in Earth's Interior* (pp. 259-269). https://doi.org/10.1002/9781119508229.ch22

Sverjensky, D. A., Harrison, B., & Azzolini, D. (2014). Water in the deep Earth: The dielectric constant and the solubilities of quartz and corundum to 60 kb and 1200 °C. *Geochimica et Cosmochimica Acta*, *129*, 125–145. https://doi.org/10.1016/j.gca.2013.12.019

Sverjensky, D. A., & Huang, F. (2015). Diamond formation due to a pH drop during fluid-rock interactions. *Nature Communications*, *6*(1), 8702. https://doi.org/10.1038/ncomms9702

Sverjensky, D. A., Stagno, V., & Huang, F. (2014). Important role for organic carbon in subduction-zone fluids in the deep carbon cycle. *Nature Geoscience*, *7*(12), 909–913. https://doi.org/10.1038/ngeo2291

Syracuse, E. M., van Keken, P. E., Abers, G. A., Suetsugu, D., Bina, C., Inoue, T., … Jellinek, M. (2010). The global range of subduction zone thermal models. *Physics of the Earth and Planetary Interiors*, *183*(1–2), 73–90. https://doi.org/10.1016/j.pepi.2010.02.004

Tatsumi, Y. (1989). Migration of fluid phases and genesis of basalt magmas in subduction zones. *Journal of Geophysical Research*, *94*(B4), 4697–4707. https://doi.org/10.1029/JB094iB04p04697

Thomassot, E., Cartigny, P., Harris, J. W., & (Fanus) Viljoen, K. S. (2007). Methane-related diamond crystallization in the Earth's mantle: Stable isotope evidences from a single diamond-bearing xenolith. *Earth and Planetary Science Letters*, *257*(3–4), 362–371. https://doi.org/10.1016/j.epsl.2007.02.020

Tingle, T. N., Roedder, E., & Green, H. W. (1992). Formation of fluid inclusions and etch tunnels in olivine at high pressure. *American Mineralogist*, *77*(3–4), 296–302.

Tiraboschi, C., Miozzi, F., & Tumiati, S. (2022). Carbon-saturated COH fluids in the upper mantle: A review of high-pressure and high-temperature ex situ experiments. *European Journal of Mineralogy* , 34(1), 59-75. https://doi.org/10.5194/ejm-34-59-2022

Tomlinson, E. L., Jones, A. P., & Harris, J. W. (2006). Co-existing fluid and silicate inclusions in mantle diamond. *Earth and Planetary Science Letters*, *250*(3–4), 581–595. https://doi.org/10.1016/j.epsl.2006.08.005

Tomlinson, E. L., & Müller, W. (2009). A snapshot of mantle metasomatism: Trace element analysis of coexisting fluid (LA-ICP-MS) and silicate (SIMS) inclusions in fibrous diamonds. *Earth and Planetary Science Letters*, *279*(3–4), 362–372. https://doi.org/10.1016/j.epsl.2009.01.010

Touret, J. L. R. (2009). Mantle to lower-crust fluid/melt transfer through granulite

metamorphism. *Russian Geology and Geophysics*, *50*(12), 1052–1062. https://doi.org/10.1016/j.rgg.2009.11.004

Touret, J. L. R., & Huizenga, J. M. (2012). Fluid-assisted granulite metamorphism: A continental journey. *Gondwana Research*, 21(1), 224-235. https://doi.org/10.1016/j.gr.2011.07.022

Trail, D., Watson, E. B., & Tailby, N. D. (2011). The oxidation state of Hadean magmas and implications for early Earth's atmosphere. *Nature*, *480*(7375), 79–82. https://doi.org/10.1038/nature10655

Trieloff, M., Kunz, J., Clague, D. A., Harrison, D., & Allègre, C. J. (2000). The nature of pristine noble gases in mantle plumes. *Science*, *288*(5468), 1036–1038. https://doi.org/10.1126/science.288.5468.1036

Trumbull, R. B., Yang, J.-S., Robinson, P. T., Di Pierro, S., Vennemann, T., & Wiedenbeck, M. (2009). The carbon isotope composition of natural SiC (moissanite) from the Earth's mantle: New discoveries from ophiolites. *Lithos*, *113*(3–4), 612–620. https://doi.org/10.1016/j.lithos.2009.06.033

Tschauner, O., Huang, S., Greenberg, E., Prakapenka, V. B., Ma, C., Rossman, G. R., … Tait, K. (2018). Ice-VII inclusions in diamonds: Evidence for aqueous fluid in Earth's deep mantle. *Science*, *359*(6380), 1136–1139. https://doi.org/10.1126/science.aao3030

Tuff, J., Wade, J., & Wood, B. J. (2013). Volcanism on Mars controlled by early oxidation of the upper mantle. *Nature*, *498*(7454), 342–345. https://doi.org/10.1038/nature12225

Uematsu, M., & Franck, E. U. (1980). Static dielectric constant of water and steam. *Journal of Physical and Chemical Reference Data*, *9*(4), 1291–1306. https://doi.org/10.1063/1.555632

Ulmer, G. C., Grandstaff, D. E., Woermann, E., Göbbels, M., Schönitz, M., & Woodland, A. B. (1998). The redox stability of moissanite (SiC) compared with metal-metal oxide buffers at 1773 K and at pressures up to 90 kbar. *Neues Jahrbuch Für Mineralogie, Abhandlungen*, *172*(2–3), 279–307. https://doi.org/10.1127/njma/172/1998/279

Vandersande, J. W., & Zoltan, L. D. (1991). High temperature electrical conductivity measurements of natural diamond and diamond films. *Surface and Coatings Technology*, *47*(1–3), 392–400. https://doi.org/10.1016/0257-8972(91)90305-G

Wagner, W., & Pruß, A. (2002). The IAPWS formulation 1995 for the thermodynamic properties of ordinary water substance for general and scientific use. *Journal of Physical and Chemical Reference Data*, *31*(2), 387–535. https://doi.org/10.1063/1.1461829

Walker, R. J. (2009). Highly siderophile elements in the Earth, Moon and Mars: Update and implications for planetary accretion and differentiation. *Chemie Der Erde*, *69*(2), 101–125. https://doi.org/10.1016/j.chemer.2008.10.001

Walther, J. V., & Orville, P. M. (1983). The extraction-quench technique for determination of the thermodynamic properties of solute complexes: application to quartz solubility in fluid mixtures. *American Mineralogist*, *68*(7–8), 731–741.

Wannamaker, P. E. (2000). Comment on "The petrologic case for a dry lower crust" by Bruce W. D. Yardley and John W. Valley. *Journal of Geophysical Research: Solid Earth*, *105*(B3), 6057–6064. https://doi.org/10.1029/1999JB900324

Weinberg, R. F., & Hasalová, P. (2015). Water-fluxed melting of the continental crust: A review, *212*, 158-188. https://doi.org/10.1016/j.lithos.2014.08.021

Weiner, R. (1960). R. Parsons: Handbook of electrochemical constants. *Zeitschrift Für Elektrochemie, Berichte Der Bunsengesellschaft Für Physikalische Chemie*, *64*(6), 872–873. https://doi.org/10.1002/BBPC.19600640623

Weingärtner, H., & Franck, E. U. (2005). Supercritical water as a solvent. *Angewandte Chemie - International Edition*, 44(18), 2672-2692. https://doi.org/10.1002/anie.200462468

Weiss, Y., & Goldstein, S. L. (2018). The involvement of diamond-forming fluids in the metasomatic 'cocktail' of kimberlite sources. *Mineralogy and Petrology*, *112*(1), 149–167. https://doi.org/10.1007/s00710-018-0613-8

Weiss, Y., Kiflawi, I., Davies, N., & Navon, O. (2014). High-density fluids and the growth of monocrystalline diamonds. *Geochimica et Cosmochimica Acta*, *141*, 145–159. https://doi.org/10.1016/j.gca.2014.05.050

Williams, H. M., Wood, B. J., Wade, J., Frost, D. J., & Tuff, J. (2012). Isotopic evidence for internal oxidation of the Earth's mantle during accretion. *Earth and Planetary Science Letters*, *321–322*, 54–63. https://doi.org/10.1016/j.epsl.2011.12.030

Wiryana, S., Slutsky, L. J., & Brown, J. M. (1998). The equation of state of water to 200 °C and 3.5 GPa: Model potentials and the experimental pressure scale. *Earth and Planetary Science Letters*, *163*(1–4), 123–130. https://doi.org/10.1016/S0012-821X(98)00180-0

Withers, A. C., Kohn, S. C., Brooker, R. A., & Wood, B. J. (2000). A new method for determining the P-V-T properties of high-density H_2O using NMR: Results at 1.4-4.0 GPa and 700-1100 °C. *Geochimica et Cosmochimica Acta*, *64*(6), 1051–1057.

https://doi.org/10.1016/S0016-7037(99)00318-X

Wohlers, A., & Manning, C. E. (2009). Solubility of corundum in aqueous KOH solutions at 700 °C and 1 GPa. *Chemical Geology*, *262*(3–4), 310–317. https://doi.org/10.1016/j.chemgeo.2009.01.025

Woodland, A. B., & Koch, M. (2003). Variation in oxygen fugacity with depth in the upper mantle beneath the Kaapvaal craton, Southern Africa. *Earth and Planetary Science Letters*, *214*(1–2), 295–310. https://doi.org/10.1016/S0012-821X(03)00379-0

Wu, S., Audétat, A., Jochum, K., Wang, H., Chen, J., Stoll, B., Zhang, C., Bao, Z., Yang, S., Li, C., Wang, X., Xu, C., Xu, L., Huang, C., Xie, L., Yang, Y., Yang, J. (in press) Characterization of Three Natural Rhyolitic to Andesitic Glasses (OJY-1, OH-1, OA-1) as Reference Materials for In-Situ Microanalysis, *Chemical Geology*

Wu, Y. C., Koch, W. F., & Pratt, K. W. (1991). Proposed new electrolytic conductivity primary standards for KCl solutions. *Journal of Research of the National Institute of Standards and Technology*, *96*(2), 191-201. https://10.6028/jres.096.008

Xu, X. Z., Yang, J.-S., Robinson, P. T., Xiong, F., Ba, D. Z., & Guo, G. L. (2015). Origin of ultrahigh pressure and highly reduced minerals in podiform chromitites and associated mantle peridotites of the Luobusa ophiolite, Tibet. *Gondwana Research*, *27*(2), 686–700. https://doi.org/10.1016/j.gr.2014.05.010

Yagi, T., & Hishinuma, T. (1995). Iron hydride formed by the reaction of iron, silicate, and water: Implications for the light element of the Earth's core. *Geophysical Research Letters*, *22*(14), 1933–1936. https://doi.org/10.1029/95GL01792

Yamaguchi, T., Fukuyama, N., Yoshida, K., & Katayama, Y. (2021). Ion solvation and water structure in an aqueous sodium chloride solution in the gigapascal pressure range. *Journal of Physical Chemistry Letters*, *12*(1), 250–256. https://doi.org/10.1021/acs.jpclett.0c03147

Yang, X., Keppler, H., & Li, Y. (2016). Molecular hydrogen in mantle minerals. *Geochemical Perspectives Letters*, *2*(2), 160–168. https://doi.org/10.7185/geochemlet.1616

Yardley, B. W. D. (2009). The role of water in the evolution of the continental crust. *Journal of the Geological Society*, *166*(4), 585–600. https://doi.org/10.1144/0016-76492008-101

Yardley, B. W. D., & Bodnar, R. J. (2014). Fluids in the continental crust. *Geochemical Perspectives*, 3, 1–125. https://doi: 10.7185/geochempersp.3.1

Yardley, B. W. D., & Valley, J. W. (1997). The petrologic case for a dry lower crust. *Journal of*

Geophysical Research B: Solid Earth, *102*(6), 12173–12185. https://doi.org/10.1029/97JB00508

Yaxley, G. M., Berry, A. J., Kamenetsky, V. S., Woodland, A. B., & Golovin, A. V. (2012). An oxygen fugacity profile through the Siberian Craton - Fe K-edge XANES determinations of $Fe^{3+}/\sum Fe$ in garnets in peridotite xenoliths from the Udachnaya East kimberlite. *Lithos*, *140–141*, 142–151. https://doi.org/10.1016/j.lithos.2012.01.016

Yoshino, T., Gruber, B., & Reinier, C. (2018). Effects of pressure and water on electrical conductivity of carbonate melt with implications for conductivity anomaly in continental mantle lithosphere. *Physics of the Earth and Planetary Interiors*, *281*, 8–16. https://doi.org/10.1016/j.pepi.2018.05.003

Yoshino, T., & Noritake, F. (2011). Unstable graphite films on grain boundaries in crustal rocks. *Earth and Planetary Science Letters*, *306*(3–4), 186–192. https://doi.org/10.1016/j.epsl.2011.04.003

Zedgenizov, D. A., Rege, S., Griffin, W. L., Kagi, H., & Shatsky, V. S. (2007). Composition of trapped fluids in cuboid fibrous diamonds from the Udachnaya kimberlite: LAM-ICPMS analysis. *Chemical Geology*, *240*(1–2), 151–162. https://doi.org/10.1016/j.chemgeo.2007.02.003

Zhang, B., & Yoshino, T. (2017). Effect of graphite on the electrical conductivity of the lithospheric mantle. *Geochemistry, Geophysics, Geosystems*, *18*(1), 23–40. https://doi.org/10.1002/2016GC006530

Zhang, C., & Duan, Z. (2009). A model for C-O-H fluid in the Earth's mantle. *Geochimica et Cosmochimica Acta*, *73*(7), 2089–2102. https://doi.org/10.1016/j.gca.2009.01.021

Zhang, R. Y., Liou, J. G., Iizuka, Y., & Yang, J.-S. (2009). First record of K-cymrite in north Qaidam UHP eclogite, Western China. *American Mineralogist*, *94*(2–3), 222–228. https://doi.org/10.2138/am.2009.2983

Zhang, R. Y., Yang, J.-S., Ernst, W. G., Jahn, B. M., Iizuka, Y., & Guo, G. L. (2016). Discovery of in situ super-reducing, ultrahigh-pressure phases in the Luobusa ophiolitic chromitites, Tibet: New insights into the deep upper mantle and mantle transition zone. *American Mineralogist*, *101*(6), 1285–1294. https://doi.org/10.2138/am-2016-5436

6. Appendices

Table A1. *KCl Aqueous Solution Conductivities (S/m) Measured in the Electrochemical Diamond Anvil Cell.*

Run name	C_{KCl}, wt%	P sensor	K_{cell}, m^{-1}
DACKCl28	6.96	+	49216
T, °C	P, MPa	ρ, g/cm³	σ, S/m
100	5	0.959	24.6
125	19	0.948	29.2
150	40	0.938	32.9
175	73	0.932	36.8
200	87	0.917	38.9
225	119	0.911	41.0
250	140	0.899	42.8
275	165	0.889	44.4
300	187	0.878	45.6
325	216	0.872	46.7
350	227	0.856	46.9
375	261	0.853	47.1
400	304	0.854	47.1
425	340	0.853	46.8
450	360	0.844	46.6
475	407	0.848	46.7
500	459	0.854	46.8
100	1	0.959	25.7
125	19	0.948	30.1
150	40	0.938	34.4
175	73	0.932	37.6
200	87	0.917	40.1
225	119	0.911	41.6
250	140	0.899	43.1
275	165	0.889	44.3
300	187	0.878	45.4
325	216	0.872	46.0
350	227	0.856	46.5
375	261	0.853	46.8
400	304	0.854	47.3
425	340	0.853	47.1
450	360	0.844	46.9
475	407	0.848	46.8

Run name	C_{KCl}, wt%	P sensor	$K_{cell,}$ m^{-1}
DACKCl2	6.96	+	126502
T, °C	P, MPa	ρ, g/cm³	σ, S/m
75	223	1.054	20.4
100	203	1.034	24.7
125	256	1.035	28.5
150	295	1.031	32.3
175	353	1.032	35.5
200	397	1.029	38.2
225	408	1.016	40.3
250	491	1.023	41.7
275	525	1.017	43.0
300	561	1.012	43.6
325	609	1.009	44.1
350	638	1.002	44.9
375	697	1.003	44.8
400	743	1.001	44.7
425	767	0.994	44.7
450	761	0.979	44.6
475	757	0.965	44.4
500	788	0.961	43.9
525	785	0.947	44.0
550	853	0.953	44.0
575	852	0.940	43.7
600	921	0.946	43.5
625	939	0.940	43.6
650	957	0.933	43.7
675	1010	0.936	43.2

Run name	C_{KCl}, wt%	P sensor	K_{cell}, m^{-1}
DACKCl3	6.96	+	129728
T, °C	P, MPa	ρ, g/cm³	σ, S/m
50	329	1.096	15.7
75	428	1.108	20.6
100	496	1.110	24.6
125	561	1.111	28.5
150	625	1.110	31.9
175	684	1.109	34.4
200	739	1.107	36.7
225	830	1.111	38.6
250	820	1.096	40.1
275	830	1.085	41.6
300	899	1.086	42.6
325	910	1.075	43.5
350	870	1.055	44.5
375	859	1.040	44.8
400	806	1.016	44.9
425	792	1.000	45.0
100	301	1.063	24.4
125	351	1.062	29.0
150	344	1.045	32.6
175	385	1.041	35.6
200	431	1.038	38.2
225	493	1.039	40.3
250	556	1.040	41.8
275	533	1.019	43.1
300	602	1.022	44.0
325	672	1.025	44.5
350	671	1.011	44.8
375	729	1.011	45.2
400	640	0.975	44.9

Run name	C_{KCl}, wt%	P sensor	K_{cell}, m^{-1}
DACKCl29	6.96	+	73506
T, °C	P, MPa	ρ, g/cm³	σ, S/m
275	39	0.800	42.1
300	49	0.775	42.5
325	124	0.814	43.0
350	117	0.779	43.3
375	162	0.789	43.6
400	213	0.802	43.9
425	253	0.805	43.6
450	218	0.758	43.3
475	299	0.791	43.1
500	313	0.780	43.0

Run name	C_{KCl}, wt%	P sensor	K_{cell}, m^{-1}
DACKCl30	6.96	+	59241
T, °C	P, MPa	ρ, g/cm³	σ, S/m
100	19	0.967	26.4
125	67	0.970	30.7
150	96	0.963	34.6
175	146	0.964	38.1
200	198	0.966	40.7
225	236	0.961	43.0
250	281	0.959	44.7
275	332	0.959	45.8
300	385	0.960	47.2
325	439	0.961	48.3
350	479	0.958	48.8
375	503	0.949	49.1
400	546	0.948	49.6
100	14	0.965	26.5
125	46	0.961	31.3
150	102	0.966	35.3
175	134	0.960	39.0
200	166	0.953	41.8
225	224	0.957	44.0
250	257	0.950	45.6
275	320	0.955	46.7
300	350	0.948	47.7
325	405	0.950	48.2
350	453	0.949	48.8
375	503	0.949	49.5

Run name	C_{KCl}, wt%	P sensor	$K_{cell,}$ m^{-1}
DACKCl31	6.96	+	72047
T, °C	P, MPa	ρ, g/cm³	σ, S/m
50	5	0.990	15.9
75	73	1.005	21.5
100	114	1.005	26.4
125	170	1.008	31.0
150	200	1.002	35.2
175	251	1.002	38.7
200	305	1.002	41.8
225	339	0.996	43.7
250	387	0.994	46.5
275	416	0.987	48.2
300	465	0.985	49.4
325	486	0.976	48.4
350	529	0.973	48.8
375	584	0.974	49.0
400	635	0.973	49.2
425	697	0.976	49.3
450	769	0.981	49.3
400	601	0.964	49.2
425	675	0.970	49.3

Run name	C_{KCl}, wt%	P sensor	$K_{cell,}$ m^{-1}
DACKCl32	6.96	+	72314
T, °C	P, MPa	ρ, g/cm³	σ, S/m
25	10	1.001	10.6
50	104	1.029	15.7
75	155	1.033	20.7
100	208	1.036	25.5
125	266	1.038	29.7
150	317	1.038	33.5
175	366	1.036	36.5
200	418	1.034	39.3
225	465	1.032	41.8
250	427	1.006	44.8
275	469	1.002	46.1

Run name	C_{KCl}, wt%	P sensor	K_{cell}, m^{-1}
DACKCl33	6.96	+	74619
T, °C	P, MPa	ρ, g/cm³	σ, S/m
25	38	1.013	10.5
50	116	1.033	15.6
75	159	1.035	20.8
100	212	1.037	25.5
125	275	1.041	29.8
150	320	1.039	33.9
175	376	1.039	37.3
200	418	1.034	40.2

Run name	C_{KCl}, wt%	P sensor	K_{cell}, m^{-1}
DACKCl4	0.74	+	126230
T, °C	P, MPa	ρ, g/cm³	σ, S/m
75	2088	1.340	1.08
100	2190	1.339	1.45
125	2277	1.336	1.78
150	2350	1.332	2.13
175	2425	1.329	2.44
200	2469	1.323	2.73
225	2257	1.294	3.21
250	1443	1.194	4.06
75	761	1.175	1.94
100	828	1.174	2.37
125	880	1.170	2.78
150	936	1.167	3.14
175	994	1.164	3.47
200	1124	1.172	3.76
225	1205	1.172	3.96

Run name	C_{KCl}, wt%	P sensor	K_{cell}, m^{-1}
DACKCl5	0.74	+	136646
T, °C	P, MPa	ρ, g/cm³	σ, S/m
25	791	1.205	1.13
50	921	1.214	1.56
75	985	1.211	2.02
100	1086	1.214	2.46
125	1122	1.207	2.86
150	1212	1.208	3.26
175	1287	1.207	3.57
200	1348	1.203	3.86
225	1429	1.203	4.16
250	1512	1.203	4.47
275	1615	1.205	4.75
300	1685	1.203	4.84
325	1809	1.208	4.81
350	1797	1.197	4.81
375	1872	1.196	5.21
400	1933	1.194	5.07
425	2098	1.204	5.19
450	1747	1.153	5.27
75	571	1.139	2.29
100	603	1.132	2.87
125	656	1.130	3.31
150	695	1.124	3.75
175	753	1.122	4.14
200	814	1.121	4.46
225	877	1.119	4.78
250	960	1.122	4.92
275	977	1.112	5.09
300	1064	1.115	5.17
325	1136	1.115	5.19
350	1210	1.116	5.35
375	1286	1.117	5.36
400	1364	1.119	5.34
425	1529	1.133	5.28

Run name	C_{KCl}, wt%	P sensor	K_{cell}, m^{-1}
DACKCl25	0.74	-	48815
T, °C	P, MPa	ρ, g/cm³	σ, S/m
200	17	0.876	5.53
225	58	0.876	5.90
250	99	0.876	6.20
275	141	0.876	6.45
300	182	0.876	6.64
325	224	0.876	6.81
350	267	0.876	6.65
375	309	0.876	6.52
400	350	0.876	6.29
425	392	0.876	6.39
450	433	0.876	6.40
475	474	0.876	6.53
500	515	0.876	6.52
200	23	0.880	5.66
225	64	0.880	6.00
250	106	0.880	6.24
275	148	0.880	6.43
300	190	0.880	6.58
325	232	0.880	6.74
350	275	0.880	6.82
400	359	0.880	6.41
450	443	0.880	6.51

Run name	C_{KCl}, wt%	P sensor	K_{cell}, m^{-1}
DACKCl26	0.74	+	54752
T, °C	P, MPa	ρ, g/cm³	σ, S/m
175	30	0.910	5.24
200	72	0.909	5.68
225	106	0.904	6.04
250	175	0.916	6.29
275	197	0.905	6.49
300	246	0.907	6.67
325	286	0.905	6.74
350	315	0.898	6.73
375	337	0.889	6.72
400	394	0.894	6.68
425	404	0.881	6.74
450	438	0.878	6.61
475	471	0.875	6.65
500	499	0.870	6.68
525	553	0.875	6.64

Run name	C_{KCl}, wt%	P sensor	K_{cell}, m^{-1}
DACKCl34	0.74	+	58603
T, °C	P, MPa	ρ, g/cm³	σ, S/m
125	24	0.951	3.99
150	78	0.955	4.73
175	134	0.960	5.38
200	193	0.964	5.84
225	226	0.957	6.11
250	252	0.949	6.39
275	299	0.948	6.61
300	324	0.939	6.66
325	352	0.931	6.72
350	390	0.928	6.78
375	431	0.925	6.65
400	474	0.924	6.71
425	479	0.910	6.66

Run name	C_{KCl}, wt%	P sensor	K_{cell}, m^{-1}
DACKCl36	0.74	+	74264
T, °C	P, MPa	ρ, g/cm³	σ, S/m
50	26	0.999	1.97
75	68	1.003	2.66
100	102	1.001	3.48
125	153	1.003	4.25
150	194	1.000	4.85
175	241	0.999	5.66
350	567	0.984	6.80
375	632	0.987	6.88
400	656	0.979	6.88
75	78	1.007	2.90
100	114	1.005	3.74
125	144	0.999	4.42
150	182	0.996	4.80
175	216	0.990	5.37
200	248	0.984	5.74
225	310	0.987	6.07
250	324	0.974	6.34
275	385	0.977	6.55
300	422	0.972	6.70
325	486	0.976	6.90
350	525	0.972	6.85
375	601	0.978	6.90

Run name	C_{KCl}, wt%	P sensor	K_{cell}, m^{-1}
DACKCl37	0.74	+	62479
T, °C	P, MPa	ρ, g/cm³	σ, S/m
25	22	1.007	1.27
50	60	1.013	1.94
75	121	1.022	2.58
100	165	1.022	3.32
125	213	1.022	3.98
150	251	1.018	4.23
175	239	0.998	4.82
200	301	1.001	5.19
225	382	1.009	5.45
250	417	1.003	5.73
275	452	0.997	5.97
300	501	0.995	6.16
325	548	0.993	6.29
350	577	0.986	6.35
375	611	0.981	6.44
400	645	0.976	6.47
425	676	0.970	6.39
450	725	0.970	6.41
150	177	0.994	4.50
175	199	0.984	4.99
200	258	0.987	5.40
225	275	0.975	5.68
250	327	0.975	5.92
275	338	0.961	6.11
300	389	0.961	6.26
325	393	0.946	6.34
350	444	0.946	6.38
375	498	0.948	6.56
400	546	0.948	6.42
425	597	0.948	6.41

Run name	C_{KCl}, wt%	P sensor	K_{cell}, m^{-1}
DACKCl18	0.74	+	41799
T, °C	P, MPa	ρ, g/cm³	σ, S/m
125	58	0.966	0.46
150	125	0.975	0.50
175	137	0.961	0.54
200	188	0.962	0.59
225	204	0.949	0.65
250	274	0.957	0.69
275	333	0.960	0.71
300	348	0.947	0.73
325	389	0.944	0.76
350	425	0.940	0.77
375	480	0.942	0.78
400	520	0.939	0.78

Run name	C_{KCl}, wt%	P sensor	K_{cell}, m^{-1}
DACKCl22	0.07	+	31507
T, °C	P, MPa	ρ, g/cm³	σ, S/m
25	5	0.999	0.14
50	35	1.003	0.20
75	104	1.016	0.28
100	145	1.016	0.35
125	185	1.013	0.39
150	222	1.009	0.46
175	266	1.007	0.51
200	313	1.005	0.56
225	351	1.000	0.58
250	384	0.993	0.58
275	419	0.987	0.58
300	488	0.992	0.62
325	523	0.986	0.65
350	573	0.985	0.70
375	618	0.983	0.69
400	668	0.982	0.75
425	623	0.956	0.75

Run name	C_{KCl}, wt%	P sensor	K_{cell}, m^{-1}
DACKCl23	0.07	+	16660
T, °C	P, MPa	ρ, g/cm³	σ, S/m
50	42	1.006	0.20
75	99	1.014	0.27
100	153	1.018	0.35
125	215	1.023	0.41
150	268	1.024	0.47
175	297	1.016	0.52
200	356	1.017	0.57
225	358	1.002	0.60
250	406	1.000	0.64
275	462	1.000	0.67
300	488	0.992	0.70
325	534	0.989	0.71
350	584	0.988	0.72
375	641	0.989	0.73

Table A2. *Measured Resistances (Ω) of Piston-cylinder Assemblies, with Correction for Lead Resistance Applied.*

	6.96 wt% KCl									
	1 GPa			2 GPa			3 GPa			
T, °C	KV8	KV11	KV12	KV14	KV15	KV16	KV17	KV18	KV29	KV63*
900	37.7	32.8	32.5	20.2	29.5	23.4		19.3	18.0	16.7
850	37.9	33.1	32.8	21.0	30.7	24.2		20.7	19.1	16.8
800	38.1	33.5	33.3	21.7	31.6	24.6		21.9	20.2	16.9
750	38.5	33.5	33.8	22.1	32.2	24.9	21.0	23.0	21.3	17.9
700	38.7	33.6	34.1	22.6	32.7	25.3	21.8	24.0	22.3	18.7
650	38.9	33.7	34.5	23.2	33.2	25.7	22.8	25.0	23.4	20.0
600	39.2	33.6	34.9	23.8	33.6	26.2	23.8	26.0	24.6	21.3
550	39.4	33.3	35.1	24.4	33.8	26.5	25.1	27.1	26.0	22.4
500	39.5	32.8	35.2	25.0	34.1	26.8	26.5	28.4	27.7	23.1
450	39.5	32.5	35.3	25.9	34.4	27.1	28.2	30.0	29.9	24.0
400	39.6	32.2	35.3	27.0	34.5	27.2	30.4	32.0	33.0	25.3
350	39.6	30.5	33.8	28.8	37.4	27.5	34.0	34.9	37.6	27.1
300	38.1	29.8	33.0	32.0	39.6	28.2	39.4	40.7	45.7	29.5
250	39.6	31.7	34.1	36.3	41.7	29.5	47.8	48.9	57.8	34.2
200	43.3	35.8	37.4	41.3	44.6	33.0	60.0	60.9	78.5	41.7
150	50.4	43.2	44.7	49.8	53.2	38.8				
100	67.7	57.8	62.1	78.5	75.3	52.7				
Lead R, (Ω)	*1.8*	*2.7*	*2.0*	*1.7*	*1.9*	*1.3*	*2.7*	*1.8*	*1.7*	*1.8*

**experiments KV60-60_2, KV62-62_2, KV63-63_2, KV65-65_2 were performed with the same assembly at 2 sequential pressures.*

	6.96 wt% KCl							
	4 GPa					5 GPa		
T, °C	KV20	KV21	KV22	KV23	KV62*	KV56	KV62_2*	KV63_2*
900	13.8	17.8	15.7		16.9	10.1	15.4	7.4
850	14.7	19.3	16.7		18.9	11.0	17.1	8.7
800	15.7	20.8	17.8		20.7	12.0	18.8	10.2
750	16.8	22.0	18.9	24.1	22.2	13.5	20.6	12.6
700	18.0	23.5	20.0	24.9	24.1	15.5	22.8	15.0
650	19.3	24.9	21.4	26.2	27.1	17.0	26.2	17.5
600	20.8	26.4	22.8	27.4	30.6	18.9	29.7	19.2
550	22.6	27.9	24.5	28.8	33.8	21.1	32.8	21.0
500	24.8	29.5	26.9	30.4	36.9	23.1	36.1	23.5
450	28.0	31.4	29.8	32.5	40.6	24.4	40.2	25.9
400	32.4	34.1	34.3	35.1	45.6	26.8	46.4	28.9
350	39.3	37.6	43.6	38.9	53.6	29.7	55.0	33.2
300	50.0	42.3	55.8	44.4	63.3	32.9	67.1	38.4
250	67.7	50.5	74.5	53.4	78.0			
200								
150								
100								
Lead R, (Ω)	*1.9*	*2.9*	*2.2*	*2*	*0.9*	*0.8*	*0.9*	*1.3*

	0.74 wt% KCl									
	1 GPa				2 GPa			3 GPa		
T, °C	KV31	KV33	KV36	KV41	KV42	KV43	KV44	KV45	KV46	KV61
900	27.1	29.3	18.4	16.8	25.1	22.2	22.9	19.4	17.3	20.8
850	27.9	28.8	19.2	17.8	26.7	23.5	24.4	20.5	18.4	22.1
800	28.1	28.6	18.6	18.1	27.4	23.9	25.3	22.0	20.0	23.1
750	28.4	27.0	18.8	18.3	27.8	24.1	26.6	24.1	22.7	24.0
700	28.3	26.5	18.7	18.4	29.2	26.5	28.2	27.9	26.1	25.0
650	28.2	26.0	18.2	18.5	32.1	29.2	32.3	30.7	30.5	26.3
600	28.6	25.6	18.0	18.8	34.4	32.4	37.1	35.7	34.8	28.5
550	29.2	25.4	17.9	19.1	36.8	35.8	41.7	41.3	41.5	31.8
500	30.2	25.4	18.3	19.5	40.9	37.2	44.3	46.1	48.7	35.3
450	31.6	25.8	18.7	20.0	44.8	40.3	48.2	52.2	55.5	39.4
400	34.1	26.9	19.8	20.7	50.3	44.1	50.2	57.6	63.0	45.3
350	37.8	29.3	21.4	22.3	54.2	46.9	56.0	64.4	70.5	54.3
300	42.7	33.2	24.4	26.6	59.0	51.0	61.6	72.5	80.5	67.2
250	50.5	38.9	28.5	31.5	66.3	57.4	72.3	86.9	94.7	88.5
200	59.6	47.0	33.6	37.3	80.0	69.1	86.7	111	119	126
150	71.9	63.9	45.4	47.5	103.9	85.7	109.8			
100	105.5	115.1	77.2	76.1	145.9	115.0	164.7			
Lead R, (Ω)	*1.8*	*2.5*	*1.8*	*1.4*	*2.1*	*1.6*	*2*	*1*	*1.4*	*1.2*

	0.74 wt% KCl						0.075 wt% KCl				
	4 GPa			5 GPa			1 GPa	2 GPa	3 GPa	4 GPa	5 GPa
T, °C	KV47	KV60	KV65*	KV58	KV60_2	KV65_2*	KV49	KV51	KV53	KV55	KV59
900	14.2	28.8	22.7	23.2	24.6	21.6	44.4	28.9	20.2	17.1	14.7
850	14.8	31.1	23.7	26.9	26.3	23.0	45.7	30.7	22.1	19.1	17.0
800	15.4	33.0	25.4	30.9	27.8	25.1	49.1	32.7	23.8	21.0	22.0
750	16.1	34.3	27.2	35.2	29.4	27.1	53.2	34.6	25.7	23.4	26.2
700	17.2	36.2	30.2	41.0	31.7	28.9	57.7	37.6	30.3	26.0	30.1
650	19.3	39.6	33.0	47.2	36.6	31.8	62.6	42.0	35.4	30.3	33.8
600	22.4	44.5	37.1	55.4	40.1	35.3	67.8	50.1	41.9	33.2	38.2
550	24.5	47.5	40.6	65.1	43.2	38.5	75.5	60.3	48.1	37.9	42.7
500	26.8	50.3	44.0	76.6	46.7	41.6	83.2	72.9	55.5	42.5	46.6
450	29.6	53.1	47.6	87.9	51.4	44.8	89.7	85.7	62.0	46.4	51.1
400	32.5	56.8	51.0	97.2	58.2	49.0	99.2	95.9	70.4	50.7	56.6
350	36.2	63.3	57.0	110.5	68.7	54.5	114	106	78.7	56.7	63.2
300	41.1	72.2	63.3	131.1	81.8	65.3	126	118	89.2	65.0	73.0
250	47.8	84.3	85.9				141	137	109	77.3	
200							170	168	141		
150							213	221			
100							308	333			
Lead R, (Ω)	*0.8*	*1.1*	*1.2*	*0.9*	*1.1*	*1.2*	*1.8*	*1.7*	*1.3*	*0.8*	*0.7*

Table A3. *Conductivity (S/m) Measurements of KCl Solutions Carried Out in Piston-cylinder Assembly.*

	6.96 wt% KCl									
	1 GPa			2 GPa			3 GPa			
T, °C	KV8	KV11	KV12	KV14	KV15	KV16	KV17	KV18	KV29	KV63*
900	44.5	41.6	46.0	51.6	45.1	44.9		56.3	62.3	51.5
850	44.6	41.5	45.9	49.9	43.6	43.6		52.7	58.9	51.4
800	44.7	41.3	45.6	48.5	42.5	43.1		50.0	55.9	51.3
750	44.6	41.7	45.3	47.8	41.9	42.8	49.75	47.8	53.2	48.6
700	44.7	41.9	45.2	47.0	41.5	42.3	48.12	46.0	51.1	46.7
650	44.8	42.0	45.0	46.0	41.1	41.8	46.19	44.3	48.9	43.8
600	44.8	42.5	44.8	45.1	40.8	41.2	44.42	42.8	46.7	41.3
550	44.9	43.2	44.9	44.2	40.8	41.0	42.29	41.2	44.3	39.4
500	45.1	44.2	45.1	43.3	40.6	40.7	40.23	39.5	41.8	38.4
450	45.5	44.9	45.3	42.1	40.5	40.5	37.96	37.6	38.9	37.1
400	45.7	45.7	45.7	40.6	40.6	40.6	35.37	35.4	35.4	35.4
350	46.0	48.6	48.1	38.2	37.6	40.3	31.77	32.6	31.2	33.2
300	48.2	50.1	49.6	34.6	35.7	39.5	27.54	28.1	25.8	30.6
250	46.8	47.5	48.4	30.7	34.1	38.0	22.81	23.5	20.5	26.5
200	43.1	42.4	44.5	27.1	32.1	34.2	18.25	18.9	15.1	21.9
150	37.3	35.4	37.5	22.6	27.0	29.2				
100	27.8	26.5	27.0	14.3	19.1	21.5				
$K_{cell,}$ m^{-1}	*1809*	*1471*	*1612*	*1095*	*1399*	*1103*	*1075*	*1132*	*1167*	*895*

**experiments KV60-60_2, KV62-62_2, KV63-63_2, KV65-65_2 were performed with the same assembly at 2 sequential pressures.*

	6.96 wt% KCl							
	4 GPa					5 GPa		
T, °C	KV20	KV21	KV22	KV23	KV62*	KV56	KV62_2*	KV63_2*
900	68.6	56.0	63.8		78.8	64.8	73.6	95.4
850	64.6	51.8	60.2		70.7	59.7	66.5	81.4
800	60.7	48.2	56.7		64.8	54.9	60.6	69.6
750	56.9	45.7	53.5	43.0	60.6	48.9	55.5	56.5
700	53.3	43.0	50.8	41.7	56.0	42.7	50.3	47.6
650	49.9	40.7	47.6	39.8	50.0	39.1	43.9	40.9
600	46.4	38.5	44.8	38.2	44.4	35.3	38.9	37.4
550	42.9	36.6	41.9	36.5	40.4	31.7	35.3	34.3
500	39.2	34.7	38.3	34.7	37.1	29.0	32.2	30.8
450	34.9	32.7	34.7	32.5	33.8	27.6	29.0	28.0
400	30.3	30.3	30.3	30.3	30.3	25.2	25.2	25.2
350	25.0	27.5	23.9	27.4	25.8	22.8	21.3	22.0
300	19.8	24.6	18.7	24.1	22.0	20.7	17.6	19.1
250	14.7	20.7	14.1	20.1	17.9			
200								
150								
100								
$K_{cell,}$ m^{-1}	*980*	*1032*	*1038*	*1062*	*1380*	*676*	*1170*	*728*

	0.74 wt% KCl									
	1 GPa				2 GPa			3 GPa		
T, °C	KV31	KV33	KV36	KV41	KV42	KV43	KV44	KV45	KV46	KV61
900	6.75	4.93	5.78	6.61	9.80	9.71	10.72	12.78	15.68	9.36
850	6.61	5.05	5.58	6.29	9.26	9.22	10.11	12.14	14.80	8.84
800	6.62	5.13	5.80	6.23	9.06	9.11	9.80	11.36	13.67	8.49
750	6.60	5.47	5.79	6.21	8.98	9.08	9.36	10.41	12.09	8.20
700	6.67	5.62	5.86	6.23	8.59	8.30	8.88	9.03	10.55	7.91
650	6.74	5.77	6.07	6.24	7.85	7.57	7.79	8.24	9.07	7.54
600	6.70	5.90	6.18	6.19	7.36	6.85	6.81	7.11	7.98	6.99
550	6.61	5.99	6.26	6.13	6.92	6.23	6.09	6.17	6.72	6.29
500	6.44	6.04	6.17	6.05	6.25	6.03	5.76	5.55	5.75	5.69
450	6.20	5.99	6.08	5.95	5.74	5.59	5.32	4.92	5.07	5.12
400	5.79	5.79	5.79	5.79	5.14	5.14	5.14	4.48	4.48	4.48
350	5.26	5.36	5.40	5.41	4.80	4.86	4.63	4.03	4.02	3.75
300	4.69	4.76	4.77	4.57	4.43	4.49	4.23	3.59	3.54	3.04
250	4.00	4.10	4.12	3.89	3.96	4.01	3.63	3.01	3.02	2.32
200	3.42	3.42	3.52	3.31	3.30	3.35	3.04	2.37	2.42	1.64
150	2.85	2.53	2.62	2.62	2.55	2.72	2.41			
100	1.94	1.41	1.55	1.64	1.82	2.03	1.61			
$K_{cell,}$ m^{-1}	*197*	*156*	*115*	*120*	*258*	*227*	*258*	*258*	*282*	*203*

	0.74 wt% KCl						0.075 wt% KCl				
	4 GPa			5 GPa			1 GPa	2 GPa	3 GPa	4 GPa	5 GPa
T, °C	KV47	KV60	KV65*	KV58	KV60_2	KV65_2*	KV49	KV51	KV53	KV55	KV59
900	8.47	7.30	8.32	12.97	7.32	7.02	1.44	1.95	1.80	1.32	1.43
850	8.16	6.78	7.99	11.22	6.87	6.61	1.41	1.84	1.65	1.18	1.24
800	7.87	6.41	7.48	9.79	6.52	6.08	1.32	1.74	1.54	1.08	0.96
750	7.55	6.19	7.01	8.62	6.18	5.65	1.23	1.65	1.43	0.97	0.81
700	7.09	5.89	6.34	7.43	5.75	5.31	1.14	1.53	1.22	0.88	0.71
650	6.34	5.40	5.82	6.47	5.00	4.84	1.06	1.37	1.05	0.76	0.63
600	5.48	4.82	5.19	5.53	4.57	4.38	0.99	1.16	0.89	0.69	0.56
550	5.03	4.53	4.76	4.72	4.26	4.02	0.89	0.97	0.78	0.61	0.50
500	4.61	4.30	4.41	4.03	3.95	3.74	0.82	0.80	0.68	0.55	0.46
450	4.19	4.09	4.09	3.52	3.60	3.48	0.76	0.69	0.61	0.50	0.42
400	3.83	3.83	3.83	3.19	3.19	3.19	0.70	0.62	0.54	0.46	0.38
350	3.46	3.45	3.44	2.82	2.72	2.88	0.61	0.56	0.48	0.41	0.34
300	3.06	3.04	3.11	2.39	2.29	2.41	0.56	0.51	0.43	0.36	0.30
250	2.64	2.61	2.30				0.50	0.44	0.35	0.31	
200							0.42	0.36	0.27		
150							0.34	0.28			
100							0.23	0.18			
$K_{cell,}$ m^{-1}	*125*	*218*	*196*	*310*	*186*	*157*	*69.0*	*59.2*	*37.9*	*23.4*	*21.7*

Table A4. *Model Parameters Used for Fluid Fraction Calculations (Figures 2.10, 2.11).*

Figure 2.10					
Depth, km	T, °C	Fluid	σ_{mantle}, S/m	Ø, vol%	Locality
75	622	Hydrous carbonatite	0.025	0.28	Slave
75	622	Hydrous carbonatite	0.2	2.26	Slave
100	750	Hydrous carbonatite	0.03	0.22	Slave
100	750	Hydrous carbonatite	0.1	0.65	Slave
150	983	Hydrous carbonatite	0.02	0.07	Slave
150	983	Hydrous carbonatite	0.1	0.33	Slave
75	622	5 wt% NaCl	0.025	0.05	Slave
75	622	5 wt% NaCl	0.2	0.39	Slave
100	750	5 wt% NaCl	0.03	0.04	Slave
100	750	5 wt% NaCl	0.1	0.12	Slave
150	983	5 wt% NaCl	0.02	0.01	Slave
150	983	5 wt% NaCl	0.1	0.07	Slave
75	622	10 wt% NaCl	0.025	0.03	Slave
75	622	10 wt% NaCl	0.2	0.22	Slave
100	750	10 wt% NaCl	0.03	0.02	Slave
100	750	10 wt% NaCl	0.1	0.07	Slave
150	983	10 wt% NaCl	0.02	0.01	Slave
150	983	10 wt% NaCl	0.1	0.04	Slave
75	622	5 wt% KCl	0.025	0.10	Slave
75	622	5 wt% KCl	0.2	0.82	Slave
100	750	5 wt% KCl	0.03	0.13	Slave
100	750	5 wt% KCl	0.1	0.39	Slave
150	983	5 wt% KCl	0.02	0.08	Slave
150	983	5 wt% KCl	0.1	0.41	Slave
75	622	10 wt% KCl	0.025	0.06	Slave
75	622	10 wt% KCl	0.2	0.45	Slave
100	750	10 wt% KCl	0.03	0.07	Slave
100	750	10 wt% KCl	0.1	0.21	Slave
150	983	10 wt% KCl	0.02	0.04	Slave
150	983	10 wt% KCl	0.1	0.22	Slave
110	938	Hydrous carbonatite	0.1	0.26	Rehoboth
110	938	Hydrous carbonatite	0.2	0.52	Rehoboth
60	615	5 wt% NaCl	0.1	0.24	Rehoboth
60	615	5 wt% NaCl	1	2.40	Rehoboth
110	938	5 wt% NaCl	0.1	0.10	Rehoboth
110	938	5 wt% NaCl	0.2	0.21	Rehoboth
60	615	10 wt% NaCl	0.1	0.13	Rehoboth
60	615	10 wt% NaCl	1	1.34	Rehoboth
110	938	10 wt% NaCl	0.1	0.06	Rehoboth
110	938	10 wt% NaCl	0.2	0.12	Rehoboth
60	615	5 wt% KCl	0.1	0.41	Rehoboth
60	615	5 wt% KCl	1	4.03	Rehoboth

Depth, km	T, °C	Fluid	σ_{mantle}, S/m	Ø, vol%	Locality
110	938	5 wt% KCl	0.1	0.37	Rehoboth
110	938	5 wt% KCl	0.2	0.73	Rehoboth
60	615	10 wt% KCl	0.1	0.22	Rehoboth
60	615	10 wt% KCl	1	2.22	Rehoboth
110	938	10 wt% KCl	0.1	0.20	Rehoboth
110	938	10 wt% KCl	0.2	0.40	Rehoboth

Figure 2.11					
Depth, km	T, °C	Fluid	σ_{mantle}, S/m	Ø, vol%	Locality
105	736	Hydrous carbonatite	0.025	0.19	Dharwar (cold)
125	837	Hydrous carbonatite	0.2	1.06	Dharwar (cold)
145	930	Hydrous carbonatite	0.025	0.10	Dharwar (cold)
105	736	5 wt% NaCl	0.025	0.03	Dharwar (cold)
125	837	5 wt% NaCl	0.2	0.19	Dharwar (cold)
145	930	5 wt% NaCl	0.025	0.02	Dharwar (cold)
105	736	10 wt% NaCl	0.025	0.02	Dharwar (cold)
125	837	10 wt% NaCl	0.2	0.10	Dharwar (cold)
145	930	10 wt% NaCl	0.025	0.01	Dharwar (cold)
105	736	5 wt% KCl	0.025	0.10	Dharwar (cold)
125	837	5 wt% KCl	0.2	0.79	Dharwar (cold)
145	930	5 wt% KCl	0.025	0.10	Dharwar (cold)
105	736	10 wt% KCl	0.025	0.05	Dharwar (cold)
125	837	10 wt% KCl	0.2	0.44	Dharwar (cold)
145	930	10 wt% KCl	0.025	0.06	Dharwar (cold)
105	907	Hydrous carbonatite	0.025	0.07	Dharwar (hot)
125	1029	Hydrous carbonatite	0.2	0.41	Dharwar (hot)
105	907	5 wt% NaCl	0.025	0.03	Dharwar (hot)
125	1029	5 wt% NaCl	0.2	0.18	Dharwar (hot)
105	907	10 wt% NaCl	0.025	0.02	Dharwar (hot)
125	1029	10 wt% NaCl	0.2	0.10	Dharwar (hot)
105	907	5 wt% KCl	0.025	0.09	Dharwar (hot)
125	1029	5 wt% KCl	0.2	0.74	Dharwar (hot)
105	907	10 wt% KCl	0.025	0.05	Dharwar (hot)
125	1029	10 wt% KCl	0.2	0.40	Dharwar (hot)

Table A5. *Fitting Parameters for Figures A1-A7.*

Experiment	Element	Value	Error	Error, %
DACKCl_28, 300 °C, 6.96 wt% KCl (Figure A1)	R_1 (solution resistance), Ω	1091	1.7	0.16
	R_2, Ω	6203	1053	16.97
	CPE_1-T, F	3.98E-06	3.47E-07	8.71
	CPE_1-P	0.66	0.01	1,3
DACKCl_5, 100 °C, 0.74 wt% KCl (Figure A2)	R_1 (solution resistance), Ω	55440	420.89	0.76
	CPE_1-T, F	7.22E-12	1.73E-12	23.95
	CPE_1-P	0.92	0.02	1.69
	R_2, Ω	1.00E+20	1.00E+20	100
	CPE_2-T, F	6.38E-08	9.62E-09	15.08
	CPE_2-P	0.69	0.02	2.4
DACKCl_5, 450 °C, 0.74 wt% KCl (Figure A3)	R_1 (solution resistance), Ω	24737	215.48	0.87
	CPE_1-T, F	9.36E-12	3.83E-12	40.88
	CPE_1-P	0.95	0.03	2.8
DACKCl_22, 100 °C, 0.075 wt% KCl (Figure A4)	R_1 (solution resistance), Ω	80831	679.87	0.84
	CPE_1-T, F	2.42E-11	3.03E-12	12.54
	CPE_1-P	0.817	0.01	1.01
	R_2, Ω	1.00E+20	1.00E+20	100
	CPE_2-T, F	1.81E-06	2.35E-07	18
	CPE_2-P	0.386	0.02	5.9
KV_12 (PC), 400 °C, 6.96 wt% KCl (Figure A5)	R_1 (solution resistance), Ω	37.33	0.05	0.14
	R_2, Ohm	1.7	0.1	4.4
	CPE_1-T, F	6.10E-05	1.70E-05	26.8
	CPE_1-P	0.77	0.03	3.58
KV_61 (PC), 400 °C, 0.74 wt% KCl (Figure A6)	R_1 (solution resistance), Ω	46.45	0.06	0.13
	R_2, Ω	1.24	0.09	7.29
	CPE1-T, F	3.58E-05	1.90E-05	53.2
	CPE_1-P	0.85	0.05	6.1
KV_59(PC), 400 °C, 0.075 wt% KCl (Figure A7)	L_1, H	7.73E-07	7.60E-09	0.98
	R_1 (solution resistance), Ω	57.29	0.04	0.07
	CPE_1-T, F	3.87E-05	1.51E-06	3.9
	CPE_1-P	0.298	0.002	0.84
	R_2, Ω	1.00E+20	1.00E+20	100
	CPE_2-T, F	0.032	0.006	17.8
	CPE_2-P	0.77	0.04	4.81

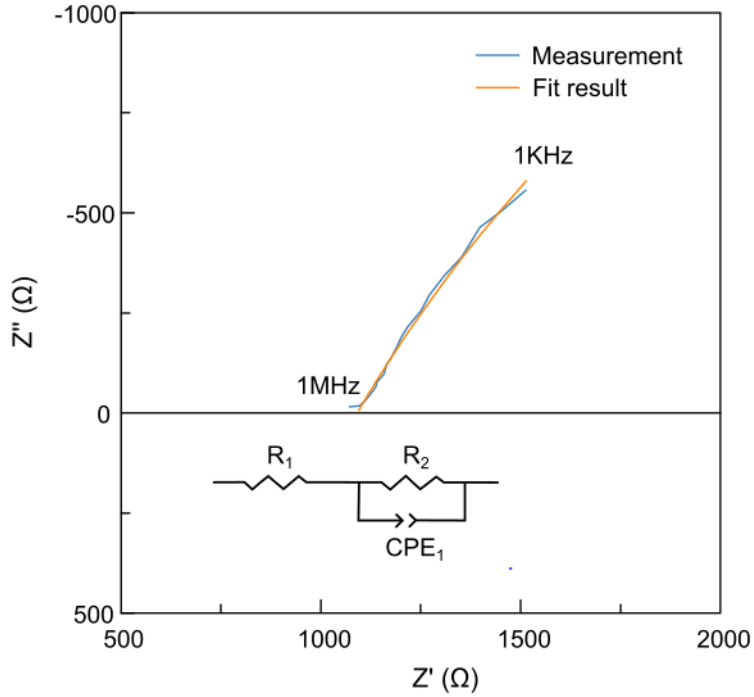

Figure A1. *Impedance graph from experiment DACKCl_28, 300 °C, 6.96 wt% KCl.*

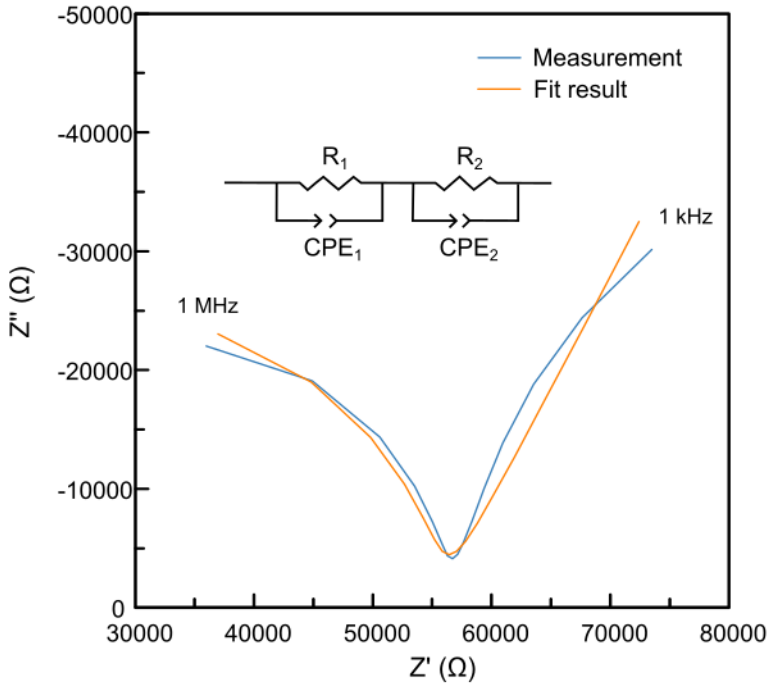

Figure A2. *Impedance graph from experiment DACKCl_5, 100 °C, 0.74 wt% KCl.*

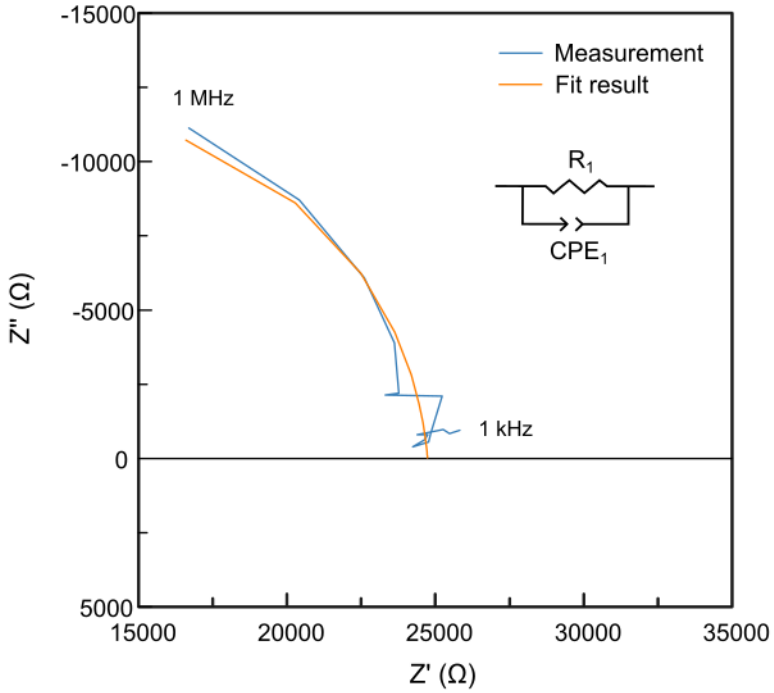

Figure A3. *Impedance graph from experiment DACKCl_5, 450 °C, 0.74 wt% KCl.*

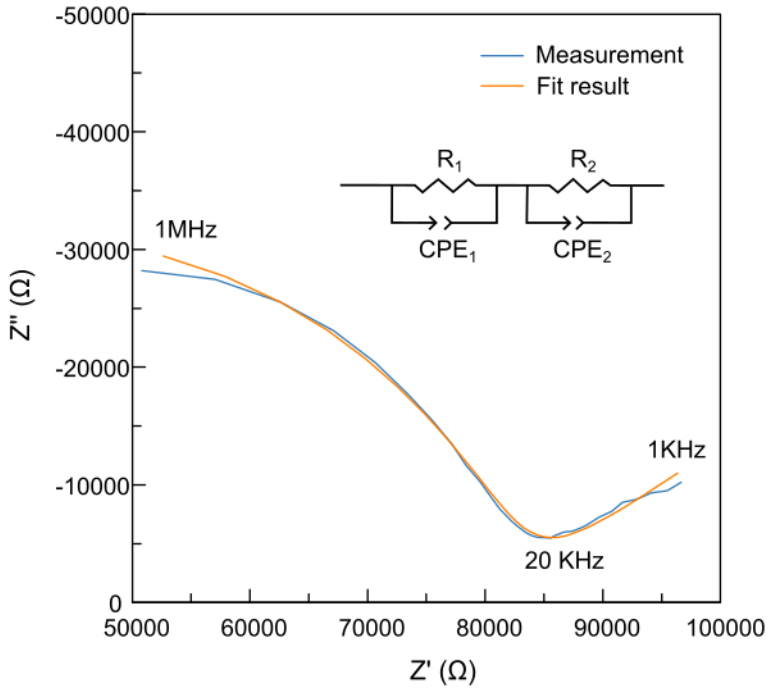

Figure A4. *Impedance graph from experiment DACKCl_22, 100 °C, 0.075 wt% KCl.*

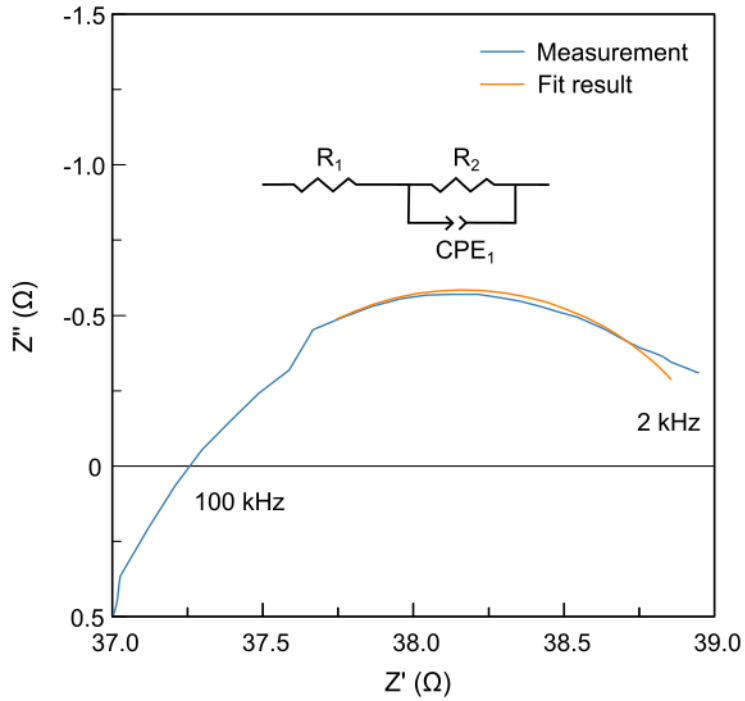

Figure A5. *Impedance graph from experiment KV_12(PC), 400 °C, 6.96 wt% KCl.*

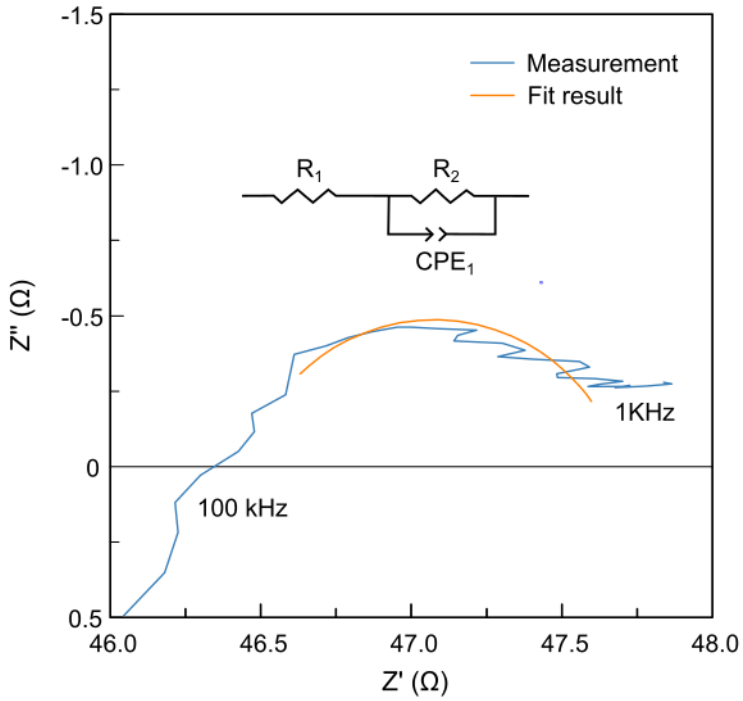

Figure A6. *Impedance graph from experiment KV_61(PC), 400 °C, 0.74 wt% KCl.*

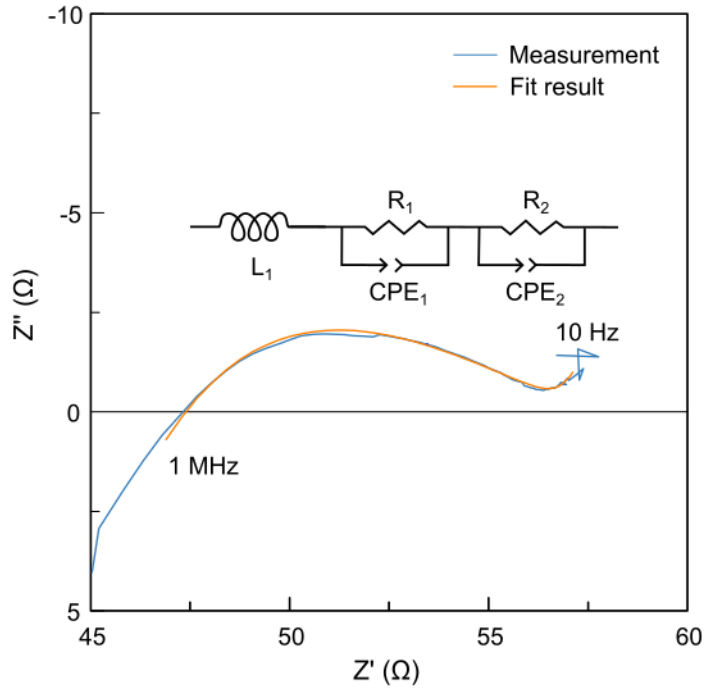

Figure A7. *Impedance graph from experiment KV_59(PC), 400 °C, 0.075 wt% KCl.*

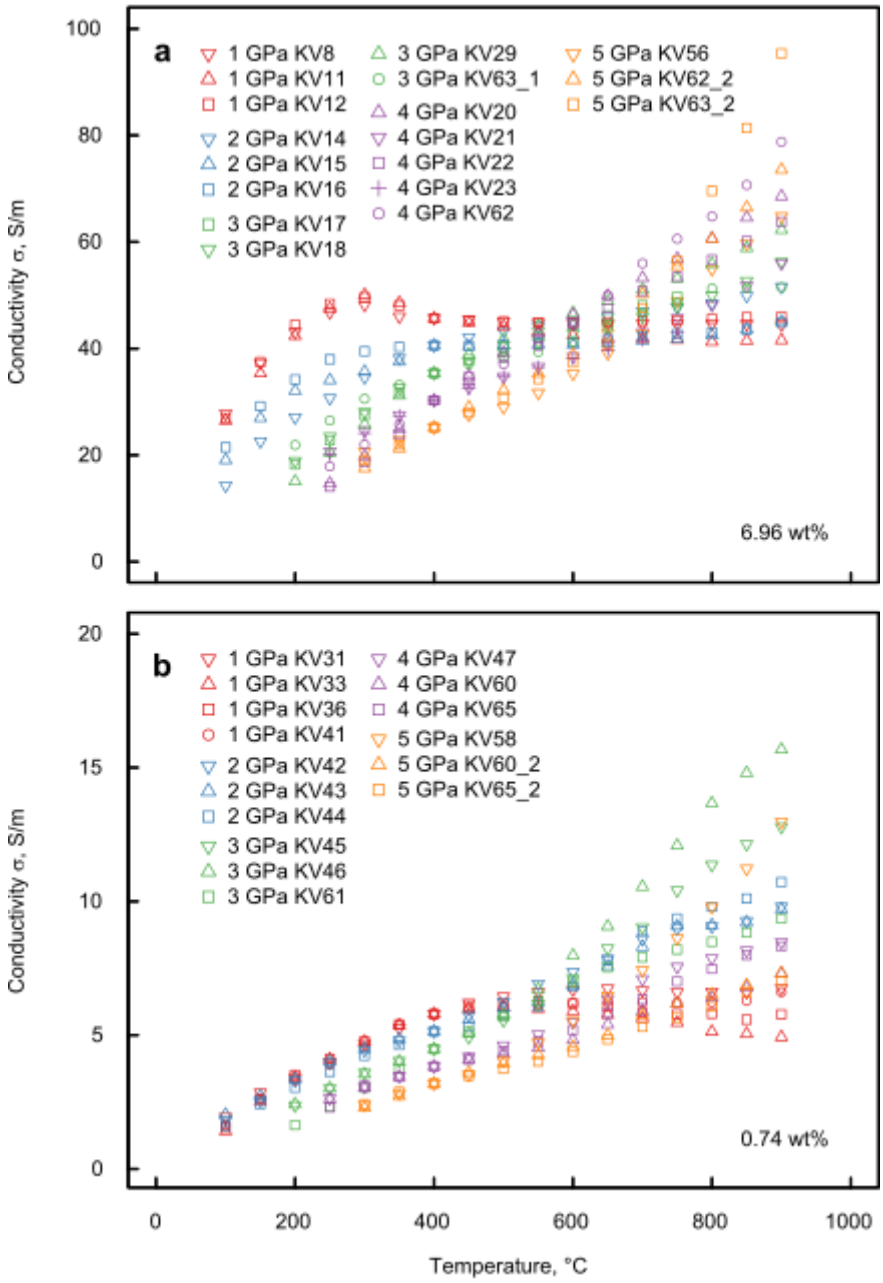

Figure A8. *Conductivity values from multiple piston-cylinder electrochemical experiments for a) 6.96 and b) 0.74 wt% KCl solutions*

Acknowledgments

I would like to thank Hans Keppler for his supervision, patience and mentorship. He came up with the ideas of the three research projects for this thesis, aided in designing the experiments, corrected all of the presented text and figures and wrote the part on acetate stability in subduction fluids. Andreas Audétat performed the LA ICP-MS analyses, aided with LA ICP-MS data processing and supplied the solid diamond discs for gasket indentation, for what I am very grateful. Help from Victoria Szlachta who performed piston-cylinder experiments investigating acetate stability and assisted with the DAC experiments of the same study is greatly appreciated. She and Hans Keppler produced the graphic materials for the part of text reporting those results as well. I would like to thank Haihao Guo for his explanations of the methodology of piston-cylinder electrochemical measurements. Discussions with Catherine McCammon, Gerd Steinle-Neumann, and Greta Rustioni were extremely helpful and allowed to significantly improve experimental procedures and data processing. Sven Linhardt and Thomas Meier provided me with valuable consultations on various electrical issues. Consultations from Leonid Dubrovinskiy on the DAC technique and general pieces of advice were a valuable contribution to this thesis, for what I am grateful.

Support from Heinz Fischer, Stefan Übelhack, Alexander Rother, Raphael Njul and Dorothea Wiesner who manufactured assembly parts and prepared the samples for all of our projects was critical and no work could have been done without it. Ulrike Trenz's help with materials supply and chemicals management was important and I would like to thank her for that. Special thanks are due to Tetsuo Irifune who kindly supplied the platelets of nanocrystalline diamond via the Joint Usage/Research Center PRIUS at Ehime University. I would also like to thank Detlef Krauße for his assistance with SEM-EDS analyses and Saiana Khandarkhaeva for her assistance with FIB. Advice and support in the matters of bureaucracy from Anna Dinius, Petra Buchert and Janina Potzel were of much help and deserve full acknowledgement. Last minute aid with machine time from Lianjie Man and Pedro Antonio Valdivia Munoz allowed to complete the experimental and analytical procedures on time. Mentorship from Jonathan Dolinschi on various manufacturing techniques is appreciated as well.

I would also like to thank my parents Ekaterina Vlasova and Alexey Vlasov, as well as my girlfriend Ekaterina Ivanova for their love and support through all those years.

(Eidesstattliche) Versicherungen und Erklärungen

(§ 9 Satz 2 Nr. 3 PromO BayNAT)

Hiermit versichere ich eidesstattlich, dass ich die Arbeit selbstständig verfasst und keine anderen als die von mir angegebenen Quellen und Hilfsmittel benutzt habe (vgl. Art. 64 Abs. 1 Satz 6 BayHSchG).

(§ 9 Satz 2 Nr. 3 PromO BayNAT)

Hiermit erkläre ich, dass ich die Dissertation nicht bereits zur Erlangung eines akademischen Grades eingereicht habe und dass ich nicht bereits diese oder eine gleichartige Doktorprüfung endgültig nicht bestanden habe.

(§ 9 Satz 2 Nr. 4 PromO BayNAT)

Hiermit erkläre ich, dass ich Hilfe von gewerblichen Promotionsberatern bzw. -vermittlern oder ähnlichen Dienstleistern weder bisher in Anspruch genommen habe noch künftig in Anspruch nehmen werde.

(§ 9 Satz 2 Nr. 7 PromO BayNAT)

Hiermit erkläre ich mein Einverständnis, dass die elektronische Fassung meiner Dissertation unter Wahrung meiner Urheberrechte und des Datenschutzes einer gesonderten Überprüfung unterzogen werden kann.

(§ 9 Satz 2 Nr. 8 PromO BayNAT)

Hiermit erkläre ich mein Einverständnis, dass bei Verdacht wissenschaftlichen Fehlverhaltens Ermittlungen durch universitätsinterne Organe der wissenschaftlichen Selbstkontrolle stattfinden können.

…….
Ort, Datum, Unterschrift